Indirect estimation of mean vorticity from polarized emission of nanoparticles in turbulent duct flows

Kishan Ramesh Kumar

Delft University of Technology

This dissertation is submitted for the degree of
MSc, Mechanical Engineering

Delft University of Technology October 2019

Indirect estimation of mean vorticity from polarized emission of nanoparticles in turbulent duct flows

by

Kishan Ramesh Kumar

to obtain the degree of Master of Science
at the Delft University of Technology,
to be defended on Thursday, October 31, 2019 at 15:00 hours
P&E number: 2996

Student number:	4737202	
Project duration:	Dec 23, 2019 – Oct 31, 2019	
Thesis committee:	Prof. dr. ir. C. Poelma,	TU Delft, supervisor and chair
	Dr. ir. M. J. Tummers	TU Delft, committee member
	Dr. R. Delfos	TU Delft, committee member
	Dr. G. A. Bohlin	TU Delft, committee member

TU Delft

ETH zürich

I would like to dedicate this thesis to my loving parents, my brother, my sister-in-law and pray for the recovery of the Amazon forest …

Declaration

I hereby declare that except where specific reference is made to the work of others, the contents of this dissertation are original and have not been submitted in whole or in part for consideration for any other degree or qualification in this, or any other university. This dissertation is my own work and contains nothing which is the outcome of work done in collaboration with others, except as specified in the text and acknowledgements.

Kishan Ramesh Kumar
October 2019

Preface

This thesis attempts to develop a new novel measurement technique from ground zero. The physics behind the technique, the approach which needs to be undertaken to show the proof of concept and the necessary experimental equipment to be used is unfamiliar. Due to the lack of previous literature to support this approach, intensive preliminary studies have to be conducted. Overall, it attempts to answer at least a few of the questions which will set the necessary ground rules for further development of this technique.

In brief, consider phosphorescent nanoparticles as tracers in a turbulent flow which are sensitive to polarized excitation. When they are excited, the emitted light would retain some of its polarization. The rate of rotation of the particles change which alters the emission polarization. By measuring the change in polarization of the nanoparticles, vorticity was estimated in the fluid medium. The objective of this thesis was to conceptualize the possibility of this technique by conducting steady-state measurements rather than focusing on the accuracy of estimated vorticity.

Readers who are particularly interested in understanding the physics behind the technique are directed to section 3.5. Those who are interested in the mathematics involved behind this technique, are directed to section 3.3. Necessary preliminary studies conducted to support the hypothesis and use it in actual results are presented in chapter 5. This approach involves several assumptions and a dedicated procedure was developed to conduct the experiments. They are listed in subsection 3.5.5 and Appendix B respectively. Based on the two approaches undertaken to interpret this technique as illustrated in Figure 1.1, the results are presented to the reader in chapter 6. In each chapter, the possible sources of error and scope for improvements are hinted which might be relevant for future researchers.

Acknowledgements

I would like to acknowledge Prof. Roesgen for giving me this opportunity to work at the Institute of Fluid Dynamics (IFD) at ETH, Zurich. His vision to embark upon the novel and diverse experiments with an open mind has motivated me continuously. I would also thank Prof. dr. ir. C. Poelma, Chair of Multi-phase systems from TU Delft for being an external supervisor. I thank him sincerely for all his help in writing report and helping me with presentation. I would like thank TU Delft for the JvE grant for funding me throughout this thesis. I would also like to thank my other committee members in the defense, Dr.ir. M.J. Tummers, Dr. R. Delfos and Dr. G.A. Bohlin.

I would like to thank the graduate student Markus Schmidt who was my weekly supervisor in this project. His way of writing python scripts, research approach and writing reports have helped me to become a better researcher in the long run. He also helped me a lot in aligning the experimental setup and all the administrative paperwork to accept me as an exchange student.

I would like to thank all my family members my mom, dad, brother, sister-in-law without their sacrifices I would not have completed this master. I would like to thank all my cousins Varsh, Keer, Shravs, Pavan, and Lakshmi for their joyful conversations. I would like to thank my grandparents and my aunts and uncles for siding by me throughout this journey.

I would like to thank Jennifer who helped me around the lab and for brainstorming sessions regarding the scope of the experiments. I would like to thank Sthavishtha, Prajish and Shruti from ETH who constantly supported me during the project. I would like to thank Udhav, Anand, Arjun, Kalpit, Maneesh, Karthick, Kunal, Shriram, Shravan, Samuel, Amogh, Jim, Cipher, Biswa, Nidarshan who supported me continuously. I would like to thank Akhilesh, Badri, Anoosh, Arvind, Arya, Varun, Anurag, Sushant, Sharab and Vetri for making this as fun-filled masters.

Abstract

Optical measurement techniques are widely used in fluid mechanics to measure quantities like velocity, vorticity, and temperature. They are usually non-intrusive visualization techniques that provide a major advantage by not influencing the flow properties. Most of the developed measurement techniques estimate vorticity by computing the gradients of the measured velocity fields.

In this project, the idea is to directly measure the mean vorticity using polarized emission of nanoparticles. The nanoparticles are excited using vertically and horizontally polarized laser. Accordingly, the emission from these nanoparticles is separated into vertical and horizontal polarized emissions respectively. Depending on the percentage of fluorophores in the nanoparticles whose absorption dipole moment is parallel to the excitation electric vector of the laser, the polarized emission is varied. The nanoparticles in the quiescent fluid state have a characteristic polarization (or anisotropy) depending on the chemical composition of the nanoparticle. However, in turbulent flows, depolarization of the particles can occur because of the rotation of the nanoparticles due to vorticity. Based on this idea, the vorticity can be estimated by quantifying the depolarization in turbulent flows. To verify the above phenomena experimentally, steady-state polarization measurements were conducted.

A cost-effective experimental setup was built specifically to measure depolarization from these nanoparticles. Important preliminary tests like lifetime measurements, spectroscopic studies, and photo-bleaching experiments were conducted. Based on these results, hybrid europium based chelated spherical particles were chosen. To further understand the properties of these particles in a quiescent flow, a consolidated set of anisotropy measurements were conducted to study their oxygen sensitivity in the surrounding medium, viscosity dependence and the effect of its concentration in the fluids. Analytical correlations which was developed in-house to translate the depolarization of the nanoparticles to vorticity was used in this thesis. Flow in a square duct was studied to estimate the vorticity along the edges and further compare it with the DNS data.

Two additional non-dimensional numbers ND1 and ND2 were introduced to interpret the underlying physics behind the problem. The variation of synthetic signals was studied for different Re, fundamental anisotropy r_0 and the non-dimensional number ND2. These synthetic signals showed a drop in anisotropy near the edges of the square duct that has occurred probably due to vorticity. Emission polarized intensity signals and the anisotropy contours for Re = 0 and Re = 4434 were analyzed. Due to the measurement error, the contours were column averaged and respectively compared their variation along the width of the square duct. A drop in anisotropy was observed for Re = 4434. Using the ratio of emission intensities for each excitation polarization, the vorticity was estimated using the optimization algorithm. The estimated vorticity ω_y shows similar trends compared to DNS data [67] which is a promising evidence for the proof of concept. However, the results are not overlapping from the repeatability studies due to the high sensitivity of the optimization algorithm and the random error from the measurement equipment. To improve this technique in the future, transient experiments have to be conducted to estimate vorticity accurately and to capture the underlying physics.

Table of contents

List of figures

List of tables

Nomenclature

Greek Symbols

ε	Angle between absorption and emission moments [radian]
η	Dynamic viscosity [$\mathrm{kg \cdot m \cdot s^{-1}}$]
γ	Constant in stretched exponential function [-]
λ_0	Laser wavelength [m]
μ_E	Excited state dipole moment [$\mathrm{A \cdot s \cdot m}$]
μ_G	Ground state dipole moment [$\mathrm{A \cdot s \cdot m}$]
ν	Kinematic viscosity [$\mathrm{m^2 \cdot s^{-1}}$]
ω	Components of vorticity [$\mathrm{s^{-1}}$]
Ω	Total vorticity [$\mathrm{s^{-1}}$]
π	$\simeq 3.14\ldots$
ϕ	Azimuthal angle [radian]
ρ_f	Density of the fluid [$\mathrm{kg \cdot m^{-3}}$]
ρ_p	Density of the particle [$\mathrm{kg \cdot m^{-3}}$]
τ_c	Correlation time [s]
τ_f	Decay lifetime [s]
τ_ff	Hydrodynamic memory effect time [s]
θ	Polar angle [radian]

Superscripts

$\ddot{x}$	double differential
grad	Gradient force
$\overline{x}$	Mean quantity
scat	Scattering force
$+$	Wall units
x'	Fluctuation

Subscripts

ext	External
f	Fluorescent light contribution
fr	Friction
grav	Gravitational force
h	Horizontally polarized laser excitation
$\parallel$	Parallel
$\perp$	Perpendicular
s	Scattered light contribution
ss	Steady state
th	Thermal
v	Vertically polarized laser excitation

Other Symbols

$2w_0$	Diameter of the laser beam [m]
k_s	Surface roughness [m]
a	Radius of cavity [m]
c	Speed of light [$\mathrm{m \cdot s^{-1}}$]
F	Force [$\mathrm{kg \cdot m \cdot s^{-2}}$]
f	Probability distribution function [-]
G	G factor [-]
H	Full width of square duct [m]
h	Half width of square duct [m]
h_p	Planck's Constant [$\mathrm{m^2 \cdot kg \cdot s^{-1}}$]
I	Intensity [-]
k	Boltzmann constant [$\mathrm{m^2 \cdot kg \cdot s^{-2} \cdot K^{-1}}$]
k_r	Radiative rate constant [$\mathrm{s^{-1}}$]
M	Electric dipole moment between two excited states [$\mathrm{C \cdot m}$]
m	Mass of the particle [kg]
n	Refractive index [-]
$n(t)$	Number of molecules [-]
P	Polarization [-]
r_0	Fundamental anisotropy [-]
r	Anisotropy [-]
r_p	Radius of the particle [m]
Re_τ	Frictional Reynolds number [-]
Re_b	Bulk Reynolds number [-]

Re	Reynolds number [-]
r_{ss}	Steady-state anisotropy [-]
T	Temperature [K]
t	Time [s]
u	Velocity of the fluid [$m \cdot s^{-1}$]
u_τ	Frictional velocity [$m \cdot s^{-1}$]
V	Volume of the particle [m^3]

Acronyms / Abbreviations

BODIPY	Meso- substituted boron dipyrromethene
CCD	Charge-Coupled Device
CCVJ	9-(2-carboxy-2-cyanovinyl)juloli- dine
DCVJ	9-(2,2-dicyanovinyl)julolidine
DEM	Discrete Element Method
DI	De-ionized
DNS	Direct Numerical Simulation
FEM	Finite Element Method
FLIP	Fluorescence Loss In Photobleaching
HAP	Heavy atom perturber
LDA	Laser Doppler Anemometry
LES	Large Eddy Simulation
NA	Numerical Aperture
PMMA	Poly(methyl methacrylate)
UV	Ultraviolet

Chapter 1

Project overview

"Turbulence is the most important unsolved problem of classical physics"

Richard P Feynman

1.1 Project context

Fluid mechanics has a variety of applications in the field of mechanical, chemical and biomedical engineering. Broadly, flows can be divided into laminar and turbulent flows. They are observed in all the sizes from extra-terrestrial flows occurring in photo-sphere of the stars to small devices like nozzles and pipes [58]. Since the turbulent flows are an indispensable part of fluid mechanics, it is very important to understand the underlying physics. However, turbulence remains an open unresolved problem for several decades [58]. Among various parameters in turbulence, concepts such as vorticity specifically, vortex stretching and the theory of energy cascade form an integral aspect of turbulence [59].
Beginning with the vorticity, it is defined as the curl of the velocity vector,

$$\vec{\omega} = \nabla \times \vec{u} \tag{1.1}$$

Consider a flow suspended with spherical nanoparticles. Then the motion of every particle in the flow can be decomposed into translation, rotation and expansion which is caused due to the flow [93]. In such a case, the vorticity can be interpreted as twice the rotation rate of the particles along principal axes in the fluid in the absence of shear deformation [74]. Alternatively, vorticity can also be interpreted as the circulation per unit area of a surface perpendicular to the vorticity field [35]. Many authors in the past have tried to compute or measure vorticity using computational and experimental tools. The experimental methods used to measure vorticity are broadly split into three categories [93]:

1. Indirect measurements of vorticity from velocity: This is done by first measuring the velocity components at multiple points in the flow which are near each other. Then, the vorticity is estimated by computing the measured velocity gradients. For example, Particle Image Velocimetry (PIV) as described by Westerweel et al. [98].

2. Direct measurements of vorticity: Methods that can directly measure the vorticity. For example, vane type vorticity meter as described by Wigeland et al. [99].

3. Measurements of flow properties other than velocity to estimate vorticity: This is done by utilizing the measurements of flow properties other than velocity such as magnetic potential in conducting fluids to estimate vorticity. For example Tsinober et al. [89].

From the 1st category, PIV has become an established prominent tool over the last three decades for visualizing instantaneous vorticity fields in turbulent flows [98]. The second category is relatively less examined compared to the first category. However, the third category is the least explored with very few ideas to measure vorticity by relating it with other properties [94]. The idea of this project, falls in the third category. In this technique, it is possible to estimate all the three vorticity components (ω_x, ω_y and ω_z) with a single field of view based on the developed mathematical formulations. This would be a major advantage compared to the previously known techniques. The concept of this technique is introduced in section 1.2.

1.2 Bird's-eye view of the concept

Consider a fluid medium with spherical nanoparticles that are sensitive to the polarized excitation. Let these nanoparticles be made of molecules that show luminescence phenomena. Luminescence is a phenomenon that occurs when the emission of light occurs from the excited states of molecule in the substance [40]. When these nanoparticles are excited with polarized light, the molecules with the absorption transition moment aligned parallel to the electric vector of the polarized excitation source have the highest probability of excitation [76]. Absorption transition moment is a vector quantity that relates the ground and the excited state using the phase vectors [53]. However, if external forces are acting on the particle that causes deterministic rotations, the percentage of molecules which are aligned in parallel to the excitation electric vector will change. This will change the emission intensities from these nanoparticles which can be utilized to indirectly estimate the vorticity.
In a nutshell, the change in the emission intensities is effectively used to measure the rotation of the particles in the fluid medium, to estimate the vorticity. All the mathematical relations involved in this proposed idea is described in detail in chapter 3.
When the population of fluorophores is excited with vertically polarized light, the emitted light will retain a percentage of polarization based on how fast it is rotating in the fluid medium [38]. Fluorophores are molecules that show luminescence phenomena. This process is called fluorescence anisotropy or fluorescence polarization. Polarization (P) and the anisotropy (r) are expressed as [38],

$$r = \frac{I_{\parallel} - I_{\perp}}{I_{\parallel} + 2I_{\perp}} \tag{1.2}$$

$$P = \frac{I_{\parallel} - I_{\perp}}{I_{\parallel} + I_{\perp}} \tag{1.3}$$

Here $I_{\parallel}$ and $I_{\perp}$ are parallel and perpendicular intensities of the polarized emission respectively, when the particles are excited with vertically polarized light.
When the particles undergo deterministic rotations, the anisotropy is expected to further reduce. The reduction in anisotropy, known as depolarization is caused due to the vorticity. Faster rotation of the particles will result

in higher depolarization of the emission. Slower rotation of the particles show higher anisotropy. In this thesis, steady-state measurements were conducted to measure phosphorescence depolarization in a canonical turbulent square duct flow caused due to vorticity. The measured depolarization was translated to vorticity for comparing with DNS results. Laminar flow was not chosen for comparison because of lower magnitudes of vorticity compared to the turbulent flows. This is justified based on the newly introduced non-dimensional numbers in subsection 3.5.3. DNS database [67] was chosen for comparison since this was also used to perform the sensitivity analysis of the analytical relations presented in chapter 3. To perform sensitivity analysis, a database of all the three vorticity components was essential. Lastly, an unconstrained optimization problem that was developed in-house, was used to estimate the vorticity from the measured phosphorescence emission intensities.

1.3 Research questions

This thesis aims to show the proof of concept of the possibility of estimating the vorticity in the fluid medium from the properties of polarization, using nanoparticles in a canonical fluid flow. To achieve this, the following sub-research questions were formulated:

1. What type of research is done by previous researchers in the fluorescence anisotropy to measure properties of the fluid flow?
2. Which experimental equipment is suitable (like camera, laser, and type of particles) to measure the anisotropy of nanoparticles?
3. What are the important parameters that affect the polarized emission from nanoparticles?
4. How can luminescence emission be employed to study the properties of the fluid that help in interpreting anisotropy?
5. How do the derived analytical correlations vary based on different input parameters ?
6. Is it possible to measure vorticity using depolarization ? How accurate are the steady-state measurements ?

1.4 Project goals

To answer the research questions, this project was divided into the following goals,

1. Conduct preliminary experiments to identify the most suitable nanoparticles.
2. Design a suitable experimental setup which includes designing the square duct and selecting the nanoparticles to benchmark depolarization based vorticity measurements.
3. Classify and elucidate the important parameters which affect the emission from the nanoparticles.
4. Perform sensitivity analysis of the derived vorticity relations using the DNS data [67].
5. Interpret the results from the conducted experiments and compare it with the DNS results.

1.5 Structure of the report

In chapter 2, the theory behind fluorescence anisotropy is elaborated with a few of its applications. Vorticity measurement techniques are described, focusing more on the unconventional procedures to measure vorticity. Lastly, a brief review of turbulence in channel and duct flows is provided to comprehend the subject of this measurement technique. In chapter 3, a detailed theory behind the experimental technique is elaborated, describing the physics involved and showing the relevant mathematical formulae. Elaborate descriptions of the concepts behind the formulation of this problem starting from the fundamental level based on the non-dimensional numbers are presented.
In chapter 4, suitable experimental equipment required for the phosphorescence anisotropy is described. In this thesis, the chosen canonical flow was a square duct flow, hence the design parameters of the square duct flow are presented. In chapter 5, an intensive study about the particles is conducted. Fluorescence and phosphorescence lifetime analysis, spectroscopic analysis and photo-bleaching studies are performed. In section 5.2, calibration procedures, fundamental anisotropy of vitrified nanoparticles and in quiescent fluid state is conducted that lay the foundation for interpretation of the turbulent flow results. The effect of viscosity and dissolved oxygen is studied using nanoparticles as probes. A set of assumptions that were made to develop this technique at the cost of accuracy of results, is listed.
In chapter 6, the variation of synthetic signals obtained from analytical correlations are studied by varying different parameters using DNS data as input [67]. The respective contours from the experiments are compared with the synthetic signals obtained from DNS data which show the drop in anisotropy. The contours are column averaged to focus on the trends observed at Re = 0, 2660, 4434 and 6208. Finally vorticity ω_y, was estimated using the optimization algorithm and repeatability studies were conducted to observe any similarity in vorticity. Lastly, the major conclusions from this project are summarized in chapter 7. Since this is the first attempt to develop this experimental technique based on the proposed hypothesis, the conducted preliminary studies in chapter 5 lay out the references to develop this technique for the future. To improve the accuracy of this technique, future recommendations in the section 7.2 are presented to the reader.

1.6 Other contributions

The experiments involved in the lifetime analysis as shown in subsection 5.1.1, mathematical formulations and the optimization problem section 3.3 to section 3.4 were developed by the author's supervisors at the Institute of Fluid Dynamics (IFD), ETH Zurich. A greater part of the setup as described in section 4.1 was built by the author's supervisor at ETH. Rest of the work in this thesis is done by the author.

1.7 Project boundaries

Since this is the first attempt to measure vorticity using depolarization, there are too many options that can be tried to make the technique work or improve the technique. However, due to logistics and time constraints, the scope of the project is bounded to a manageable size.

1.7.1 Choosing the suitable nanoparticles

This thesis was restricted to only three different types of nanoparticles (eosin Y, rhodamine and europium based chelated nanoparticles). However, spherical particles with higher lifetime could be synthesized from the specific chemical crystal dyes [12, 37] which will improve the accuracy of the results significantly.

1.7.2 Orientation of the square duct

The experiments were conducted in a vertical square duct due to ergonomic constraints. Nonetheless, turbulence is expected in vertical square duct considering sufficient development length is provided [52]. Duct flow was selected since non-planar surfaces like flow in a pipe show scattering of the excitation beam which will change its polarization inducing a systematic error in the measurements [38].

1.7.3 Post-processing

No advanced image processing algorithms were employed since the project focused on observing trends in depolarization from the experimental data. Small variations of laser shots were already accounted for in steady-state measurements with long exposure times.

1.7.4 Comparison with reference data

The analytical relations developed inhouse had to be analyzed for its sensitivity with the known three vorticity components for different Reynolds number (Re) in turbulent flows. DNS data was chosen, since the author could not find a consolidated database of three vorticity components from previous measurements like PIV for different Re, in turbulent duct flows.

1.8 Methodology

The physics behind the main concept in this thesis has not been researched in the past. Hence it becomes quite critical for the readers to understand this concept thoroughly for the necessary constructive criticism that will help the technique to develop over the years. Figure 1.1 shows the two approaches used in this thesis.
The flow shown by the red arrows show a direct straight approach (approach 1). The dotted green arrows show the reverse-engineered approach to conduct a sensitivity analysis of the analytical model correlations (approach 2). Both the approaches are based on the concept introduced in section 1.2. Approach 1 is a straight forward method that uses the experimental results as an input to the analytical model correlations. This was further used in the optimization model to obtain vorticity. Approach 2 begins by using the known DNS vorticity results [67] as the input to the straightforward analytical correlations to obtain the synthetic signals. These synthetic signals should show similar trends as experimental results for the highest accuracy of vorticity data. Approach 2 was used to perform the sensitivity analysis of the analytical correlations as described in Appendix D. The final goal was to interpret both the results from the two approaches, which are marked in purple boxes.
An experimental methodology was developed during this thesis considering the analytical model and the budget constraints. The author mentions at least a few failed iterations for the researchers who might want to develop this technique in the future. Since the analytical model correlations and the optimization problem are based on the new concept, it becomes quite relevant to conduct their sensitivity analysis to study their variation with different parameters.

The problem formulation is discussed in chapter 3. The preliminary experiments and anisotropy measurements were conducted to lay the foundation required to comprehend this technique as shown in chapter 5. Lastly, the applicability of this technique was shown in chapter 6

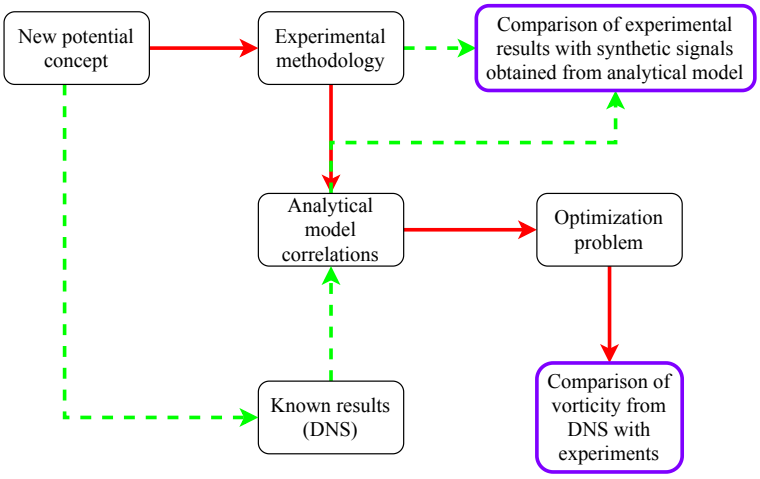

Fig. 1.1 Two approaches were undertaken in this thesis to understand the underlying physics. Approach 1 (arrows in red) employs the measurement results from the experiments in the analytical model correlations. Using these as an input for the optimization problem to estimate the vorticity to compare it with the DNS data. Approach 2 (arrows in green) elaborates on using the known DNS results as user input in the analytical model correlations to study their sensitivity and compare the synthetic signals with the experimental results.

Chapter 2

Introduction

In this chapter, basic theory behind fluorescence anisotropy and various applications of fluorescence anisotropy is presented in section 2.1. A brief introduction to various vorticity measurement techniques is provided and some of their shortcomings are discussed in section 2.2. Lastly, a concise history of the advancements in the estimation of vorticity via computational and experimental methods in a turbulent channel/duct flows is reported in section 2.3.
Since this is the first attempt to estimate vorticity from depolarization, the author could not find any past literature elaborating on the underlying physics. Hence, a detailed theory behind this idea is elucidated in chapter 3.

2.1 Fluorescence anisotropy

Fluorescence anisotropy is an established field with various applications in the field of biomedical engineering from drug discovery to early diagnostics of various diseases [106]. But, the field of fluorescence anisotropy has not set its foot in the field of fluid dynamics. To understand this thesis, the relevant theory behind fluorescence anisotropy (polarization) is elaborated in subsection 2.1.1. Different types of fluorescence anisotropy measurements and their overview is presented in subsection 2.1.2. Lastly different applications of fluorescence anisotropy is described in the subsection 2.1.3

2.1.1 Theory of fluorescence

Luminescence is a phenomenon that occurs when the emission of light occurs from the excited states of a molecule. Natural phenomena like aurora borealis, emission of light from the bacteria in the sea are the common luminescence phenomena [8]. Consider a molecule that can get excited by absorbing electromagnetic radiation depending on its properties. After its excitation, an electron returning to the ground state releases its energy in the form of a photon. Generally, the emitted photon will have lower energy and longer wavelength compared to the absorbed radiation. This phenomenon is called Stokes shift [40]. To understand the various processes that can occur inside a molecule, Jablonski diagram as shown in Figure 2.1a is used. It explains the various transitions that occur between the excitation and emission spectrum [40]. S_1 and S_2 are the first and second quantum singlet states, T_1 is the first triplet state and the vibrational levels at each of the electronic states are represented as 0,1,2 .. n [24]. Broadly, luminescence can be segregated into two types, fluorescence and phosphorescence depending on the nature of excitation, the timescales of emission and the substance

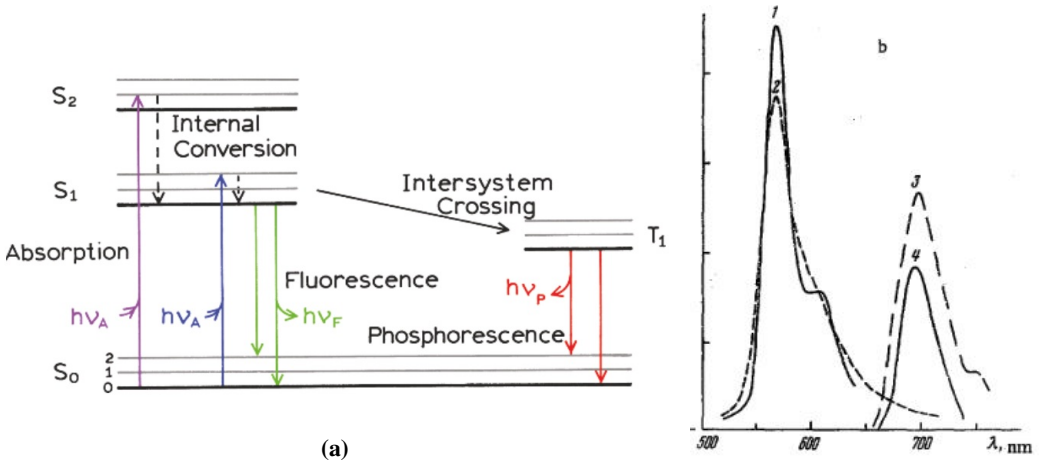

Fig. 2.1 Jablonski diagram as shown in Fig (a) show various processes happening when luminescence particles are excited [40]. S_0, S_1 and S_2 are the singlet states, T_1 is the triplet state. The vibrational levels at each of the electronic state are represented as 0,1,2 .. n. from [36]. Fig. (b) shows the intensity curves showing fluorescence and phosphorescence of rhodamine [36]. The peaks 1 and 2 are the fluorescence peaks. The peaks 3 and 4 are the phosphorescence peaks. However, the peaks 3 and 4 are magnified by 8000 times.

itself. Fluorescence is the emission of a photon from singlet states (predominantly from 1st singlet state) and phosphorescence is the emission of a photon from triplet state as shown in Figure 2.1a [40].

The time scale for light absorption is about 10^{-15} seconds. Most molecules return to the ground state of their respective electronic states in about 10^{-12} seconds to reach momentary equilibrium [83]. The lifetimes of fluorescence which also includes delayed fluorescence ranges from 10^{-9} to 10^{-6} seconds. Luminescence lifetime is defined as the average time spent by the molecule in an excited state before returning to the ground state [38]. The lifetime of phosphorescence ranges from 10^{-6} to 10 seconds [83]. The absorption bands are smaller for triplet excited state which reduces the the population of phosphorophores resulting in lower quantum yield [76]. Quantum yield (ϕ_y) is defined as the ratio of the number of photons emitted to the number of photons absorbed [84].

In the past, Kuznetsov et al. [36] conducted spectroscopy experiments to compute bands of fluorescence and phosphorescence. Figure 2.1b shows the spectrum of rhodamine 6G in water at 298 K. The peaks 1 and 2 are the fluorescence peaks. The peaks 3 and 4 are the phosphorescence peaks. However, the peaks 3 and 4 are magnified by 8000 times. Using this, fluorescence or phosphorescence spectrum bands could be estimated.

Quantum yield can also be defined as [44],

$$\phi_y = \frac{k_r}{k_r + k_{nr}} \tag{2.1}$$

Here, k_r is the rate constant of fluorescence and phosphorescence. k_{nr} is the rate constant of all the non-radiative deactivation processes which are elaborated. Many deactivation processes result in the transition from an excited state to a ground state. Vibrational relaxation is a rapid process resulting in the transition to the lowest vibrational level of the molecule due to the collision of molecules with the excited species and the solvent medium [27]. Internal conversion is the process that occurs when there is a transition from a higher excited state to a lower excited state without the emission of radiation. This process can also occur between S_0 and S_1 depending on the type of the molecule as shown in Figure 2.1a. But the probability of its occurrence is low [40]. External conversion can occur due to the interaction of the excited molecule with the surrounding medium

which results in the energy transfer. Temperature also affects the mobility of the fluorophores resulting in lower anisotropy [22]. The influence of the temperature on excitation and emission processes is quite difficult to control [107]. Solvent polarity also plays an important role in decreasing the energy of emission spectra due to the stabilization of the excited molecules in polar solvents [39]. Multiple effects acting simultaneously on these particles, result in lower quantum yield. No single theory can be applied to understand the effects of the environment on the fluorophores.

Fluorescence quenching also decreases the fluorescence intensity of the sample. Ware [96] describes oxygen quenching as, the reaction of the oxygen with excited fluorophores or phosphorophores causing de-excitation of the molecules and leading to form a chemical complex. Molecular interactions such as excited state reactions, ground-state complex formation, collisional quenching are the main reasons for quenching [96]. The inter-system crossing is a phenomenon that occurs when there is a crossover from singlet state to triplet state (S_1 to T_1) [83]. Inter-system crossing is observed often in molecules with heavy atoms such as Iodine and Bromine.

Since the idea behind this project is to measure the depolarization due to vorticity, it is important to list some of the common depolarization sources. Most of the factors which cause depolarization in the decreasing order of its magnitude are rotational diffusion, Resonance Energy Transfer (RET) from the solutions, the turbidity of the solutions, Brownian motion, radiative transfer, light scattering, re-absorption, and misalignment of the polarizers [38]. Rotational diffusion is a process by which the equilibrium statistical distribution of the overall orientation of the molecules inside the particles is restored [65]. Radiative transfer is a process that involves reabsorption of emitted photons by the fluorophores. Radiative transfer depends on non-molecular optical properties of the sample, size of the sample container and the optical densities of the sample [38]. Further discussion about the rotational diffusion timescale is presented in subsection 3.5.3.

To understand the depolarization effects on the nano-particles, a set of experiments was conducted as described in chapter 5. These experiments help in the interpretation of square duct flow anisotropy measurements in chapter 6.

2.1.2 Types of measurements

According to Lakowicz [38], there are two common types of anisotropy measurements. Steady-state measurements are performed with constant illumination. When the sample is illuminated with a continuous laser beam, the emission spectrum is recorded. Steady-state is reached almost immediately because the timescale of fluorescence is in the nanoseconds. Time-resolved measurements are the second type of measurement where the pulse width of the laser is significantly shorter than the decay time of the sample to capture the transient behavior of the particles.

A steady-state measurement is the average of time-resolved phenomena over the intensity decay of the sample. Considering the fluorophore with decay lifetime (τ_f) and correlation time (τ_c), the intensity and anisotropy decays are given by [40],

$$I(t) = I_0 e^{-t/\tau_f} \tag{2.2}$$

$$r(t) = r_0 e^{-t/\tau_c} \tag{2.3}$$

Decay lifetime (τ_f) is the average time spent by the molecule in the excited state before returning to the ground state. Correlation time (τ_c) is the average time required for the molecules aligned with respect to the excitation polarization to reach random distribution at equilibrium. Where I_0, r_0 are the intensity and anisotropy at $t = 0$

immediately following the excitation pulse. The correlation time of the particles is expressed as

$$\tau_c = \frac{\eta V}{RT} \tag{2.4}$$

Here η is the viscosity of the fluid, V is the volume of the rotating molecule, R is the universal gas constant and T is the temperature in Kelvin. The steady state anisotropy (r_{ss}) is given by,

$$r_{ss} = \frac{\int_0^\infty r(t)I(t)dt}{\int_0^\infty I(t)dt} \tag{2.5}$$

The steady state anisotropy is normalized with total intensity. The steady state intensity (I_{ss}) could also be related to the decay time as

$$I_{ss} = \int_0^\infty I_0 e^{-t/\tau_f} dt = I_0 \tau_f \tag{2.6}$$

Steady-state anisotropy does not reveal complete information regarding the molecule shape and its orientation. If a molecule has two decay lifetimes, then the steady-state intensity will reveal the weighted average intensity from the whole molecule [38].

In fluorescence experiments, a blank sample is studied to detect Raman scattering [82], Rayleigh scattering [105] and stray scattering from other sources. A blank sample is identical to the sample without any fluorophores. Using a blank sample in the polarization experiments helps in identifying the erroneous scattering sources. Scattering solutions are used to calibrate the excitation source polarization. Colloidal silica solution is generally used to mimic the scattering solution [87]. However, scattering from sources other than the fluorophores like background or dirt inside the fluid can cause erroneous polarization. The actual observed anisotropy is given by [38],

$$r_{obs} = f_s r_s + f_f r_f \tag{2.7}$$

Where f_s is fractional contribution from scattered light, f_f is contribution from fluorescent light, r_s and r_f are anisotropy of scattered light and fluorescent light. Due to the above reasons, polarization experiments are highly dependent on the precise geometry of the setup and the optical density of the sample.

2.1.3 Applications of steady-state fluorescence anisotropy

Few researchers have applied steady-state fluorescence anisotropy technique to measure the properties of the fluid, like viscosity. Levitt et al. [43] conducted fluorescence anisotropy measurements with fluorescent molecular rotors. Levitt et al. considered fluorophores like BODIPY (meso- substituted boron dipyrromethene), CCVJ (9-(2-carboxy-2-cyanovinyl) juloli- dine) and DCVJ (9-(2,2-dicyanovinyl) julolidine) as probes of apparent viscosity to study the variation of anisotropy with viscosity. Similar studies were conducted in subsection 5.2.3, to study the dependence of viscosity on the anisotropy of europium based particles and to check if they behave similar to molecular rotors.

Lee et al. [42] discussed various applications of fluorescent molecular rotors as micro-viscosity probes. Bui et al. [14] studied Terbium (Tb) based complexes as optical viscosity probes. They observed a four-fold increase in luminescence lifetime and quantum yield for a range of viscosity (0.6-1200 cP). The main reason claimed by Bui et al. for this to occur was that higher viscosity fluids impede the rotations of the luminescent molecules which decreases the non-radiative decay and increases the quantum yield. Here, non-radiative decay loss is defined as loss of energy via collisions with external medium and vibrations [76]. Walter et al. [95] proved

that the variation of quantum yield of europium based nanoparticles due to the dissolved oxygen does not vary. Similar studies were conducted to verify the proposed physics with in subsection 5.2.4.

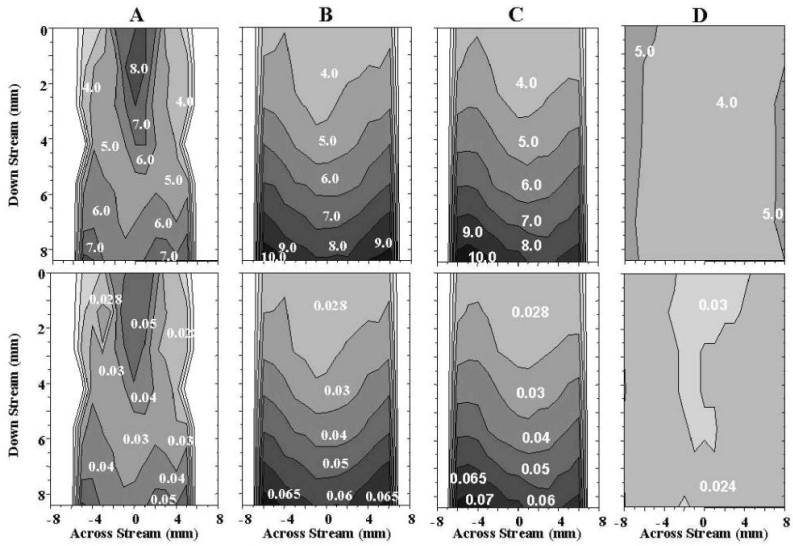

Fig. 2.2 Inter-Molecular alignment maps of polarization on the top and anisotropy in the bottom for (A) pure liquid MEG flow (B) 0.35×10^{-3} mol $\cdot$ L^{-1} SDS surfactant solution; (C) 4×10^{-3} mol $\cdot$ L^{-1} SDS surfactant solution; and (D) 3.5×10^{-3} mol $\cdot$ L^{-1} PEO surfactant solution [68].

An automatic method was designed by Quintella et al. [68] with closed-loop self-control to obtain anisotropy maps of liquid films to study the variation of molecular alignment with anisotropy. The study was conducted on liquid film of Monoethlyene Glycol (MEG) on borosilicate with surfactants like Sodium Dodecyl Sulfate (SDS) and PolyEthylene Oxide (PEO) at sub-micellar concentrations. Figure 2.2 shows the polarization and anisotropy maps of pure MEG, MEG and SDS surfactant, MEG and PEO surfactant. Pure MEG showed low anisotropy due to strong interactions with boro-silicate. The addition of SDS leads to weaker interfacial tension, ensuring the alignment of molecules along the flow. When PEO was added, the long chains of PEO interacted with small MEG molecules causing disturbance in inter-molecular networks and misalignment of molecular domains. These effects caused a decrease in anisotropy and polarization as shown in Figure 2.2 (D).
Very few authors have tried to relate the properties of the flow like velocity, vorticity with the polarization. Kenyon et al. [28] employed fluorescence polarization to study a laminar jet of Rhodamine 6G dye in ethylene glycol. The change in the degree of polarization was observed in the laminar jet due to the presence of shear forces within the jet.

Polarization profiles were observed every 0.5 mm along the jet. The polarization 3-D map is shown in Figure 2.3. Two broad polarization peaks separated by a small distance were observed near the nozzle and a gradual increase of polarization was increased downstream. This indicated that the liquid is depleted at the center and forced to the edges, implying higher molecular alignment along the edges. In conclusion, Kenyon et al. claimed that the reason for higher polarization is due to the inhibition of the rotation of dye molecules caused by larger shear forces. Quintella et al. [69] conducted similar measurements with non-spherical fluorophore dyes inside a nozzle to observe the variation of polarization and compare it with the velocity of the flow as shown in Figure 2.4. They observed similar trends showing higher polarization at the nozzle exit which has a higher velocity. However, no background analytical relations relating to shear forces and polarization were presented to support this hypothesis. In this thesis, analytical correlations were presented to relate the

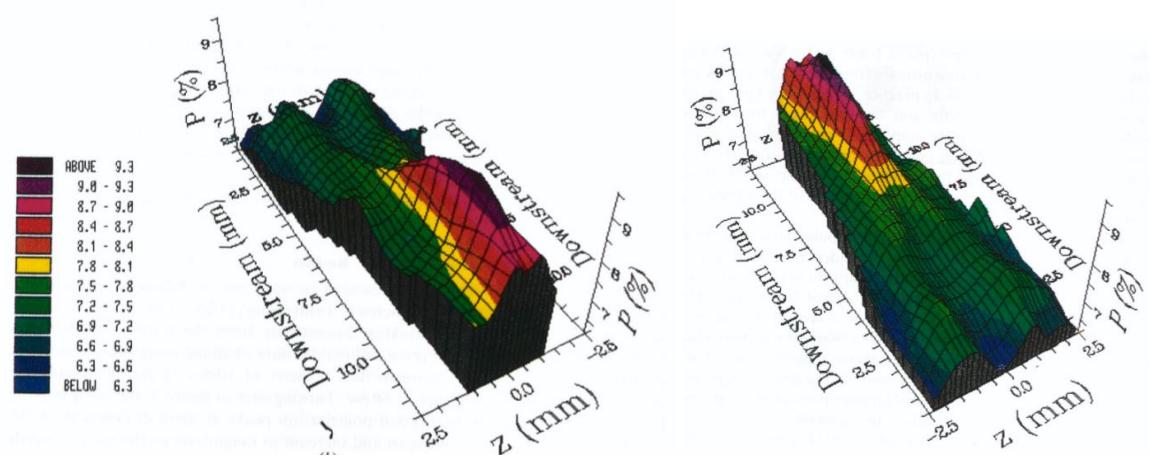

Fig. 2.3 Polarization map looking towards the nozzle and looking downstream at 30 psi. A gradual increase in polarization is observed downstream of the nozzle [29].

anisotropy with vorticity in the square duct flow. The effect of shear forces is not accounted in this thesis.
In this project, spherical phosphorescent particles were chosen to observe the variation of polarization with vorticity along the edges of the square duct. Spherical particles were chosen because of the assumption that the rotation is the same for each molecule by ensuring the observation area as a particle comprising of many molecules inside. If the particles have a different shape like crystal or dye, the rotation expected to produce due to vorticity would be asymmetric which has to be specially accounted in the theory presented in chapter 3. However, this is beyond the scope of this thesis.

2.2 Vorticity measurement techniques

In this section, some of the measurement techniques used in the past to obtain vorticity are elaborated. Besides the categories of vorticity measurement techniques described in section 1.1, broadly it can also be divided into intrusive methods as described in subsection 2.2.1 and non-intrusive methods as listed in subsection 2.2.2.

2.2.1 Intrusive techniques

Intrusive techniques are those that measure the properties of the flow like vorticity by influencing the flow. Depending on the shape and size of the device, the impact of the device on the flow will vary. The main parameters of a measurement device are spatial resolution, temporal resolution, and accuracy [94].

Kovasznay [33] was one of the first authors to measure stream-wise vorticity by introducing the concept of 'vorticity meter' employing hot wire sensors. Figure 2.5 shows the photograph of the four-probe Wheatstone bridge [33]. Using a four-probe hot wire sensor as a Wheatstone bridge, the vorticity was estimated using voltage fluctuations by employing mathematical relations. Wyngaard [102] modified this probe to an eight sensor probe for improving the spatial resolution of vorticity. Wyngaard [102] presented optimum sensor separation as 2-4 Kolmogorov lengths for higher accuracy of vorticity results. Kock am Brink and Foss [32] used an eight sensor array to measure stream-wise vorticity to improve the resolution.
Kastrinakis [26] used two Kovasznay probes to measure the RMS distribution of the stream-wise vorticity along

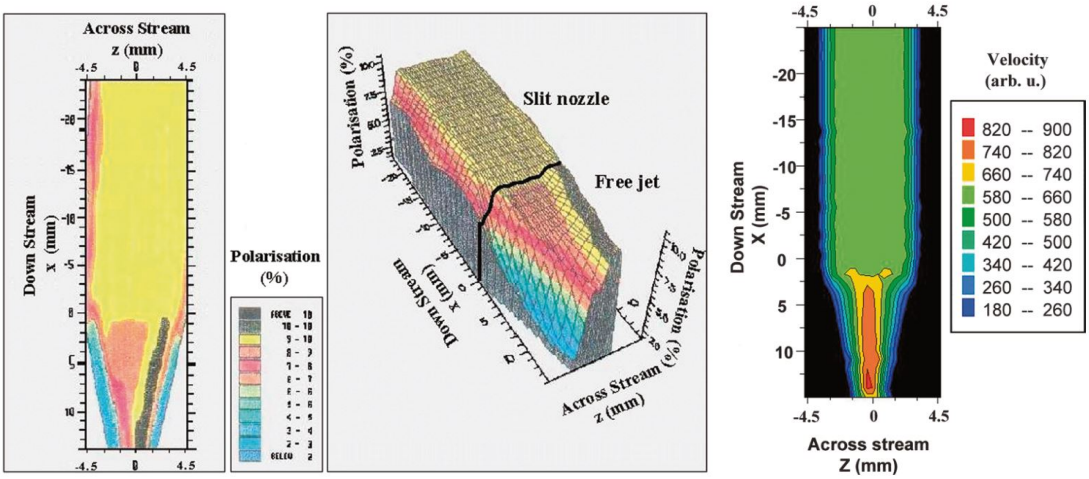

Fig. 2.4 Polarization and relative velocity of the flow inside the nozzle. Higher polarization is observed with regions of higher velocity [69].

a fully developed channel flow. Accuracy of the vorticity was improved using multiple probes by correcting the vorticity measured by a single probe. Many other authors also attempted to increase the accuracy of the experiments like Tagawa et al. [85] who changed the design of the vorticity probe to X-shape. All the previous measurements depend on the design of the probe. There were many attempts in the past to measure two and three components vorticity simultaneously. Kim and Fiedler [31] designed the six sensor probe to compute two out of three vorticity components simultaneously. Figure 2.6 shows the photograph of the six sensor probe which was used in the mixing layer.

Wassman and Wallace [97] attempted to measure all three components of vorticity using a nine sensor probe. This is shown in Figure 2.7. But they faced a lot of electrical cross talk and thermal cross talk problems causing erroneous results. To simplify the design, Vukoslavčević and Wallace[92] built a 9 sensor probe and reduced the resistance and overheat ratio to solve the above problems. However, the correlation coefficient obtained from the nine sensor probe was low. Hence a 12 sensor probe was built and tested by Ong and Wallace [62] which improved the correlation coefficient.

Wigeland et al. [99] constructed a vane-vorticity indicator that consisted of four perpendicular blades and is designed to rotate about its axis on a high-speed steel shaft, as shown in the Figure 2.8 photographs. The blades of each vane were made very thin in order to minimize the moment of inertia and to increase its sensitivity. Placing one of these vanes in the flow ensured the alignment of the rotation axis with the mean flow direction and the rotation of the vane indicated the rotating component of the flow. This rotation was related to the vorticity of the flow with careful calibration.

Vorticity was also estimated indirectly by measuring other quantities like electric potential. Tsinober et al. [89] tried to measure vorticity in the presence of the magnetic field in conducting fluids. Seven electrode probe was used to measure electric potential in near proximity and using central differences of the electric potential vorticity was estimated depending on the magnitude of the magnetic field.

After the advent of better technology leading to better experimental equipment, the measurement techniques extensively progressed in the direction of non-intrusive visualization based methods which are elaborated below.

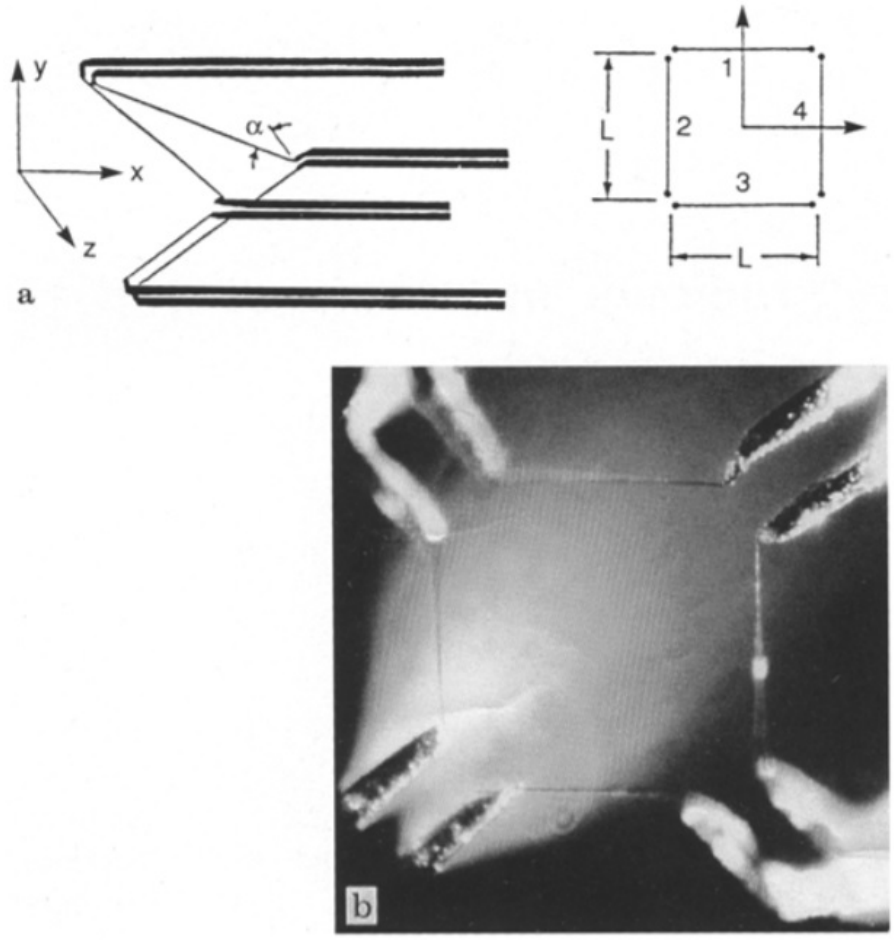

Fig. 2.5 a) The sketch of vorticity meter from Kovasznay [33] b) Stream-wise vorticity meter photograph [64].

2.2.2 Non-intrusive techniques

Non-intrusive techniques are those methods that measure vorticity without any influence on the flow. Some of the commonly established measurement techniques which are used generally to compute vorticity from velocity gradients in fluid flows are Particle Image Velocimetry (PIV) [98, 1, 3], Laser Doppler Anemometry (LDA) [63, 41, 4] and scalar imaging [88]. Over the years, some of the researchers attempted to measure vorticity by employing unconventional methods which are listed below.

Frish and Webb [21] developed a unique approach to measure the vorticity directly by employing small plastic particles with planar embedded mirrors inside the flow. Small spherical particles rotate with an angular velocity equal to half of the vorticity inside the flow. A beam of laser light that is reflected from these particles was detected by an optical system that translates the rotation of the particles to vorticity.

Recently, Ryabtsev et al. [75] devised a new method to directly measure vorticity using a rotating Doppler effect. The angular Doppler effect was observed when a frequency shift of the laser beam due to the energy exchange between the rotating optical element and circularly polarized light beam. This beam possesses orbital angular momentum which has spatial modulation of beam front. Ryabtsev et al. measured the vorticity in a fluid flow using micron-sized particles as rotating optical elements. The experimental setup is shown in

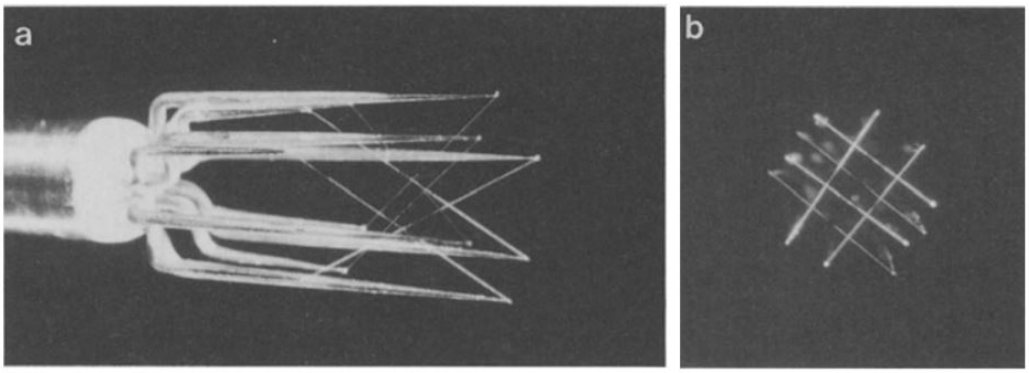

Fig. 2.6 Six sensor vorticity probe photographs [31].

Figure 2.9. The cylindrical container was rotated a few times to ensure steady flow and further to ensure a pure solid body rotation velocity field $u = r \times \omega$. The solid-body rotation was chosen as it is the simplest to create and characterize velocity and vorticity fields.
Based on the previous research on some of the unconventional procedures of vorticity measurement techniques, very few researchers have tried to estimate vorticity by measuring other quantities. The scope of this project was the estimation of vorticity by measuring anisotropy or polarization. The accuracy of the estimation of vorticity cannot be compared with full scale developed techniques like PIV since the scope of this thesis is laying out suitable guidelines to carry forward this research and attempting to prove the proof of concept behind this idea. Since this is the first ever attempt to work on this concept, there are no previous research papers that could be referred, for the interpretation of the results from this thesis.

2.3 Turbulent channel and duct flows

Channel flow is the flow of any fluid in between the parallel walls [61]. Channel flow is one of the main types of flow which is studied extensively by fluid dynamics researchers to understand wall-bounded turbulent flows. Generally, to show the proof of concept for a new measurement technique, canonical flows are studied and experimented. In this thesis, 3-D channel/square duct flow was considered due to the following reasons:

1. Round surfaces behave as specular surfaces that present different angles with respect to the excitation source due to its curvature [71, 49]. Due to the curvature, the reflected angles will have different polarization making it harder to account for, in polarization based measurements. To avoid this additional degree of freedom for the proof of concept of this measurement technique, duct flow were chosen.

2. Adequate availability of literature for designing the square duct to ensure the development of turbulence.

Nikuradse [61] and Reichardt [72] were among the first authors who introduced the turbulent flows in channels. Over the past decades, turbulence in channel flows is being studied using advanced numerical computations like Finite Volume Methods (FVM), Finite Element Methods (FEM), Direct Numerical Simulations (DNS) [108], and Large Eddy Simulations (LES) [103]. Experimental techniques are being continuously developed to study different types of flow for the understanding of turbulence characteristics. A brief description of various methods and techniques used to understand the channel flows is given below. The subsection 2.3.1 elaborates on

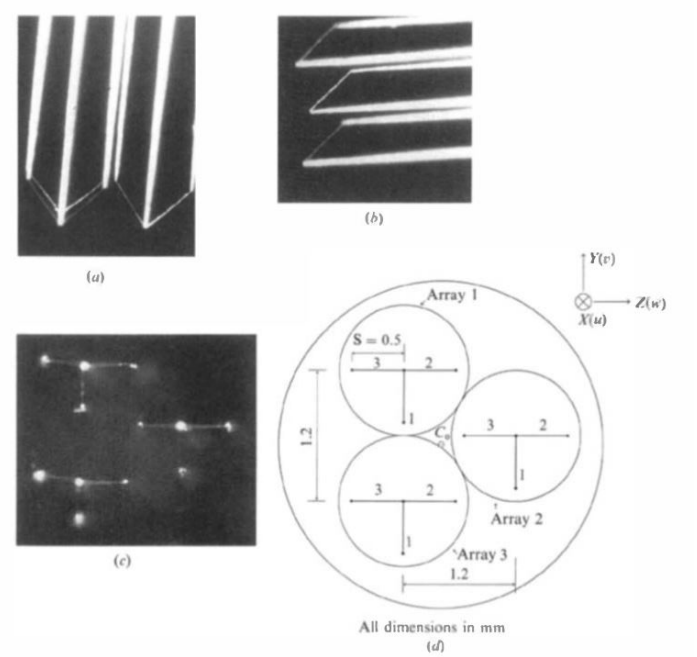

Fig. 2.7 Nine sensor vorticity probe photographs [31].

some of the important computational methodologies used in the past to compute vorticity. The subsection 2.3.2 describes the previous experimental methods to study the vorticity in channel flows.

2.3.1 Computational methods

The advancement of computational resources has increased the precision of simulated results. Kim et al. [30] were one of the first few authors who generated a comprehensive database by performing simulations on turbulent channel flows. This database was consolidated for qualitative and quantitative comparisons with new experimental or computational techniques.

Zhu et al. [108] performed DNS in a square duct at Re = 600 to compute the root mean square, flatness, and skewness of velocity fluctuations along the wall bisectors. Yao et al. [103] conducted LES in duct flows for Reynolds number from 4410 to 250000. Mean secondary flow showed the existence of two counter-rotating vortices in each corner of the duct. Modesti and Pirozzoli [51] ran DNS to study the effect of Reynolds number and Mach number on compressible isothermal channel flow. Vinuesa et al. [90] employed a new convergence criterion for the DNS in channel and duct flows. For channel flows, a convergence indicator was defined based on the deviation of total shear stress from the linear profile. For duct flows, deviation in the stream-wise momentum balance was measured. Figure 2.10 shows the velocity and vorticity contours for two different Reynolds numbers. Figure 2.11 shows the variation of velocity and vorticity for different aspect ratios.
Most of the past literature performed DNS to mimic the 2D channel flow by applying two boundary conditions on the top and bottom wall and applying periodic boundary conditions on the other two walls. However authors like Pirozzoli et al. [67] performed DNS computations with a duct flow geometry. This was ensured by enforcing boundary conditions on all the four walls of the channel. Figure 2.12 shows the vorticity contours for one-quarter of the square duct about x, y and z axis for Re = 4410. Pinelli et al. [66] also performed DNS in a duct flow to understand the Prandtl secondary motion of the second kind. Figure 2.13 shows the averaged

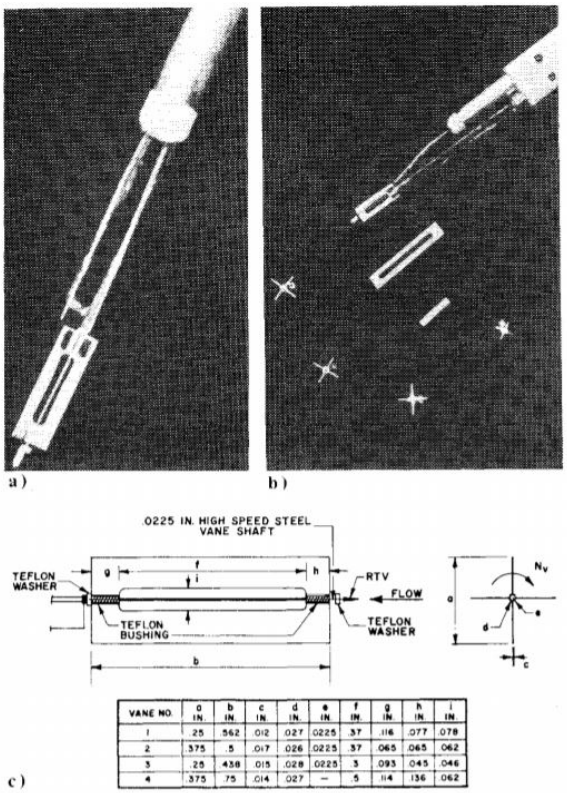

VANE NO.	a IN.	b IN.	c IN.	d IN.	e IN.	f IN.	g IN.	h IN.	i IN.
1	.25	.562	.012	.027	.0225	.37	.116	.077	.078
2	.375	.5	.017	.026	.0225	.37	.065	.065	.062
3	.25	.438	.015	.028	.0225	.3	.093	.045	.046
4	.375	.75	.014	.027	–	.5	.114	.136	.062

Fig. 2.8 a) Vane vorticity indicator probe b) Photographs of different sizes of vanes c) Schematic of vorticity indicator vanes and dimensions in inches [99].

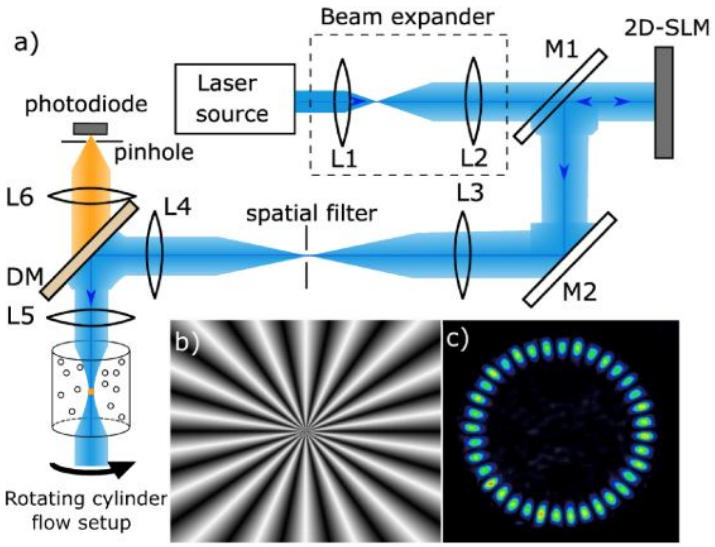

Fig. 2.9 a) Experimental setup where L1-6 are lenses and M1-2 are mirrors and DM is the dichroic mirror. b) Laguerre Gaussian light with +18 modes c) Result of the beam structure illuminated from the particles [75].

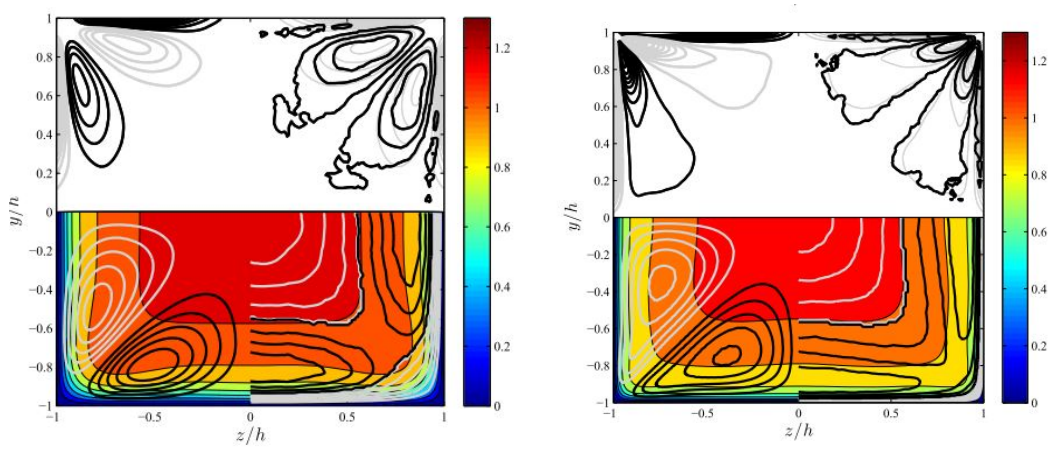

Fig. 2.10 In plane flow for Re_τ = 180 (left) and 360 (right). Lower half showing stream-wise velocity with streamlines in the lower left and lower right as vortex location. The upper left half shows the mean stream-wise vorticity ω_x where grey lines indicate negative vorticity and black lines indicate positive vorticity. Upper right half indicate the vorticity in grey ω_x and in black the probability distribution function of vortex locations with positive and negative stream-wise vorticity [90].

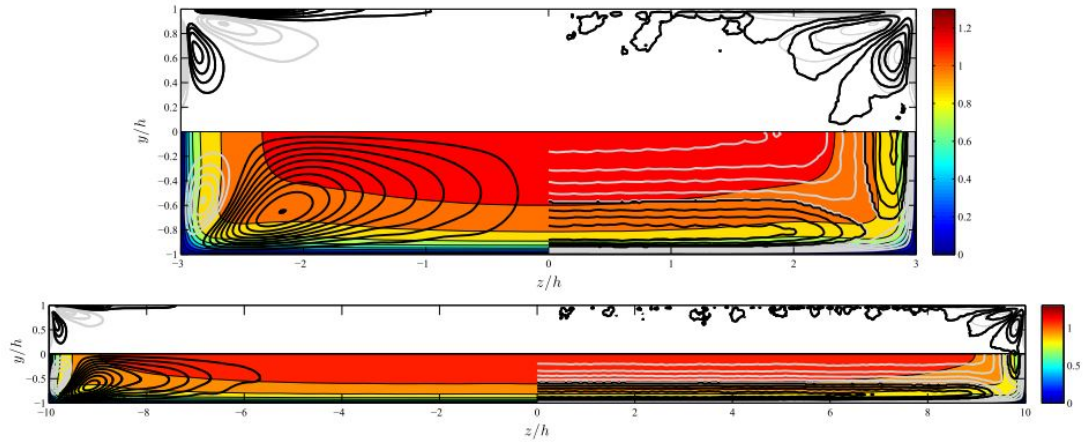

Fig. 2.11 The upper left half shows the mean stream-wise vorticity ω_x where grey lines indicate negative vorticity and black lines indicate positive vorticity. Upper right half indicates the vorticity in grey ω_x and in black the probability distribution function of vortex locations with positive and negative stream-wise vorticity. In-plane flow for aspect ratio = 3 (Top) and 10 (bottom) as Figure 2.10 [90].

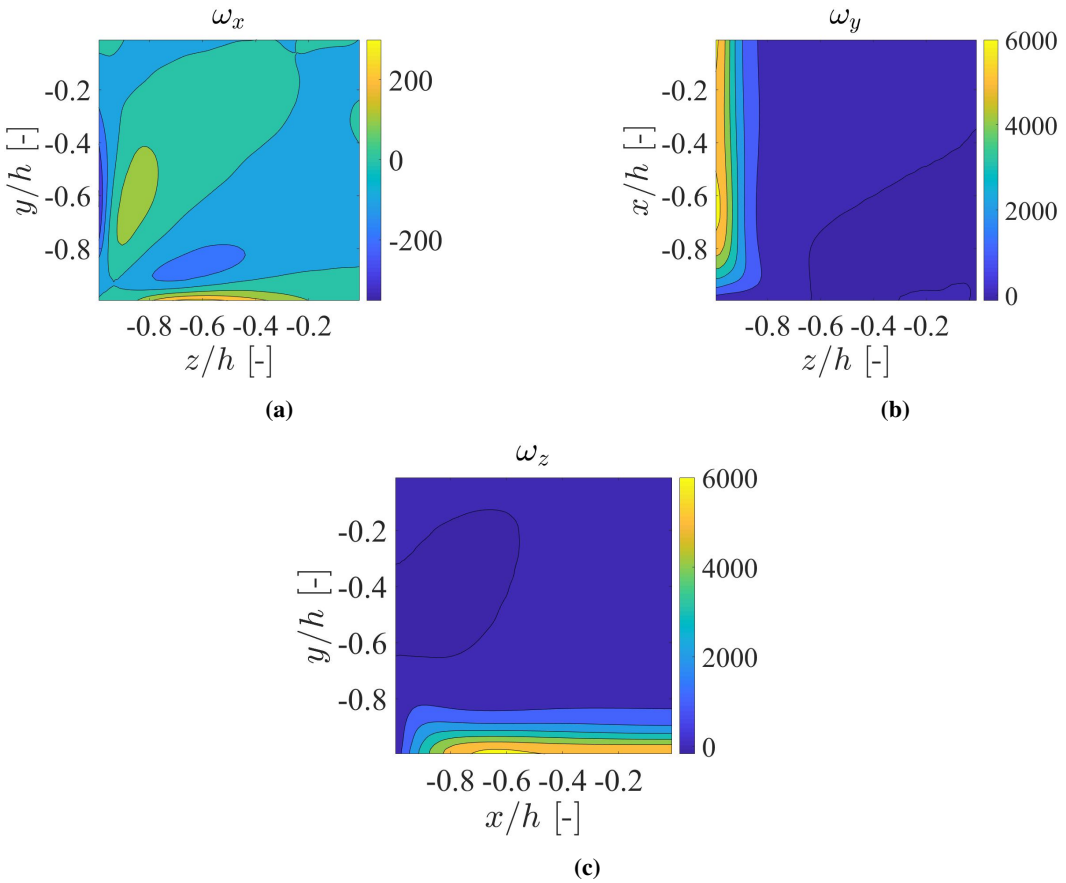

Fig. 2.12 DNS vorticity contours for one quarter of the square duct at Re = 4410. Fig (a), Fig (b) and Fig (c) shows the vorticity contours about x, y and z direction. They were plotted from the DNS database published by Pirozzoli et al. [67]. $h = 2$ mm, is the half width of the square duct.

vorticity contour for three different Reynolds number cases. These show that the boundary layer reduces with an increase in Re.

Pirozzoli et al. square duct DNS results were used in this thesis for the comparison of experimental data. Square duct flow was chosen due to logistics constraints in the availability of the pump with higher capacity. Larger the cross-section of the duct, higher the pump capacity was required to achieve the same Re.

2.3.2 Experimental methods

Various experimental techniques have been employed in duct flows to understand the flow characteristics in a high Re flow. Brundrett and Baines [13] employed a constant current hot wire anemometer to compute the parameters of secondary flow and Reynolds stress tensor inside the square duct. All the results were made dimensionless using characteristic length L and average shear velocity. Figure 2.14 shows the vorticity contour obtained inside the square duct. In the last few decades, non-visualization based techniques like Particle Image Velocimetry (PIV) have been used extensively to study turbulent flows. Adrian [3] elaborated the use of PIV to measure vorticity or strain rate tensor. One of the main parameters which needs to be considered is the mean spacing between the particles with respect to the Taylor micro-scale. Sufficiently high data density will help in

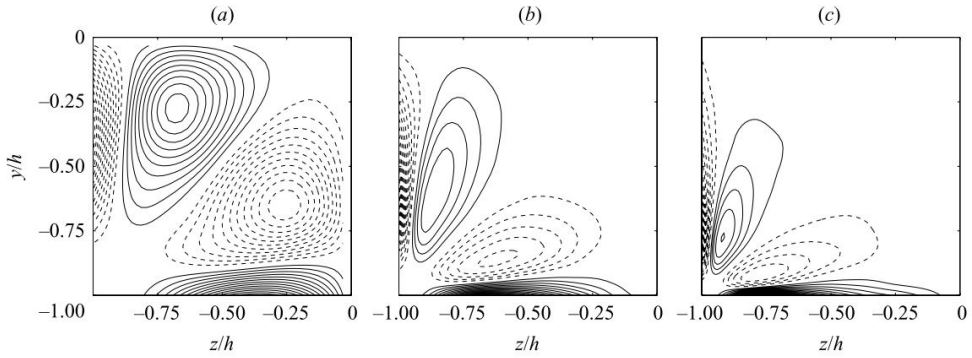

Fig. 2.13 Iso-contours of average x-direction vorticity averaged over 30 quadrants dashed lines represent negative values continuous lines represent positive values at different bulk Re_b. (a) Re_b = 1077 (b) Re_b = 2205 (c) Re_b =3500 [66].

the differentiation of the data points to compute vorticity. Gabor [23] introduced wave-front reconstruction

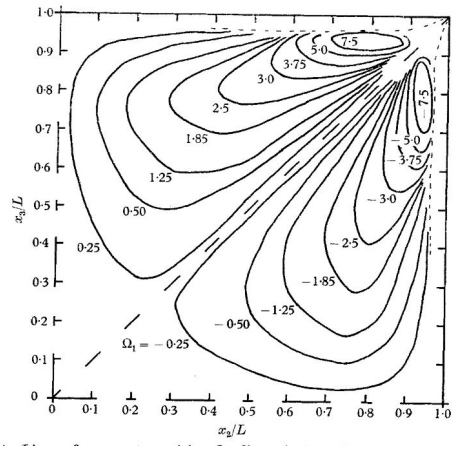

Fig. 2.14 Lines of constant vorticity for flow in square duct L = 2.5 in., duct centre line velocity U_{CL} = 28.5 ft./sec, average velocity U_{av} = 22.9 ft./sec, Reynolds number = 60,000 [13].

which was used in Holography. The hologram contains information about both phase and amplitude of diffracted waves that help in image construction. Tao et al. [86] employed this holographic velocimetry to measure a 3D velocity field. The velocity field was further filtered with a spatial box to obtain filtered strain rate and vorticity in fully developed turbulent duct flow. Recent developments in PIV are time-resolved PIV [25], stereo-PIV [100, 91], holographic PIV [7, 48], statistical PIV [2, 70] and Tomographic PIV [19, 78, 79]. These techniques can show instantaneous vorticity fields, although these techniques compute vorticity from the measured components of velocity. In this thesis, an unconventional attempt is made to develop a measurement technique which can estimate all the three components of vorticity using anisotropy in a turbulent duct flow with a single field of view.

Since this is the first attempt to formulate the proof of concept and to estimate vorticity using polarization imaging, no previous literature is available to support the hypothesis of the project. Hence, to develop the problem statement from baseline, elaborate physics and mathematical formulations behind this concept are described in chapter 3.

Chapter 3

Theory

In this chapter, the theory introduced in section 1.1 is elaborated with the mathematical relations behind the physics of the problem. The section 3.1 shows the derivation of averaged intensity signal for the particles in the quiescent state. The section 3.2 relates the variation of fundamental anisotropy of the particles r_0 with the angle between the absorption and emission transition moments ε. The section 3.3 explains the theory behind the derivation of synthetic signals formulae. The section 3.4 briefly describes the physics behind the optimization problem which was used to translate the experimental results to vorticity. Lastly, section 3.5 elucidates the problem based on the schematic diagram with necessary non-dimensional numbers and timescales involved and the assumptions used to develop the analytical signals.

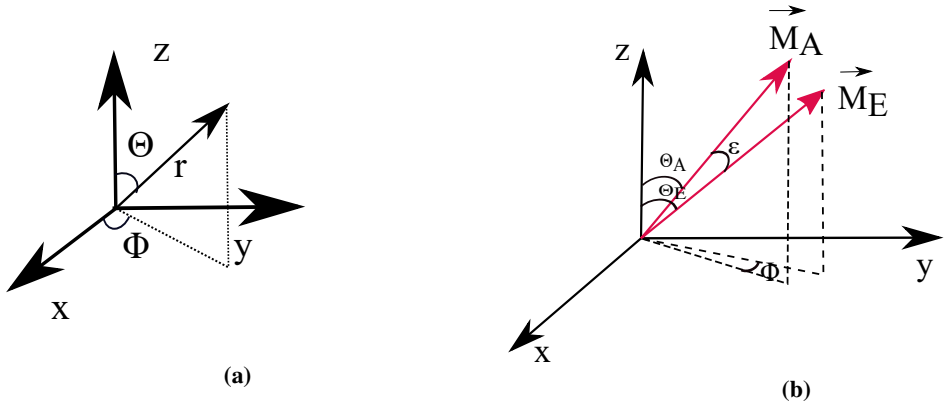

Fig. 3.1 Schematic of distribution function showing different angles. Fig(a) shows the reference coordinate system used in section 3.1. The polar and azimuthal angles are shown by θ and ϕ. Fig(b) shows $\vec{M}_A$ and $\vec{M}_E$ are absorption and emission moments. ε is the angle between absorption and emission transition moments. θ_A is the absorption moment angle with respect to polarization z-axis and θ_E is the emission absorption moment angle with respect to polarization z-axis used in section 3.2.

3.1 Derivation of average intensity

Consider a sample particle excited by polarized light. The molecules with absorption transition moment aligned in parallel to the electric vector of the polarized excitation have the highest probability of excitation which is called as photoselection. Absorption transition moment is the characteristic dipole moment of the molecule [38].

It is the process which occurs when the population of excited fluorophores align themselves in the direction of the polarized light [38].
Let us assume, that the luminescent molecules are placed in the origin of cartesian coordinates. The normalized intensity with a sufficient number of excitations and emissions when aligned along the z-axis in spherical coordinates is given by as a function of probability distribution function [38],

$$I_z = f(\theta) = \cos^2(\theta) \tag{3.1}$$

Here θ and ϕ are the polar and azimuthal angles of the spherical coordinate system, $f(\theta)$ is the probability distribution function of the randomly oriented population of excited molecules at an angle θ. For reference, the coordinate system is shown in Figure 3.1a. Accordingly, other intensity normalized components are given as,

$$I_y = \sin^2(\theta)\sin^2(\phi) \tag{3.2}$$

$$I_x = \sin^2(\theta)\cos^2(\phi) \tag{3.3}$$

The total intensity of the population of excited fluorophores or phosphorophores is equal to 1 as shown below.

$$I_0 = I_x + I_y + I_z = 1 \tag{3.4}$$

In the time domain, the intensity is expressed in terms of lifetime of particles,

$$I(t) = I_0 e^{\frac{-t}{\tau_f}} = (I_x + I_y + I_z)e^{-t/\tau_f} \tag{3.5}$$

τ_f is the luminescence lifetime.
The fraction of molecules ($W(\theta,\phi)d\theta d\phi$) oriented with the transition moments under defined angles in terms of probability distribution function ($f(\theta)$) was computed, as described by [76],

$$W(\theta,\phi)d\theta d\phi = \frac{f(\theta)\sin(\theta)d\theta d\phi}{\int_0^{2\pi} d\phi \int_0^{\pi} f(\theta)\sin(\theta)d\theta} \tag{3.6}$$

The whole of the denominator is the total number of molecules which is $\frac{4\pi}{3}$ [76]. The intensity signal along a direction when they are randomly oriented, is a function of the fraction of molecules and the probability distribution function. The average intensity along a particular direction is computed from Equation 3.6 and Equation 3.1, Equation 3.2 and Equation 3.3. For example, the average intensity along z-axis is,

$$I_z = <\cos^2(\theta)> = \int_{\phi=0}^{2\pi}\int_{\theta=0}^{2\pi}(\cos^2(\theta)W(\theta,\phi)d\theta d\phi)\cdot(I_0\cdot\exp(-t/\tau_f)) \tag{3.7}$$

Where I_0 total intensity and τ_f is the luminescence lifetime. For better understanding, $f(\theta)d\theta$ is the distribution function of fluorophores oriented between the angles θ and $\theta + d\theta$. The distribution of molecules when excited by vertically polarized light (z-direction) is given by $f(\theta)d\theta = \cos^2\theta \sin d\theta$ [38]. Further mathematical derivation is presented in Lakowicz [38].

3.2 Fundamental anisotropy of randomly oriented molecules

The distribution function $f(\theta)$ as described in the previous section can be used to determine the fundamental anisotropy r_0 of the particles. The term r_0 is used to refer to the anisotropy observed in the absence of other depolarizing processes such as rotational diffusion or energy transfer. The limits of the theoretical value for fundamental anisotropy is in between (-0.2 to 0.4). Diphenhydramine (DPH) showed a value of 0.39 [20]. The real anisotropy is generally much lower due to the angle between the absorption and emission dipole moments, environmental depolarization factors as discussed in subsection 2.1.3.
The basic principle behind this derivation of fundamental anisotropy begins with the classical formula for spherical trigonometry Santos and Valeur[76],

$$cos\theta_E = cos\theta_A cos\varepsilon + cos\phi sin\theta_A sin\varepsilon \tag{3.8}$$

The angle ε is the angle between absorption and emission transition moments. θ_A is the absorption moment angle with respect to z-axis, θ_E is the emission absorption moment angle with respect to z-axis, ϕ is the angle between the planes of absorption ($\vec{M}_A$) and emission moments ($\vec{M}_E$) in the x–y plane. This is shown in Fig. Figure 3.1a. Using this formula and employing equi-probable distribution of molecules, the fundamental anisotropy (r_0) is derived as shown in [76],

$$r_0(\varepsilon) = \frac{2}{5}\left(\frac{3cos^2\varepsilon - 1}{2}\right) \tag{3.9}$$

The above equation is taken as a reference to build an analytical model for deterministic rotations. Intensities from the polarization experiments is translated to estimate vorticity based on the deterministic rotations of the particles. The measurement of fundamental anisotropy is described in subsection 5.2.2.

3.3 Concept of deterministic rotations

The rate of rotation of the particles will change with respect to the Brownian motion in the case of deterministic rotations caused due to the vorticity. To estimate this rotation, a model was developed in-house based on the excitation polarization orientations. The model was based on two excitation polarization directions: vertically polarized laser and horizontally polarized laser. Accordingly, for each excitation polarization, the emission angles are vertical emission and horizontal emission. The notation of the emission intensities which are important for the rest of the thesis is given by,

- I_{zv} = Vertically polarized excitation and vertically polarized emission
- I_{zh} = Horizontally polarized excitation and vertically polarized emission
- I_{yv} = Vertically polarized excitation and horizontally polarized emission
- I_{yh} = Horizontally polarized excitation and horizontally polarized emission

The concept of deterministic rotation for the simplest case about x-direction is shown in Figure 3.2. To develop intuition, let the laser be vertically polarized along the z-axis and the fraction of molecules orient along z-axis due to photo-excitation as shown in Figure 3.2a. The observation is along x-axis showing the intensities I_z and I_y for horizontal and vertical emission. Here the notation described above is not followed,

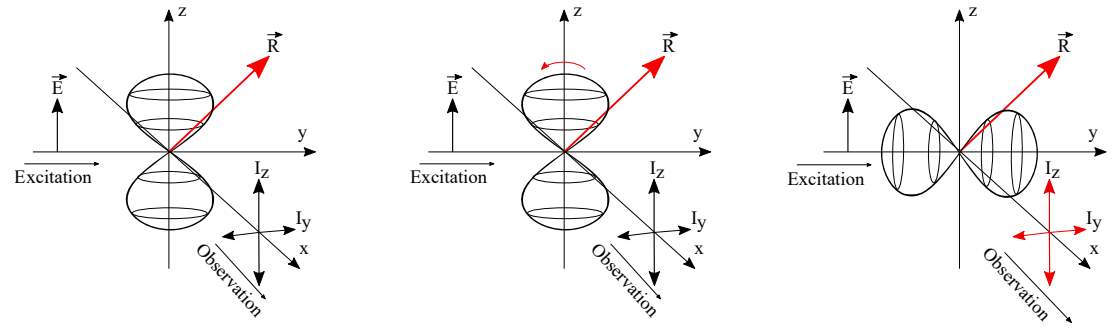

(a) **(b)** **(c)**

Fig. 3.2 The above images shows the orientation of the distribution function inside a particle excited by a vertically polarized light. Fig (a) shows the initial orientation of the molecules aligned in parallel to the polarization direction of the laser with intensities I_z and I_y in the direction of observation. Fig (b) shows the direction of rotation of the particles about x-axis (red arrow) which changes the orientation of the molecules. Fig (c) shows the modified emission intensities along the observation direction (highlighted in red). The change in emission intensities is utilized to estimate the vorticity. Here, I_z, I_y are I_{zv}, I_{yv} respectively from the notations mentioned in section 3.3.

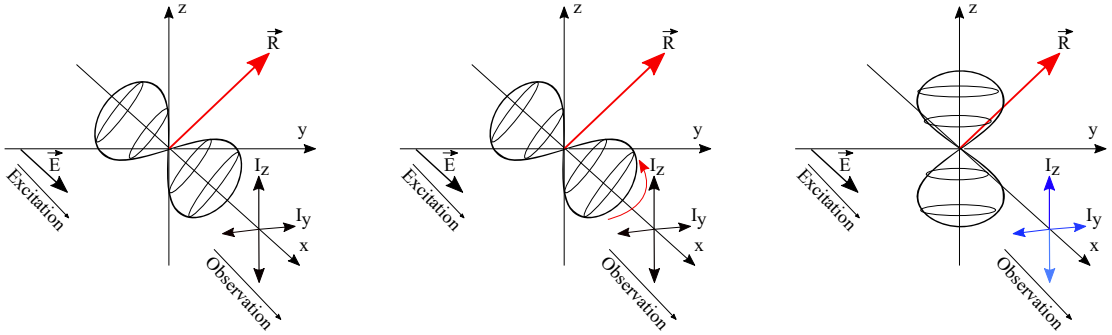

(a) **(b)** **(c)**

Fig. 3.3 The above images show the orientation of the distribution function of a spherical particle excited by horizontally polarized light. Fig (a) shows the initial orientation of the molecules aligned in parallel to the polarization direction of the laser with intensities I_z and I_y in the direction of observation. Fig (b) shows the direction of rotation of the particles about x-axis (red arrow) which changes the orientation of the molecules. Fig (c) shows the modified intensities along the observation direction (highlighted in blue). The change in emission intensities is utilized to estimate the vorticity. Here, I_z, I_y are I_{yh}, I_{zh} respectively from the notations mentioned in section 3.3.

to show the orientation of emission intensities to the polarization of the laser. The intensities in the image and the notation mentioned above is related as $I_z = I_{zv}$ and $I_y = I_{yv}$. Now, due to external forces acting on the particle (fluid medium forces), the particle will translate and rotate. If the particle translates, the polarized emission intensities will not change because the molecules remain oriented in the same direction as excitation polarization. If the particle rotates as shown in Figure 3.2b about x-axis the resulting orientation will be as shown in Figure 3.2c. Due to the rotation of the particles, the emission intensities have changed (marked in red), the original configuration which is marked in red. This difference in intensities is utilized to measure the rotation of the particle that leads to computing vorticity. Figure 3.3 shows the schematic for horizontally polarized light. Here the intensities marked in blue as shown in Figure 3.3c are $I_z = I_{zh}$ and $I_y = I_{yh}$.
Initial probability distribution function before rotation of the particle with the Brownian motion is given as

$$f_{\text{base}}(\theta) = \left((\cos(\varepsilon))^2 (\cos(\theta))^2 + 1/2\,(\sin(\varepsilon))^2 (\sin(\theta))^2\right) e^{-\frac{t}{\tau_c}} + \frac{1}{3} - \frac{1}{3} e^{-\frac{t}{\tau_c}} \tag{3.10}$$

Here, the distribution function depends on the emission angle ε, lifetime of the europium particle τ_c, Brownian motion correlation time τ_c and the angle θ which indicates the orientation of the molecules in spherical coordinate system. Since the probability distribution function and the fraction of excited fluorophores are in spherical coordinate system it is converted to Cartesian coordinate system. For reference the two coordinate systems are as shown in Figure 3.1b. Using the following relations,

$$x = r \cdot sin(\theta) \cdot cos(\phi) \tag{3.11}$$

$$y = r \cdot sin(\theta) \cdot sin(\phi) \tag{3.12}$$

$$z = r \cdot cos(\theta) \tag{3.13}$$

This vector (x,y,z) is initially expressed as an unit vector $\vec{v} = (sin(\theta)cos(\phi), sin(\theta)sin(\phi), cos(\theta))$. This unit vector is converted to Cartesian coordinate system. The rotation of the particle in spherical coordinate system is translated to Cartesian coordinate system using Rodrigues' rotation formula which is given below,

$$\vec{v}_{\text{rot}} = \vec{v}\cos\Omega t + (\vec{R} \times \vec{v})\sin\Omega t + \vec{R}\,(\vec{R} \cdot \vec{v})(1 - \cos\Omega t) \tag{3.14}$$

Here, the rotation unit vector $\vec{R}$ describes an axis of rotation about which vector $\vec{v}$ rotates by an angle $\theta = \Omega t$ according to the right hand rule. Ω is expressed as components of vorticity,

$$\vec{R} = \frac{1}{\Omega}\begin{bmatrix}\omega_x & \omega_y & \omega_z\end{bmatrix}^T \tag{3.15}$$

$$\Omega = \sqrt{\omega_x^2 + \omega_y^2 + \omega_z^2} \tag{3.16}$$

Lastly, this system is converted back to spherical coordinate system using inverse trigonometric functions from Equation 3.14 because the rotation of the particle is modelled in spherical coordinate system using,

$$\phi' = \tan^{-1}\frac{\vec{v}_{\text{rot},y}}{\vec{v}_{\text{rot},x}} \tag{3.17}$$

$$\theta' = \cos^{-1}\frac{\vec{v}_{\text{rot},z}}{\sqrt{\vec{v}_{\text{rot},x}^2 + \vec{v}_{\text{rot},y}^2 + \vec{v}_{\text{rot},z}^2}} \tag{3.18}$$

These modified angles ϕ' and θ' are used to modify the probability distribution function which accounts for the rotation of the particle. For example, the modified intensity equation along the z-axis when compared to Equation 3.7 is given as

$$I_{z,\mathrm{rot}}(t) = \frac{1}{W}\int_0^{2\pi}\int_0^{\pi} \cos^2\theta f_{\mathrm{rot}}(\theta',\phi')\sin\theta \mathrm{d}\theta\mathrm{d}\phi(I_0\cdot\exp(-t/\tau_{\mathrm{f}})) \tag{3.19}$$

Here, I_0 is the magnification factor used to reduce the rounding off errors in computation of the correlations in Appendix D. The modified distribution function is highlighted in red. The intensity equation is integrated to infinity for computing steady state time integrated signals. For example, along z axis the equation is

$$D_{\mathrm{zv}} = \int_{t=0}^{\infty} I_{z,\mathrm{rot}}(t)\mathrm{d}t \tag{3.20}$$

The subscript notation is the same as the intensity notation which was explained initially in section 3.3. For horizontally polarized excitation, the first step is rotating the coordinate system by 90^0. Then the above mathematical procedure is followed to derive the intensity components which is further integrated. All the synthetic signals which are time-integrated D_{zv}, D_{zh}, D_{yv} and D_{yh} are attached in the Appendix D. These signals are called as synthetic signals. These are dependent on the vorticity components, emission angle ε, lifetime of the europium particle τ_{f}, the Brownian motion correlation time τ_{c} and an arbitrary magnification factor I_0. These four signals are used simultaneously to estimate the vorticity by building an optimization problem as explained in the next section.

3.4 Optimization model to compute vorticity from experiments

Since all the four intensity images obtained from the measurements, I_{zv}, I_{zh}, I_{yv} and I_{yh} are used to compute the three components of vorticity, an unconstrained optimization model was developed in-house using Maple and Matlab. This model uses a minimization un-constrained function (fminunc) that involves pixel by pixel optimization in Matlab to compute the vorticity. However, this is still under development and currently not optimized for computing all the three vorticity components simultaneously.
Currently the optimization algorithm used is dependent on the ratios of $I_{\mathrm{zv}}/I_{\mathrm{zh}}$ and $I_{\mathrm{yv}}/I_{\mathrm{yh}}$ as shown in Equation 3.21. The accuracy of this model is tested in chapter 6 for computing the vorticity using actual measurements. The schematic diagram of the optimization algorithm is shown in Figure 3.4

$$\text{Optimization function} = \left(\frac{I_{\mathrm{zv}}}{I_{\mathrm{zh}}}\right)^2 + \left(\frac{I_{\mathrm{yv}}}{I_{\mathrm{yh}}}\right)^2 - \left(\frac{D_{\mathrm{zv}}}{D_{\mathrm{zh}}}\right)^2 - \left(\frac{D_{\mathrm{yv}}}{D_{\mathrm{yh}}}\right)^2 \tag{3.21}$$

The intensities I_{zv}, I_{zh}, I_{yv} and I_{yh} are the results from the experiments. The intensities D_{zv}, D_{zh}, D_{yv} and D_{yh} are the derived synthetic signals which depend on vorticity, that needs to be computed, as shown in Appendix D. The optimization function should tend to zero for accurate vorticity results. Currently, the optimization algorithm is optimized to an an extent for ω_y. The vorticity values obtained from this algorithm does not indicate the sign and the direction of vorticity.

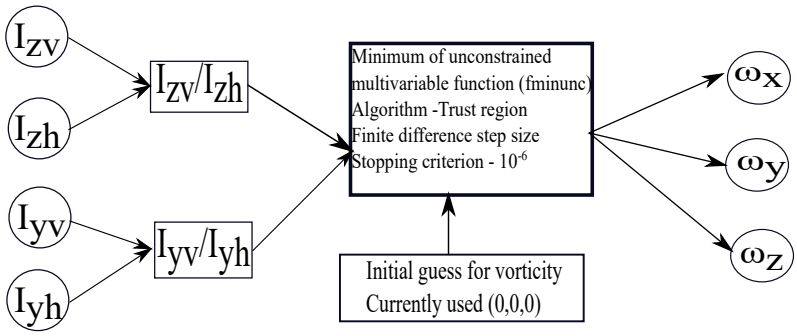

Fig. 3.4 The figure shows the schematic diagram of the optimization problem. The first four signals I_{zv}, I_{zh}, I_{yv} and I_{yh} are the results obtained from the experiments. Accordingly, their ratios are computed. Using the optimization algorithm applied to the Equation 3.21 with an initial guess as zero vorticity vector, the output vorticity components are computed using the in-built Trust region algorithm, in Matlab function fminunc.

3.4.1 Remarks

Over the course of this project, before arriving at this methodology of optimization problem, three completely different algorithms were devised and compared with the experimental results which failed to estimate vorticity. Unfortunately, the accuracy of vorticity depends highly on the type of optimization function created and the type of algorithm used. They are listed in Appendix H. Since this work is still under development, the current optimization model is not optimum that can be used for the highest accuracy of vorticity.

3.5 Formulation of the problem

When a new measurement technique is being developed for the first time, it is quite important to understand the scope of this technique and the assumptions which are made to reduce the degrees of freedom in developing or formulating the analytical idea behind the technique. This will give an idea of its limitations. The subsection 3.5.1 will help in understanding the forces and interactions involved in the problem with an illustration diagram. This helps in making some of the assumptions and deducing its limitations. The subsection 3.5.2 elaborates on the photo-bleaching as a natural decay process. The subsection 3.5.3 describes the most suitable non-dimensional numbers involved in this technique which helps in understanding the dominant physics involved. The subsection 3.5.4 describes the variation of anisotropy with viscosity as reviewed previously in subsection 2.1.3. The subsection 3.5.5 elaborates on the list of assumptions made by the author to interpret the results and reduce the number of factors involved in the formulation of this idea.

3.5.1 Interactions of the particles

When the nano-particles are dissolved in a fluid, they tend to show different characteristics of the flow depending on the type of fluid and chemical nature of the particles. In this case, let us consider that the fluorophore nano-particles are europium based chelates. Chelation is a type of bonding process which is involved with heavy metal atoms to stabilize the compounds in water [73]. Let us assume that nano-particles are dissolved in DI water. To formulate the problem, a schematic diagram is shown in Figure 3.5 which is modified from

[18]. The top image is the square duct flow with **L** as the laser beam which is used to excite the fluorophores. **W1** is the entry wall of the laser. The dashed lines create a rectangular space that is used as the Region of Interest (ROI) to study the influence of vorticity on the depolarization of the particles. The bottom image in Figure 3.5 shows the schematic illustration of the nano-particles in the boundary layer. In the ROI, the yellow circles are water molecules (**P2**), the red inner circles are fluorophores (europium nano-particles **P1**), the brown outer circles is made of PMMA but coated with fluorophores (**P3**). **I1** is the interaction between fluorophore nano-particle and wall, **I2** is fluorophore-fluorophore interaction and **I3** is the water molecule and fluorophore interaction. Forces which act on the particles are **F1** is laser scattering force due to electromagnetic field [57], **F2** is the external forces like drag force or shear forces in boundary layer which modifies the rate of the rotation of the particle **R**, **F3** is the external forces like gravity, Basset history force [47] and **F4** is the Brownian motion which acts on both water molecules and nano-particles. The arrowheads do not represent the direction of forces. In this thesis, to reduce the number of parameters which is being addressed, all the interactions (**I2 and I3**) are present in both quiescent state and inside the square duct flow. Considering the magnitude and the effect of interactions on the nanoparticles are the same in the core of the square duct flow and the quiescent state, the anisotropy of nano-particles should be in the same order. This is proved in the chapter 6 which supports the hypothesis that these interactions can be ignored. However, the interaction of the wall and the nano-particle in the boundary layer might affect the polarization of the particle depending on the type of collision and the resultant rate of rotation of these particles. This is assumed to be negligible and beyond the scope of this thesis. Based on the nano-particle diameter and the wavelength of the excitation source, three regimes are present that depend on the physics involved. They are ray optics regime ($D >> \lambda_0$), Lorentz Mie Regime ($D \sim \lambda_0$) and Rayleigh regime ($D << \lambda_0$) [11]. Depending on the type of regime, the forces exerted on the nano-particles by the laser vary. In this thesis, Lorentz Mie Regime is elaborated since the wavelength of the laser and the diameter of europium particles is around a similar wavelength. In the Lorentz Mie regime, the theory of electromagnetic field is applied to the nano-particles. **F1** is the force on the fluorophore due to the electromagnetic field of the laser. The optical forces caused by the excitation source on the particles can also affect the rotation of the particles. This is generally caused due to the radiation pressure [50]. These forces are exerted in the quiescent and in the flow state of the particles. The force due to the electromagnetic field was estimated as shown in the Appendix G. Due to the high powered laser, photo-bleaching of the nano-particles can occur which is elaborated in subsection 3.5.2.

F2 is the external forces like drag or lift force on the particles. The Reynolds and shear stresses which are prominent in the boundary layer [60], affect the particle rotation and translation. This will alter the polarization of the particles which can be measured using fluorescence anisotropy measurements. The estimation of the forces is beyond the scope of this thesis, however an attempt to estimate the vorticity due to modified rotation rate (**R**) is described in chapter 6.

F3 is other external forces like gravity, Basset history force [47] and thermal fluctuations on the particle. Thermal fluctuations are not considered in this thesis because they are considered independent with respect to the velocity of the fluid [11]. Basset history force is not modeled specifically in the vorticity correlations as described in section 3.3. **F4** is the force due to the Brownian motion which is acting on both the water molecules and the fluorophores. The Brownian motion correlation time which accounts for Brownian motion is considered while deriving the vorticity correlations.

The above analysis helps in identifying the possible sources of error which can be reduced experimentally or can be quantified numerically in the vorticity correlations.

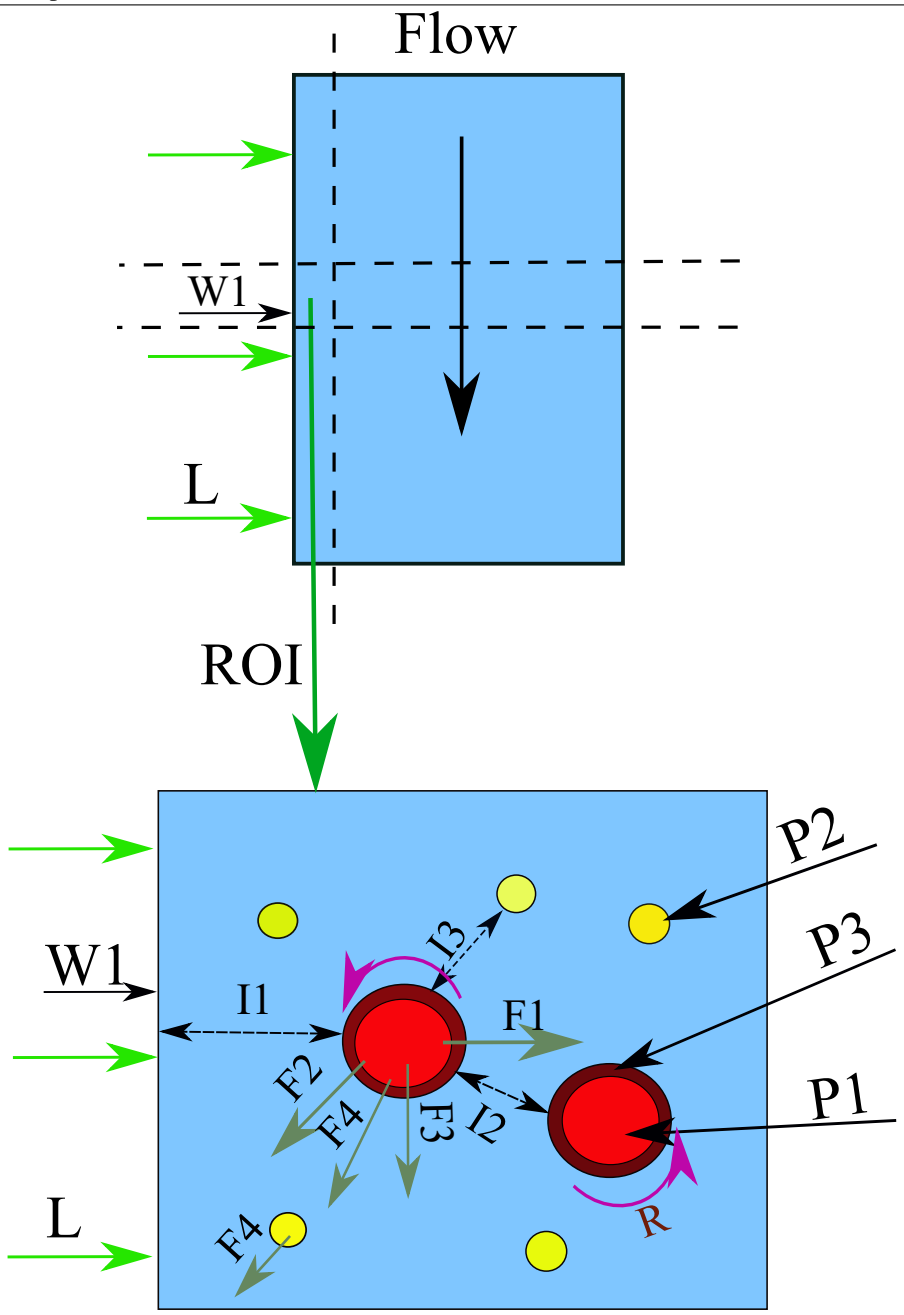

Fig. 3.5 The figure shows the schematic diagram of the problem which is being addressed. The top image shows the duct flow with laser source being excited from left (**L**), **W1** is the wall 1, the down arrow shows the flow direction in the duct and the dash lines create the Region of Interest (ROI) which is described more clearly in the bottom image. In the ROI, the yellow circles are water molecules (**P2**), the red inner circles are fluorophores (europium nano-particles **P1**), the brown outer circles is made of PMMA but coated with fluorophores (**P3**). **I1** is fluorophore nano-particle and wall interaction, **I2** is fluorophore-fluorophore interaction and **I3** is the water molecule and nano-particle interaction. Forces which act on the particles are **F1** is laser scattering force due to electromagnetic field [57], **F2** is the external forces like drag force or shear forces in boundary layer which changes the rotation rate of the particle **R**, **F3** is the external forces like gravity, Basset history force [47] and **F4** is the Brownian motion which acts on both water molecules and nano-particles. The arrowheads do not represent the direction of forces.

3.5.2 Photo-bleaching

Photo-bleaching of fluorophores and phosphorophores is a process that occurs when the sample under study is excited by a high powered laser making them unable to fluoresce due to cleaving their chemical structure [10]. Wüstner et al. [101] conducted Fluorescence loss in photo-bleaching (FLIP) to study the protein dynamics in cellular regions. They observed a trend in photo-bleaching which was expressed as a stretched exponential function

$$f_\gamma(t) = e^{(-t)^{-\gamma}} \tag{3.22}$$

The stretched exponential function is the generic decay function with γ as a constant. Since the stretched exponential function is a universal decay process, a similar analysis is performed on the hybrid europium based particles as shown in subsection 5.1.3.

3.5.3 Non-dimensional numbers

Non-dimensional numbers help in comparing the forces which are acting on the particle to understand the underlying physics involved. Many non-dimensional numbers play an important role in prioritizing the important forces acting on the particles. The bulk Reynolds number ($\mathrm{Re_b}$) of the flow is based on the square duct velocity (U), the density of the fluid (ρ_f), the dynamic viscosity of the fluid (η), kinematic viscosity of the fluid (ν) and square duct width (L_c). It is the ratio of the inertial forces to the frictional forces in the medium,

$$\mathrm{Re_b} = \frac{\rho_\mathrm{f} U L_\mathrm{c}}{\eta} \tag{3.23}$$

The above Re is chosen considering the available DNS database. Accordingly, the experimental setup was built to achieve similar Re. The density ratio between the particles and the fluid medium is given as,

$$\text{Density ratio} = \frac{\rho_\mathrm{p}}{\rho_\mathrm{f}} \tag{3.24}$$

The density ratio close to 1 ensures the diffusion of nano-particles in the fluid medium effectively. Bian et al. [11] reviewed all the available Brownian motion theories based on the properties of the flow. They showed that for the Langevin model of Brownian motion to be applicable, $9\rho_\mathrm{f}/2\rho_\mathrm{p} << 1$ to ignore the inertia completely. However in this case,

$$\frac{9\rho_\mathrm{f}}{2\rho_\mathrm{p}} \approx 3.5 \tag{3.25}$$

The above equation shows that the inertia of fluid is important. In the optimization problem (section 3.4) and the analytical equations (Appendix D), the Brownian motion time scale was considered.

To justify a proof of concept of an experimental technique, the physics behind the problem, the characteristics of an experimental setup and the analytical model behind the underlying physics should fit together like a jigsaw puzzle. The hypothesis behind the physics involved is proposed based on scaling, using two additional non-dimensional numbers to relate the time-scales of the fluorescence lifetime of the particles to the vorticity in the flow medium. To capture the information from the rotation of the particles during its emission, the lifetime of the particles (τ_f) should be of the same range as the intended parameter which is being measured, in this case being inverse of vorticity (ω). Hence, the non-dimensional number is given by **ND1**.

$$\mathrm{ND1} = \frac{\tau_\mathrm{f}}{\frac{1}{\omega}} \tag{3.26}$$

The number ND1 gives a rough idea about the sensitivity of this measurement technique. High vorticity means, the timescale of vorticity is low. Low vorticity means, the timescale of vorticity is very high. For very low vorticity say of order $\omega = 100\ s^{-1}$ the vorticity time scale is around 10 milliseconds. This means to capture the vorticity of this order, you need lifetimes of vorticity timescale order. For particles with lifetimes smaller than the vorticity timescales, the model does not show any sensitivity in the derived signals section 3.3. Hence, as the particle lifetime increases and approaches the vorticity timescale, the variation in derived signals can be observed which could be used to estimate vorticity. Also the minimum magnitude of vorticity which can be sensed, should be higher than the model predicted vorticity, due to the measurement error.

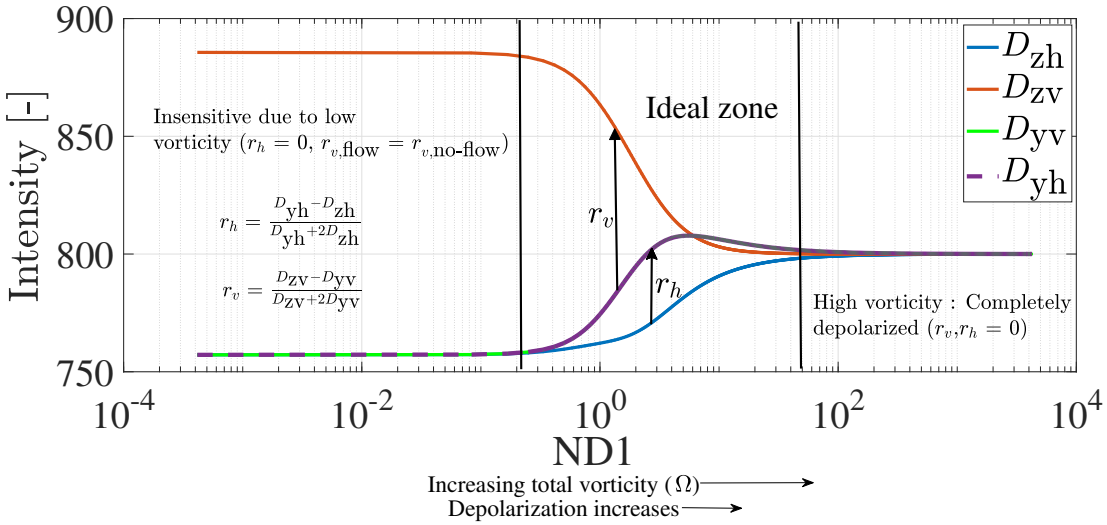

(a)

Fig. 3.6 The figure shows the variation of ND1 (subsection 3.5.3) from the model. This is computed using fixed lifetime ($\tau_f = 240$ s). For very low ND1, the magnitude of the vorticity is very low to be captured by the model. As vorticity increases, depolarization of the particles increase which leads to converging of all four intensities. Hence, the characteristic polarization sets the upper limit of ND1. Ideal zone is the region of ND1 from the analytical model where the hypothesis of this physics can be tested. This zone shrinks depending on the measurement error.

This is the reason why phosphorescent particles are chosen which show longer lifetimes to estimate smaller vorticity values. However, higher phosphorescence lifetimes will give more room to deactivation processes that reduces the quantum yield. Considering the conditions of the experiments conducted, a balance between the phosphorescence quantum yield and the phosphorescence lifetimes was critical for selecting the type of particles. As ND1 increases to a very high value (above 100), the particles are completely depolarized which makes them unsuitable to estimate that high vorticity. Hence, the upper limit of ND1 is constrained by the characteristic polarization of the nanoparticles and the lower limit of ND1 is constrained by the magnitude of vorticity and the measurement error. Figure 3.6 shows the variation of all the four intensity signals derived in section 3.3. Ideally, ND1 of order 1 should be sufficient to capture the vorticity using this hypothesis.
The region of interest, in this case is a spherical particle. For a spherical particle, it is assumed that the molecules

are fixed rigidly inside the polymer matrix. The additional non-dimensional number ND2 is based on τ_c is,

$$\mathrm{ND2} = \frac{\tau_\mathrm{f}}{\tau_\mathrm{c}} \tag{3.27}$$

When the Brownian motion correlation time (τ_c) is very low compared to the lifetime (τ_f), the anisotropy of europium nanoparticles in quiescent flow state (r) reduces, making it impractical to measure depolarization (Equation 3.28) caused due to the vorticity using the model section 3.3. When the Brownian motion correlation time (τ_c) is very high compared to the lifetime (τ_f), the drop in anisotropy due to vorticity reduces, depending on the magnitude of the Re. An overall idea of the variation of ND2 for different Re is shown in Figure 6.5. Hence, the non-dimensional number ND2 should be of the order 1. To clearly understand the role of the newly introduced non-dimensional numbers, the above theory is described schematically in Figure 3.7.

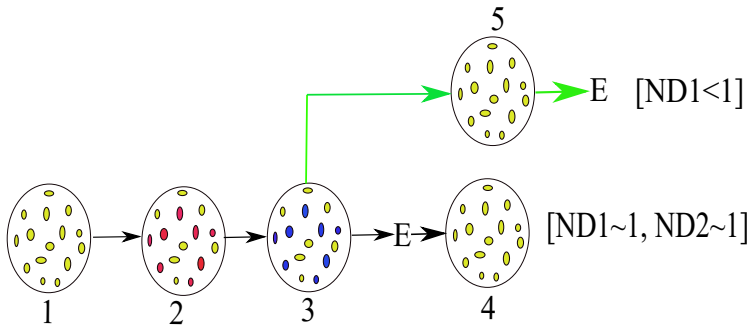

Fig. 3.7 The figure shows the schematic diagram of the problem describing the processes which might happen based on the non-dimensional numbers (ND1, ND2). E stands for emission. The big circle is a particle and the molecules are in yellow colour ellipses (ground state) is the initial ground state of the particle inside the duct flow in the boundary layer (State - 1). State 2 is attained when the particle is excited with vertically polarized laser and few molecules whose axis is parallel to excitation polarization get excited as shown in red color. Two test cases can be discussed from state 2. Test case 1 [ND1<1] : There is no effect of vorticity on the particle and the particle emits the photon without any response due to low vorticity timescale compared to the lifetime of the particle. Test case 2 [ND1∼1, ND2∼1]: The particle rotates due to the vorticity which will change the energy levels and the orientation of the particle with respect to the observation axis. The molecules in the new state 3 are shown in blue color. Followed by this, the photons are emitted in the altered state. Lastly, the molecules reach ground state as shown in state 4.

All the relevant timescales and non-dimensionless numbers in this thesis are listed in Table 3.1.

3.5.4 Effect of viscosity on anisotropy

The viscosity is one of the important characteristics of the fluid that plays an important role in the variation of anisotropy. As described in subsection 2.1.3, Levitt et al. [43] showed the variation of anisotropy with viscosity of molecular rotors. For the spherical particles, the variation of viscosity with anisotropy is given by the Perrin equation [40],

$$\frac{1}{r} = \frac{1}{r_0}\left(1 + \frac{\tau_\mathrm{f}}{\tau_\mathrm{c}}\right) \tag{3.28}$$

The derivation of this equation can be referred from Lakowicz [40]. The Perrin equation (Equation 3.28) relates the fundamental anisotropy with the measured anisotropy of the spherical nano-particle in the respective fluid

Table 3.1 List of all the relevant non-dimensionless numbers and timescales.

Quantity	Value
ρ_f of water	1000 kg $\cdot$ m^{-3}
ρ_p of europium nanoparticles	1180 kg $\cdot$ m^{-3}
Re	1000-17000
η	0.00089 Pa $\cdot$ s
T	300 K
τ_f	240 μs (subsection 5.1.1)
τ_c	194 μs (subsection 2.1.2)
Re_τ	50-500
Density ratio	1.18
ND2	1.230

medium. It is dependent on the luminescence lifetime (τ_f) and the correlation time (τ_c). The fundamental anisotropy is given by the Equation 3.9. The effect of viscosity on the anisotropy of europium nanoparticles was studied in subsection 5.2.3.

3.5.5 Assumptions

In this thesis, many assumptions were made to simplify the problem statement and capture the physics of the problem. They are:

1. The population of the fluorophores rotate after their excitation. It is assumed that the angle of rotation is the same for each molecule by ensuring the observation area as a particle comprising of many molecules inside.
2. Homogeneous concentration of fluorophore molecules inside the spherical particle.
3. Fluorophore molecules are coated uniformly on the PMMA shell of the particles which behaves similar to the core of the particle-filled with fluorophores.
4. The concept of deterministic rotations (section 3.3) is developed for only spherical particles.
5. The dye molecules inside the polymer matrix of a particle are fixed.
6. The pump in the flow loop does not harm the shape and destroy the chemical structure of the particles which will lead to incorrect results.
7. The interaction between PMMA shell and the fluorophore molecules is ignored.
8. There is no shear deformation of the nano-particles due to shear forces in the boundary layer.
9. The effect of the concentration of nano-particles on the turbulence characteristics of duct flow was not accounted for.
10. When ND2 is a very high value, ideally the rotation of the nanoparticles should be captured because of higher lifetime. However, in the correlations (section 3.3), this effect will not be accounted because the time integrated signals are integrated from t = 0 to ∞.

Chapter 4

Experimental setup

In this chapter, a description of the experimental setup used to measure the depolarization of the experiments is presented. Initially a relatively simple experimental setup was constructed to capture phosphorescence quantum yield from the common fluorophore particles (In this thesis:- eosin Y and rhodamine) as described in section F.2. However, capturing the phosphorescent quantum yield from these fluorophores consistently at room temperature is quite difficult. To fix this issue, a new dedicated experimental setup that was used to capture phosphorescence quantum yield from lanthanide-based nanoparticles (In this thesis:- europium) is elucidated in section 4.1. The section 4.2 elaborates a simple description of spectrometer setup to understand the emission spectrum of the nanoparticles. In section 4.3, the design of the square duct depending on the experimental constraints and the available DNS data is elaborated. Since this is the first attempt to estimate depolarization in the square duct using a dedicated algorithm, a specific procedure to conduct the experiments was developed as presented in section B.5. Lastly, the post-processing involved in this experimental setup, is elucidated in section 4.4.

4.1 Phosphorescence anisotropy setup

This setup was constructed to capture the phosphorescence quantum yield from europium based chelated PMMA nanoparticles. The excitation wavelength of the laser is in UV wavelength range of 355 nm and the emission spectrum wavelength is in the wavelength range of 600 nm. Further analysis is shown in subsection 5.1.2.
The experimental setup is shown in Figure 4.1. Figure 4.1a shows the schematic diagram of the experimental setup. Figure 4.1b shows the actual experimental setup inside the darkroom. The numbers in the figures indicate the part numbers which are listed in Table 4.1. All the part number descriptions are provided in the Appendix B, Table B.2.
Figure 4.2a shows the darkroom arrangement of the above setup. The green device is the Continuum Surelite laser with two laser heads holding a third harmonic generator which is used to emit the laser beam at 355 nm. Figure 4.2b is the flow-meter which was used in the flow line to measure the flow rate. Figure 4.2c was the power meter used to calibrate the polarization direction in the emission side and to fix the angle of the polarizer in the excitation side.

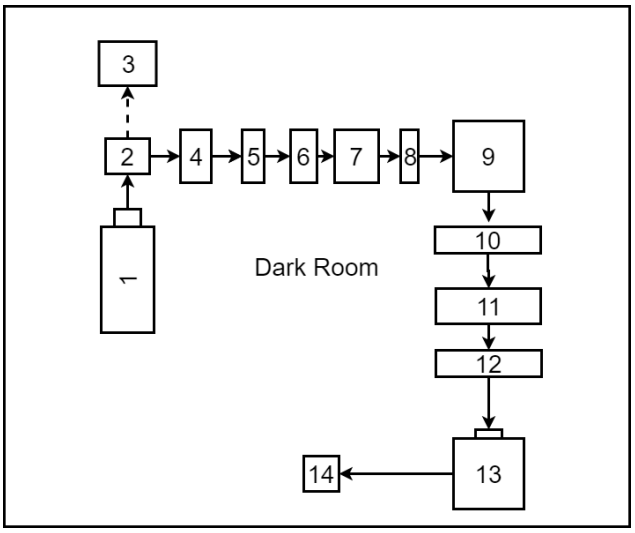

(a) Schematic of experimental setup

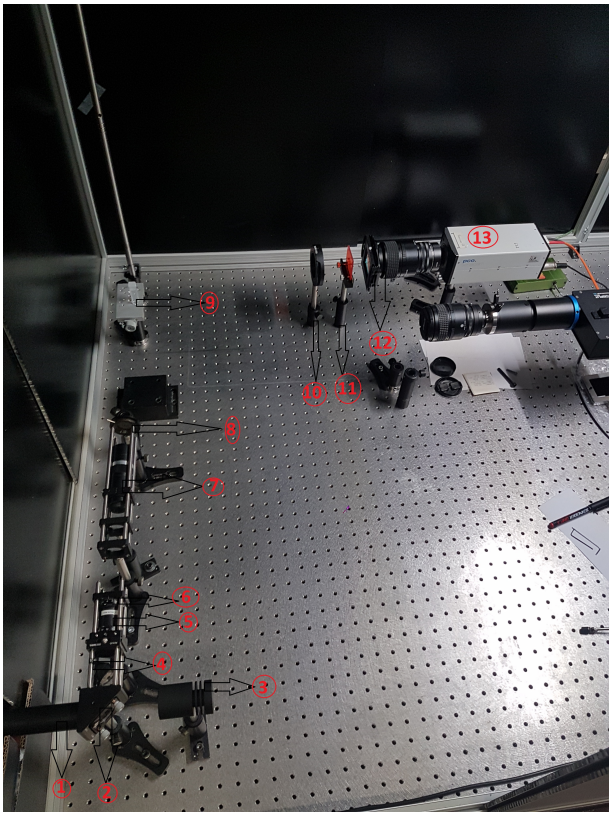

(b) Actual experimental setup enclosed in the darkroom

Fig. 4.1 Schematic diagram of the experimental setup is shown in Fig. (a) and the actual experimental setup is shown in Fig. (b). The numbering in the schematic diagram and the experimental setup image denotes the parts as described in the Table Table 4.1.

Table 4.1 List of components as shown in the Figure 4.1. This setup was built to capture phosphorescence from europium based chelated nano-particles.

Experimental equipment number (Figure 4.1)	Description of the part
1	Laser 355 nm Nd:YAG (4.5 W, Pulsed, 10 Hz, Q-switch = 187 μs, 2 laser heads)
2	Harmonic beam splitter
3	Beam dump
4	Beam sampler
5	Alpha-BBO Glan laser polarizer (accuracy - 2°)
6	Half wave-plate (accuracy - 2°)
7	Light sheet optics (laser sheet thickness $\approx$ 0.5 mm)
8	Iris diaphragm
9	Test sample (optical glass fluorescence cuvette or vertical glass square duct)
10	Linear polarizer (accuracy - 2°)
11	Long pass filer 570 nm
12	Short pass filter (Edge filter - 643 nm)
13	Camera - Sensicam QE 12 bit CCD cooled and the objective of the camera is AF MICRO NIKKON 105 mm 1:2.8 D
14	Computer system
Seeding particles	Europium based chelated particles (diameter = 120 nm)
Pump capacity	(0-3840) mL $\cdot$ min^{-1}
Exposure	15 s
Observation distance	10 cm
Pixel size	10.5 μm
Seeding concentration	0.05 mg $\cdot$ mL^{-1}

4.2 Spectrometer setup

A spectrometer was used in this thesis to interpret the luminescence spectrum nanoparticles. Figure 4.3a and Figure 4.3b shows the spectrometer and the schematic of the experimental setup. The function of the spectrometer is to capture the light and break it into spectral components. These spectral components were further digitized as a function of wavelength and this signal is displayed on the computer.
In Figure 4.3a the black connector cable is the optical fiber which allows the light to enter. The green device is the GREEN Wave Low Cost Spectrometer (StellarNet). All the parts are listed in Table 4.2. All the experiments that were conducted in the dark room are described in subsection 5.1.2.

Table 4.2 List of components as shown in the Figure 4.3.

Experimental equipment number (Figure 4.3)	Description of the part
1	Excitation source - Laser
2	Test sample in a cuvette
3	GREEN Wave Low Cost Spectrometer (wavelength range : 350 nm - 1150 nm, signal to noise ratio : 400:1)
4	Computer

(a)

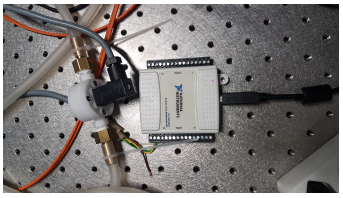

(b)

(c)

Fig. 4.2 Fig (a) shows the darkroom where experiments were conducted. Fig (b) shows the flow-meter and Data Acquisition system (DAQ) used to measure the flow-rate in the loop. Fig (c) shows the power meters used to fix the polarization angle of the laser.

(a)

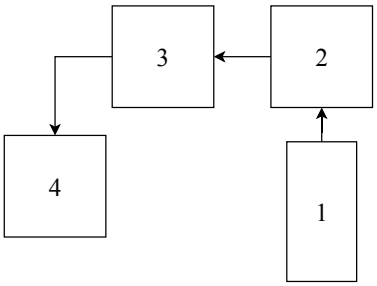

(b)

Fig. 4.3 Green wave spectrometer with the optical fibre in black color as shown in Fig. (a) and its schematic diagram as shown in Fig. (b). The numbering in the schematic diagram and the experimental setup image denotes the parts as described in the Table 4.2.

4.3 Square duct design

The nanoparticles were initially studied in a glass cuvette as shown in Figure 4.4a. To study the effect of vorticity a square duct was designed considering the necessary development length required for turbulence and its limitations from the pump and the DNS data. Monty[52] studied in detail the effect of the duct length on the developed flow conditions. They show that the required development length for the turbulence characteristics to develop was $L = 75 \times H$. Hence to be on the safer side the chosen development length for the square duct was $L = 150 \times H$. Based on the previous literature [54–56], that show macroscale turbulence characteristics in microscales, square duct with millimeter dimensions was expected to show macroscale turbulent flow

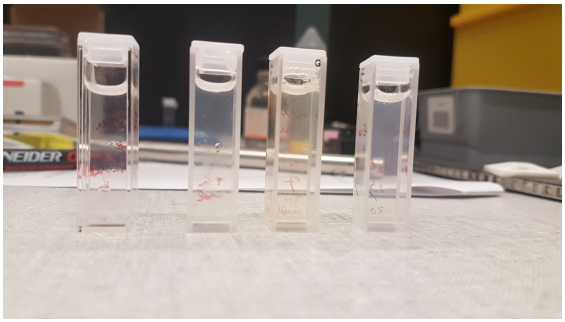

(a)

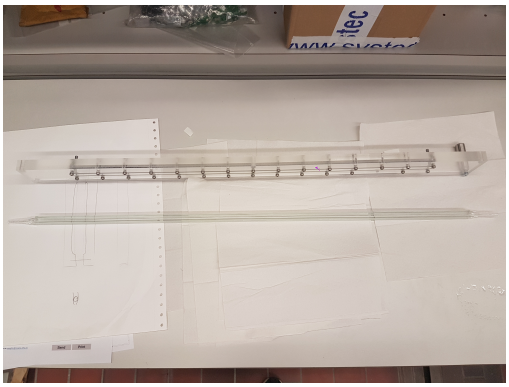

(b)

Fig. 4.4 Transparent 3 mL optical glass fluorescence cuvettes are shown in Fig. (a), two square ducts manufactured in plastic and glass as shown in Fig. (b).

characteristics.

Two square ducts were designed one made of plastic and the other one made of glass as shown in Figure 4.4b. However, since the cross-section of the duct is in the order of millimeter, it should be ensured that the surface roughness does not affect the boundary layer. Previous researchers have studied the effect of surface roughness in turbulent duct flows [46, 5]. Maeda et al. [46] showed that for the duct to be hydraulically smooth, the following condition needs to be satisfied.

$$\frac{k_S u_\tau}{\nu} < 1 \tag{4.1}$$

Here u_τ is the frictional velocity, k_s is the surface roughness. Surface roughness in the plastic square duct was measured to be $k_s = 2 \times 10^{-6}$ m. The glass square duct was expected to show even lower surface roughness since it was made of optical glass. In this thesis based on the Reynolds numbers as shown in subsection 3.5.3, the condition is $\frac{k_S u_\tau}{\nu} < 0.75$. Hence the duct flows are considered smooth without any effect of surface roughness on the boundary layer.

Considering the above criteria and the constraints of the pump availability, the manufactured square duct dimensions are 4 mm x 4 mm x 600 mm ($H = 4$ mm, $L = 600$ mm, hydraulic diameter $d_h = 4$ mm). All the part drawings are shown in the Appendix A. All the measurements were conducted at the length of $L = 135 \times H$. All the measurements were conducted in the glass square duct to lower the fluctuations due to the aberrations on the surface of the square duct.

4.4 Post processing

Most cameras have a tailor-made software which displays the image. Figure 4.5a shows the image of the vertical duct shown in the Cam-ware software developed for the used camera. In this image, the numbers indicate the walls of the glass duct. Wall 1 and wall 4 are the outer walls. Wall 2 and wall 3 are the inner walls of the duct. The white coating towards the inner edge of the duct is the glue used to hold the duct. Unfortunately, they scatter the light in the background. The glue was avoided by finding a sweet spot where the visibility of the glue was less than 5 pixels columns of the camera. The width of the duct in the camera is 350-pixel columns. The white spots in the image are the dead pixels on the sensor. The hot/dead pixel list is created from

the Sensicam camera and this list is imported to the Python script to equate them to NaN. Around 800 pixels were listed to be defunct pixels.

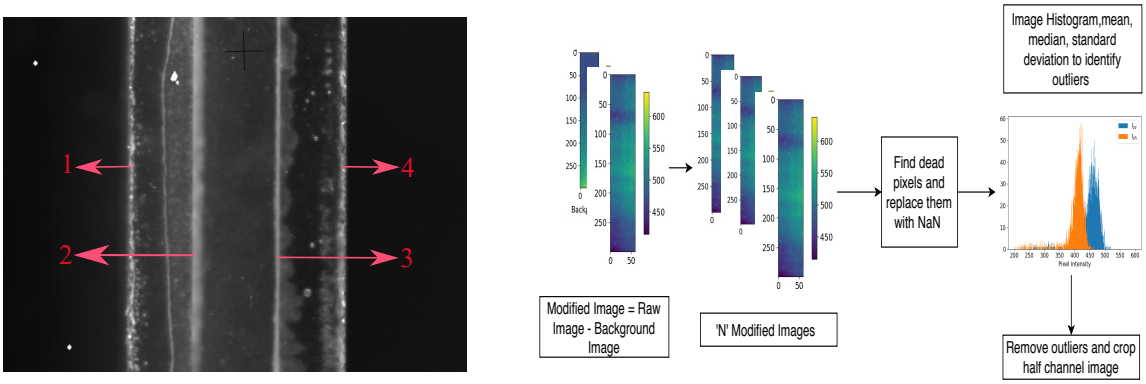

(a) **(b)**

Fig. 4.5 Fig. (a) shows the background and 4 walls of the vertically oriented duct from the camera used in the experimental setup (section 4.1). Wall 1 and wall 4 are the outer walls. Wall 2 and wall 3 are the inner walls of the duct. Fig. (b) shows the simple image processing algorithm to remove the outliers. The duct is oriented in vertical direction and the laser sheet was excited along the flow direction.

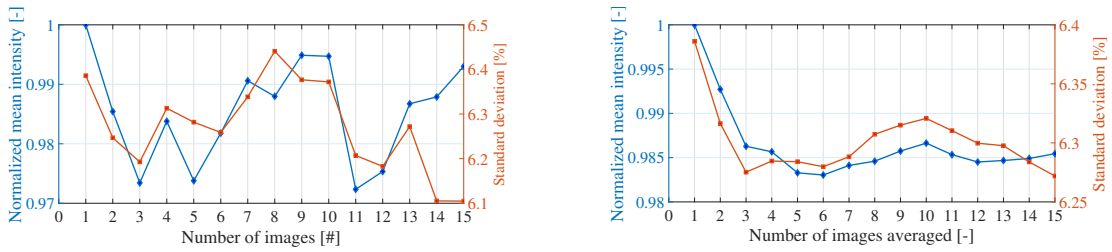

(a) **(b)**

Fig. 4.6 For Re = 4400, 15 images were captured. Fig. (a) shows the mean and standard deviation of each image. Fig. (b) shows the mean and standard deviation after averaging 'N' number of images.

All the images which were obtained from the above procedure need to be post-processed to remove dead pixels on the camera sensor and the outliers from the measurements. Figure 4.5b shows a simple post-processing algorithm that was developed in Python. 'N' number of images is captured in the camera as the background image and 'N' images are captured with laser ON. This set is subtracted and the dead pixels are equated to NaN. Using the image histogram, the mean and standard deviation of the images as a reference all the outliers were removed.

Figure 4.6a shows the mean and the standard deviation in the images along the y-axis and the # number of the image in the x-axis. Figure 4.6b shows the mean and standard deviation along the two y-axis and the x-axis indicates the number of images averaged to get the mean and standard deviation. The graphs show very little deviation in the mean of the images and the standard deviation of the images. But sometimes the images can detect a speck of dirt and to be on the safer side, 3 images per experiment were captured and averaged to remove any discontinuities. This is because the laser frequency was 10 Hz. In 0.1 seconds, two pulses of the laser were

shot at the sample. Subsequently, for the exposure of 15 seconds, 300 laser pulses were shot at the sample. As a consequence, the power output of 5 or 10 laser pulses will not significantly affect the intensity of the images. However, it is important that the procedure developed in section B.5 is followed.
The general anisotropy equation as described by Equation 1.2, should be modified to subtract the background image. The background image is subtracted to remove the background light from the surroundings and the camera noise. The modified anisotropy equation is [6],

$$r = \frac{(I_{\parallel} - I_{\mathrm{b}}) - G(I_{\perp} - I_{\mathrm{b}})}{I_{\parallel} - I_{\mathrm{b}} + 2G(I_{\perp} - I_{\mathrm{b}})} \tag{4.2}$$

Here $I_{\parallel}$ is I_{zv}, $I_{\perp}$ is I_{zh} for vertically polarized laser. G is an experimental factor that is used to fix the reference excitation polarization of the laser and I_{b} is the intensity of the background with laser off. The G factor is expressed as

$$G = \frac{I_{\mathrm{yv}}}{I_{\mathrm{yh}}} \tag{4.3}$$

G is ensured to be close to 1 for all the experiments conducted to find variation of anisotropy with viscosity. However, for the actual value of G, background intensity and the scattering from impurities in the medium has to be subtracted. DI water was used to minimize the dirt/impurities in the liquid. Using the Equation 4.2, post-processing of all the experiments were conducted in chapter 5 and chapter 6.

4.4.1 Intensity variation in the laser sheet

To understand the scope of this technique, it is important to know its limitations. One of the main limitations of this thesis is the variation of laser sheet intensity along the height of the laser sheet. Figure 4.7 shows the image of the half width of the square duct illuminated by a full laser sheet. The half-width of the square duct is 2 mm. So accordingly, the height of the laser sheet was measured to be around 18 mm with the pixel size of 10.5 μm. The respective normalized intensity was plotted with the laser sheet as shown in Figure 4.7b. This was fitted with a 2-D Gaussian distribution function.
It can be observed that the variation of laser sheet intensity is prominent in the contour image Figure 4.7a. To reduce this effect, a section of the cropped image in the upper half and the cropped region is shown by a black dash-dot rectangle in Figure 4.7a. This means that all the results from the experiments will have a considerable noise. To tackle this variation of laser power, most of the interpretation of results were performed with column-averaged images. This allows for observing the trends near the edges of the square duct along with averaging the noise levels. This limits the pixel to pixel estimation of vorticity in this thesis. Once the column averages were performed, the noise level is averaged. If we consider a uniform concentration of the particles in the fluid and ensure similar experimental conditions, the systematic error in Re = 0 and Re = 4434 should be the same. To remove systematic error, the following image processing algorithm is followed as shown in Figure 4.8. The subtracted signal can also be computed by subtracting non-normalized signals and further normalizing them. However, random error will still remain.

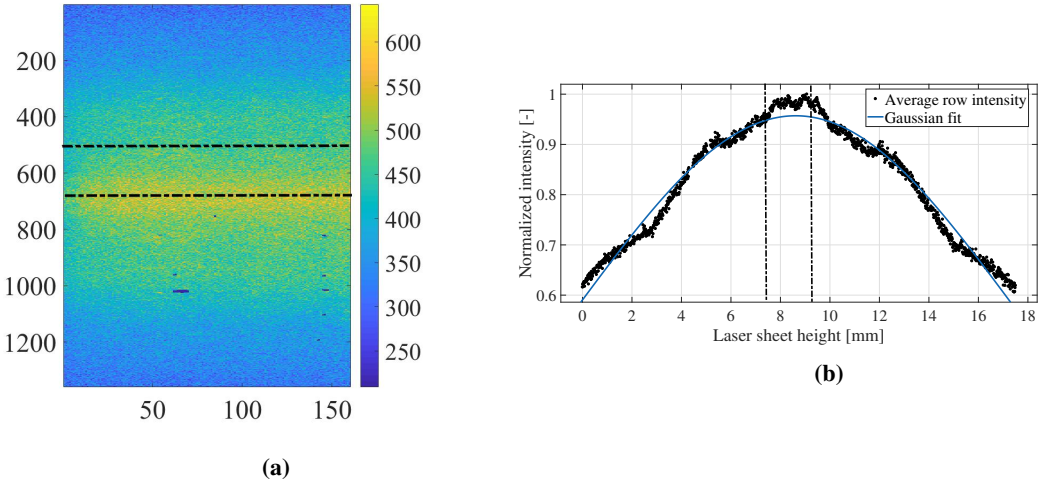

Fig. 4.7 The above image shows the emission intensity of the europium nanoparticles. Assuming uniform concentration of the nanoparticles in quiescent flow, this shows the variation of intensity along the height of the laser beam. The variation of normalized intensity along the laser sheet height is shown in Fig(b).

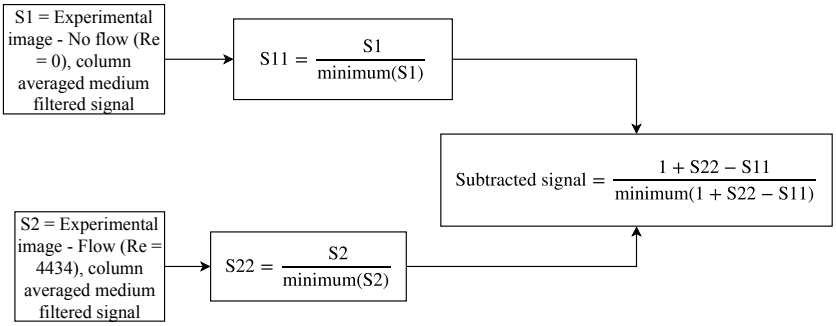

Fig. 4.8 The above image processing procedure is followed to remove the inaccuracies which are common in both the flow and no-flow condition. Firstly the respective signals are column averaged and median filtered. Further, they are normalized with respect to their minimum values and lastly the subtracted signal is obtained as shown in the box. This is used in section 6.4 for observing trends in the variation of intensities.

Chapter 5

Preliminary studies

To develop a new measurement technique, it is important to select the most suitable equipment. In the experimental setup, the nanoparticles which display luminescence properties need to be analyzed. In this chapter, a set of preliminary studies is conducted on the nanoparticles. Preliminary analysis of the particles like lifetime analysis, spectroscopic analysis is described in section 5.1. Fluorescent anisotropy measurements were conducted in a quiescent fluid state to study the anisotropy in no-flow conditions. They are elaborated in section 5.2. It is also shown that the europium nanoparticles can be used as viscosity probes to estimate viscosity based on quantum yield and anisotropy.

5.1 Preliminary analysis of the particles

In subsection 5.1.1 shows the lifetimes of hybrid europium based chelates. The subsection 5.1.2 shows the emission spectrum of colloidal silica and europium nanoparticles that are tested in this thesis to select the filters at the emission side. The subsection 5.1.3 conducts the photobleaching tests which are important to understand the shell-life of the particles and to understand its limitations.

5.1.1 Lifetime analysis

Lifetime analysis of the nanoparticles is very important to observe the type of luminescence emission spectra. This process allows us to assign specific bands for processes like fluorescence, delayed fluorescence, and phosphorescence. Generally, the lifetime in the order of micro-seconds or higher is phosphorescence. While fluorescence timescale is generally in nanoseconds or picoseconds. Often, fluorescence and phosphorescence bands overlap which makes it difficult to differentiate the two processes. The timescale of fluorescence lifetime is not suitable to measure vorticity due to very low ND1 as introduced in Equation 3.26. Hence this project aimed to capture the phosphorescence from eosin Y and rhodamine. Many experiments were conducted with eosin Y using the experimental setup shown in Appendix F. But the phosphorescence quantum yield was too low to be captured from these two compounds.

To capture the phosphorescence quantum yield, europium based chelated nanoparticles were used. The intensity decay profile from the experiments is shown in the Figure 5.1. This can be described mathematically as,

$$I(t) = I_0 e^{(-bt)} = I_0 e^{\left(\frac{-t}{\tau_f}\right)} \tag{5.1}$$

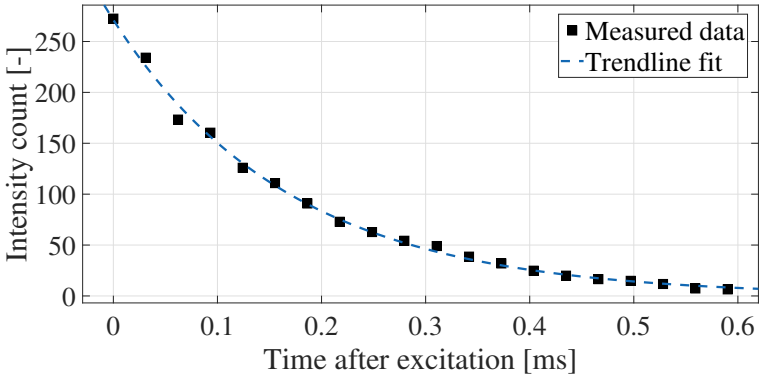

Fig. 5.1 Intensity decay of europium based nano-particles with respect to time. A mono-exponential decay trend-line was fit to determine the lifetime of the particles as shown in Equation 5.2.

From MATLAB, the bounds for the constants are I_0 - (271.2, 285.4) and b - (4.557,5.541). The trend-line equation for Figure 2.1 using the average coefficient b is given by,

$$I(t) = 279.1e^{-5.001t} \tag{5.2}$$

The lifetime is given by $\tau_f = \frac{1}{5.001}$ms $\approx 199.966\ \mu$s. Three repetitions were conducted to measure the lifetime and the average lifetime from these trials was found to around $\tau_f = 240\ \mu$s. A mono-exponential decay also implies that there is only one excited state of the nano-particles. It is very important because the concept developed in section 3.3 was developed for a single excited state. This was used in the analytical model correlations in section 3.3 to employ them in chapter 6.

5.1.2 Spectroscopic analysis

When a new experimental technique is being developed from scratch, it is important to study the luminescence spectra of the selected nanoparticles. Spectroscopy analysis of eosin Y is shown in Appendix F. Figure 5.2a shows the spectrum of colloidal silica when excited by a laser of wavelength 532 nm. The integration time used for this was 0.5 seconds. Figure 5.2b and Figure 5.2c shows the spectrum of colloidal silica and the europium based particles when they were excited by 355 nm laser with an integration time of 6 seconds.
Before analyzing the spectra of europium based nanoparticles, the spectra of colloidal silica has to be interpreted. When you compare the emission spectrum of colloidal silica from Figure 5.2a and Figure 5.2b, it is observed that the scattering properties are not prominent in colloidal silica when it is excited in the UV wavelength 355 nm (no clear peak and higher noise levels). This is probably because the colloidal silica is expected to show a combination of fluorescence and scattering [104]. However, due to no suitable completely scattering solutions in the UV wavelength, colloidal silica was used as a test sample for the calibration of excitation source polarization in section 4.1.
Europium particles were chosen which show a larger stokes shift ($\approx$ 250 nm compared to the excitation source wavelength) along with a higher lifetime. Accordingly, the filters at the emission side were chosen based on the analysis of subsection 5.2.5 to remove unwanted emission from the PMMA plastics, laser scattering. The emission peak of the europium particles was found to be 612 nm as shown in Figure 5.2c. The spectra of europium nanoparticles is noisy and a higher integration time was necessary for the europium nanoparticles.

This implies that the europium nanoparticles have a relatively lower quatum yield. This information was further used in the subsection 5.2.4 and subsection 5.2.5 to study the effect of viscosity on phosphorescence quantum yield and anisotropy.

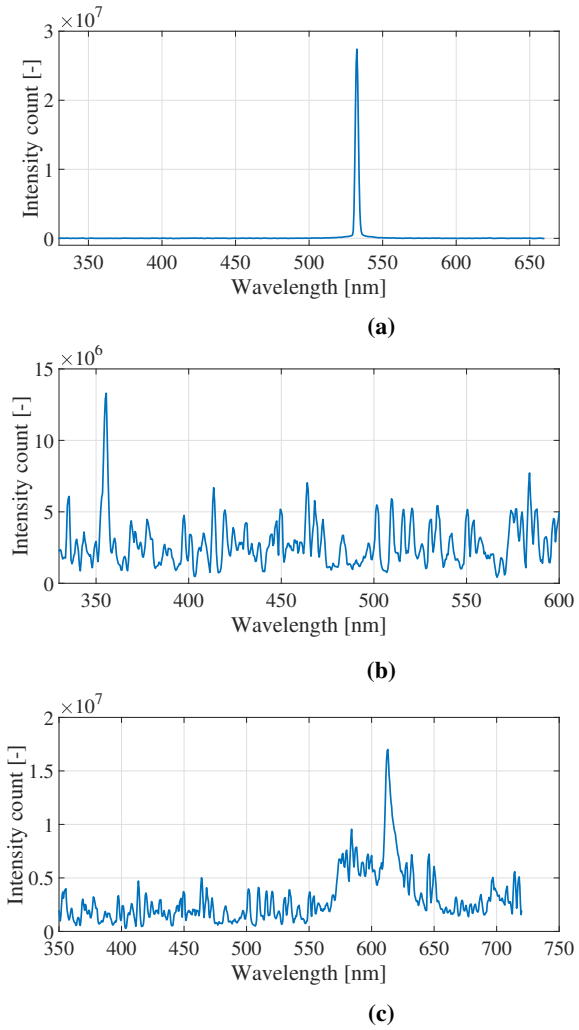

Fig. 5.2 Fig (a) shows the spectrum of colloidal silica when it is excited by 532 nm laser. The integration time of the spectrometer used was 0.5 seconds. Fig (b) shows the spectrum of colloidal silica when it is excited by 355 nm laser. Fig (c) shows the spectrum of europium when it is excited by 355 nm laser. The integration time of the spectrometer used was 6 seconds.

5.1.3 Photo-bleaching studies

As described earlier in the subsection 3.5.2, similar studies were conducted to compute the average time required for the particles before it should be replaced with the fresh set of particles. In the worst-case scenario, to destroy the same set of particles, europium particles were fixed with gelatin using a procedure developed in-house.

The process of fixing the particles was by adding 1.1 g of powdered gelatin from porcine skin to 20 mL of de-ionized water. They were mixed, stirred and left in at the room temperature for it to swell for at least 20

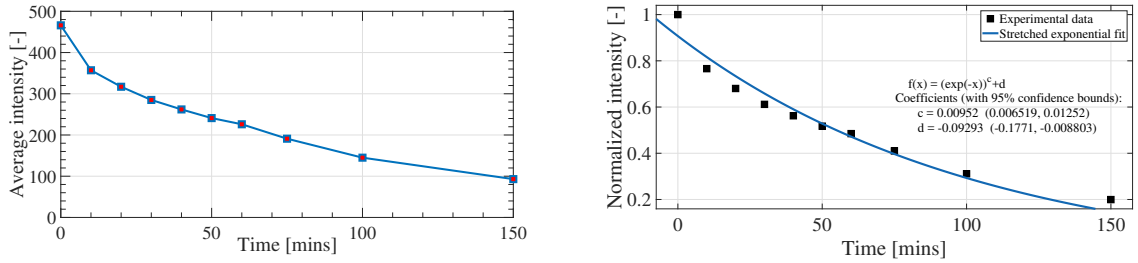

(a) **(b)**

Fig. 5.3 Photo-bleaching tests conducted to study the variation of average intensity with time in minutes in Figure 5.3a. The same figure was normalized with the maximum intensity for fitting the trend-line as shown in Figure 5.3b. The trend-line equation is shown with the value of the respective constants.

minutes. Further, a magnetic stirrer was used with a heating plate to heat the mixture in a silicone oil bath at 65 ^{0}C and simultaneously stirred at 400 rpm. The mixture was removed after it attains 65 ^{0}C and left to cool in the environment for 5 minutes. Then the europium particles were added to obtain the required concentration. After mixing the nanoparticles, they were transferred to cuvettes and stored in the refrigerator for at least 4 hours.
Photo-bleaching studies were conducted with fixed europium nanoparticles (0.05 mg/mL) inside a glass cuvette. Figure 5.3a shows the variation of mean intensity over 3 images with time in minutes. The particles were excited continuously for 150 minutes and the graph shows that the intensity has reduced significantly reaching the background. However, this effect was expected to be less drastic since the particles would be dissolved and moving simultaneously.
A stretched exponential function was fit as described as subsection 3.5.2. Accordingly, the constants in the equation were given as

$$f_\gamma(t) = e^{(-t)^{-c}} + d \tag{5.3}$$

Here d is the random noise from the experiments and c is the stretching constant. The coefficients were given as $c = 0.00952$ and $d = -0.09293$. The R^2 measure for this fit was 95.96 %.
This shows that the decay of the europium based particles was not an exact fit with the stretched exponential function. This may be due to experimental inaccuracies and in-homogeneity in the crystal structure of gelatin and europium particles. The random noise from the laser can depend on the amount of time the laser is running. This information was used in chapter 6 to interpret the results.

5.2 Anisotropy measurements

In this section, the variation of no-flow anisotropy conditions with different parameters is elaborated. subsection 5.2.1 describes the calibration of the emission polarization of experimental setup (section F.2, section 4.1) using scattering solutions. After the calibration of the emission polarization, fundamental anisotropy needs to be measured which is used in section 3.2 to relate it with the angle ε. subsection 5.2.2 computes the fundamental anisotropy (r_0) and the quiescent state phosphorescence anisotropy of the nano-particles. This is performed to compare it with the square duct flow measurements. The subsection 5.2.3 and subsection 5.2.4 study the variation of anisotropy and fluorescence quantum yield with viscosity of the medium and dissolved oxygen. Lastly, the effect of anisotropy with emission filtering using the long pass filters is conducted in subsection 5.2.5.

5.2.1 Calibration of the excitation polarization

Colloidal silica is generally used as a reference scattering medium to calibrate the emission polarization of the experimental setup [87]. Generally, colloidal silica is expected to show anisotropy of 0.95-0.97 for vertically polarized light [17]. This means that colloidal silica could emit a very high proportion of vertically polarized light and an insignificant portion of horizontally polarized light for vertically polarized laser. The apparent absorbance by colloidal silica is less than 5% [40].
Figure 5.4 shows the anisotropy of colloidal silica when excited with lasers of wavelength 532 nm and 355 nm. The concentration of colloidal silica was around 3% by weight. Figure 5.4a shows the average anisotropy of the cropped region as 0.9505 respectively. However, Figure 5.4b show the anisotropy of 0.207. This means that the colloidal silica does not show complete scattering in the UV wavelength region. Unfortunately, the UV laser could not scatter the colloidal silica particles completely, which makes it unsuitable to use it as a reference medium for fixing the excitation polarization. There are previous papers in the past that show that colloidal silica show fluorescence for UV lasers like 308 nm [104]. However, due to the lack of other completely scattering solutions in the UV region, colloidal silica was used to calibrate the experimental setup as described in section 4.1. This is one of the sources of error in the experiments.

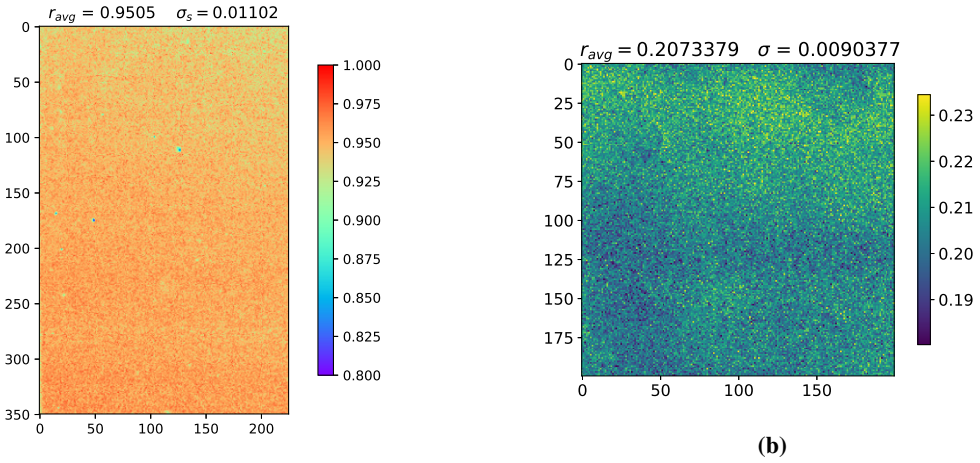

Fig. 5.4 Anisotropy of colloidal silica when excited by 532 nm laser is shown in Fig (a). Anisotropy of colloidal silica when excited by 355 nm laser is shown in Fig (b).

5.2.2 Measuring the anisotropy of nanoparticles in fixed and quiescent flow state

Fixing the particles using gelatin causes vitrification of the sample eliminating rotational diffusion. Vitrification of the sample is the concept which involves cooling a liquid so rapidly that its molecules become immobilized before they have time to crystallize [45]. The particles were fixed using the procedure described in subsection 5.1.3. By fixing the particles using gelatin, it was ensured that the oxygen quenching between the particles and the fluid medium is minimized and the rotational diffusion was reduced. Rotational diffusion is one of the main reasons for depolarization as described in subsection 2.1.1. However, due to the vitrification of the samples, the refractive index of the sample will change slightly causing a change in the quantum yield. This effect was not quantified in this measurement.
This procedure was conducted to measure the fundamental anisotropy using the available measurement equip-

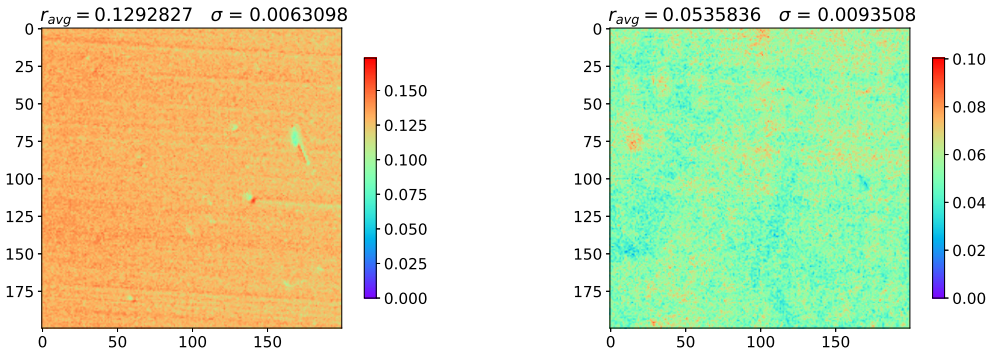

(a) **(b)**

Fig. 5.5 Anisotropy of fixed europium nano-particles using gelatin is shown in Fig (a) and the anisotropy of europium particles in DI water is shown in Fig (b). The average anisotropy has dropped by more than 50%.

ment. The fundamental anisotropy for europium based nano-particles is shown in Figure 5.5a. The fundamental anisotropy of europium particles has an average value of 0.129 ± 0.0063. The average anisotropy value for 5 sets of experiments was found to be approximately 0.12 ± 0.0103. Reifenberger et al. [73] using a CCD imaging spectrometer and a mechanical chopper measured the anisotropy of europium based chelates which was 0.12. This shows that the depolarization sources due to the measurement equipment in this thesis are minimal compared to the [73]. Roughly, the emission and the excitation polarization were calibrated based on the validation of fundamental anisotropy of europium nanoparticles. Using the europium nanoparticles with optimum concentrations as described in subsection 5.2.5, 0.05 mg/mL was used in a transparent 3 mL glass cuvette as shown in Figure 4.4a. Experiments were conducted using the setup in section 4.1. Figure 5.5b shows the phosphorescence anisotropy in DI water. The average anisotropy for 5 sets of measurements was 0.05. The average anisotropy has dropped by more than 50% when compared to fundamental anisotropy. Oxygen quenching, radiative transfer, turbidity and rotational diffusion as described in subsection 2.1.1 act as the main contributors of depolarization in this experiment. This reduces the sensitivity of the vorticity measurements in chapter 6, since the polarization is very low to accurately estimate the vorticity due to depolarization and differentiate it from noise levels.

Using the fundamental anisotropy and the anisotropy in a quiescent state in section 3.3, interpretation of square duct flow measurements in chapter 6 were conducted.

5.2.3 Effect of viscosity on anisotropy

The effect of viscosity on anisotropy as described in subsection 3.5.4 which revolves around the Perrin equation (Equation 3.28). The anisotropy was measured for europium based particles in different mixtures of glycerol and methanol accordingly in the setup as described in section 4.1. This is shown in Figure 5.6 and all the data was tabulated in Table 5.1. In the table, the viscosity of the mixtures, the dielectric constant and the refractive index were referred from [43]. These experiments were conducted with a 3 mL sample. Homogeneous solutions with the nano-particles were prepared using a magnetic stirrer.

Generally, molecular rotars were used as optical viscosity probes as conducted by Levitt et al. [43]. However, in this case, lanthanide nanoparticles could be used since they show longer lifetimes compared to generic fluorescent molecules (rhodamine, eosin Y). In Figure 5.6 the analytical model was the Perrin equation (Equa-

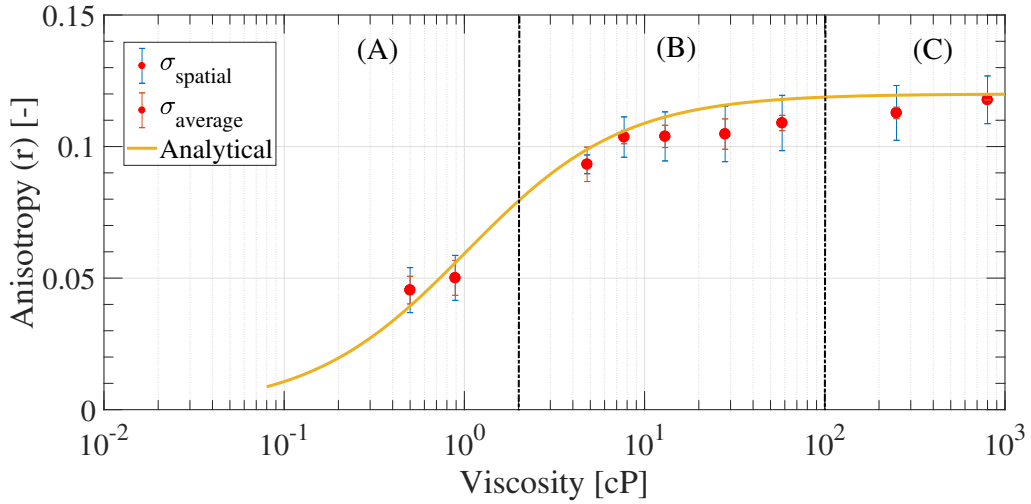

Fig. 5.6 Variation of anisotropy of europium with log of viscosity in centipoise for different percentages of methanol and glycerol plotted along with analytical model from Equation 3.28. The regions (A), (B) and (C) represent the low viscosity, medium viscosity, and high viscosity solutions respectively. The spatial error bar which depends on the dimensions of the cropped image and the average error bar is computed from three sets of experiments. The average anisotropy is tabulated in Table 5.1.The average anisotropy is tabulated in Table 5.1.

tion 3.28). The differences between the analytical and experimental models are due to multiple reasons. Higher volumes of the sample cause more error due to non-uniformities of mixing between methanol and glycerol. Generally, all the experiments generally concerned with micro-viscosity are conducted with microscopic HeLa cell samples which gives highly accurate results.

The three regions in Figure 5.6 are; low viscosity (A), medium viscosity (B) and high viscosity solutions (C). In solvents of very low viscosity, the anisotropy reaches a minimum value. In the media of high viscosity, the non-radiative de-excitation rate caused due to internal rotation becomes negligible and the anisotropy reaches very close to the anisotropy of vitrified particles. For the highest viscosity (900 cP) the measured anisotropy was the same as the anisotropy for vitrified samples. In the case of intermediate viscosities (B), these nano-particles could be used to estimate the fluidity of a medium because of higher gradients compared to region (C). The spatial standard deviation inside the cropped focused image was caused by the laser aberrations and the nonuniform mixing in the sample. The average standard deviation was calculated from three samples of the same glycerol and methanol mixtures with the same concentration of europium particles. The effect of change in refractive index and the dielectric constant on anisotropy as shown in Table 5.1 [43] was not accounted for in the measurements. All the above possible error sources led to the deviation between the analytical model and experimental data. However, the possibility of using europium based particles as optical viscosity probes can be extended with precise experimental equipment for accurate results.

This study shows the possibility of employing europium nanoparticles as viscosity probes in fluids based on anisotropy which revolves around Perrin equation.

Table 5.1 Anisotropy of europium nanoparticles for different concentrations of glycerol and methanol binary mixture as shown in the first column. The second, third and the fourth columns shows the respective viscosity, dielectric constant and the refractive index from [43]. Last column shows the average anisotropy of the europium particles. The average anisotropy along with error bars are plotted in the Figure 5.6.

Percentage of glycerol (%) in methanol and glycerol mixture	Viscosity (25 °C) in cP [43]	Dielectric Constant (ε) [1] [43]	Refractive index (n) [43]	Average anisotropy of europium (r)
0	0.5	33	1.339	0.0454
DI H_2O (100%)	0.89	33.3	1.3521	0.0508
20	4.8	33.7	1.3704	0.0932
30	7.7	36.7	1.3857	0.1036
40	13	37.6	1.403	0.1038
50	28	38.6	1.4172	0.1047
60	58	39.3	1.432	0.1089
80	250	40.8	1.4538	0.1127
>95	900	41.4	1.4645	0.1177

5.2.4 Effect of viscosity on phosphorescence quantum yield

Many authors in the past tried to relate the properties of quantum yield to the properties of the fluid medium as described in subsection 2.1.3. In this section, the variation of quantum yield with the viscosity in the fluid medium is studied. For a binary mixture of glycerol and methanol with different weight fractions in addition with 0.05 mg/mL of europium nanoparticles, the variation of quantum yield was studied using the experimental setup in section 4.2. The rise in quantum yield was observed as shown in Figure 5.7.

Increasing the weight fraction of glycerol in the binary mixture will result in increase in viscosity. Increase in the concentration of glycerol also reduces the dissolved oxygen in the fluid medium [77]. Walter et al. [95] showed that the quantum yield of europium based compounds does not change when the dissolved oxygen is varied by comparing the air equilibrated and degassed solutions. Hence, based on this hypothesis it is believed that the increase in the quantum yield is due to the increase in the viscosity. Higher viscosity fluids impede the rotations of the luminescent nanoparticles which decreases the non-radiative constant and increases the quantum yield from the Equation 2.1. This study shows the possibility of employing europium nanoparticles as viscosity probes in fluids based on quantum yield with proper calibration.

However, the effects of solvent polarity is still under discretion to completely analyze its effect on luminescent particles.

5.2.5 Effect of filtering and concentration

Fluorescence or phosphorescence quantum yield varies with its concentration in the fluid medium. This might result in the variation of anisotropy. If the concentration is too less, the quantum yield will be very low. For steady-state measurements, very high exposure would be needed making the experimental results prone to error over a longer time. Very high concentrations lead to high laser scattering between the particles, between the PMMA shell and the particles which result in an erroneous scattering component in the Equation 2.7. The range of concentrations between 0.01 mg/mL to 0.1 mg/mL was found to be optimum.

The variation of anisotropy with emission side filtering is important to check if there is any erroneous laser

[1] Levitt et al. [43] where the values are computed using $\varepsilon = \phi_m \varepsilon_m + \phi_g \varepsilon_g$ where, ϕ is the weight fraction and m and g are subscripts for methanol and glycerol respectively

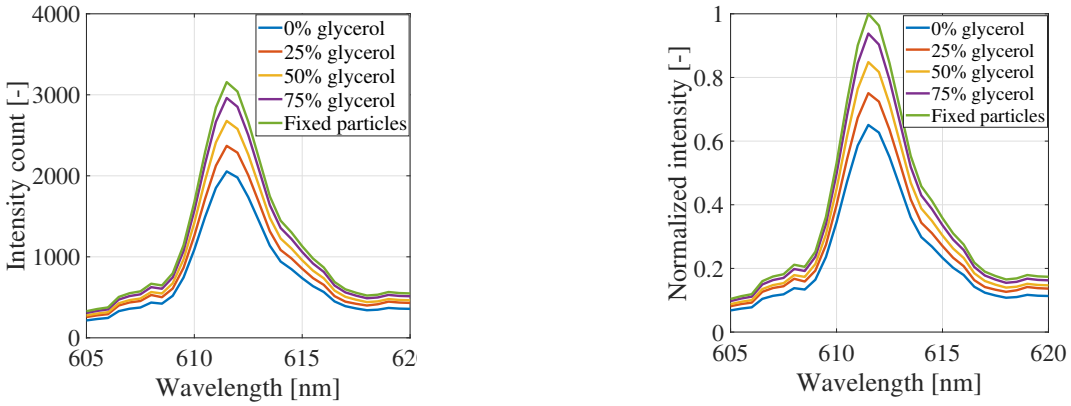

(a) **(b)**

Fig. 5.7 Variation of europium nanoparticles intensity with the wavelength for different glycerol percentages in binary mixture of glycerol and methanol as shown in Fig (a) and its normalized graph Fig (b). As the glycerol percentage is increasing, viscosity of the fluid increases leading to an increase in the quantum yield.

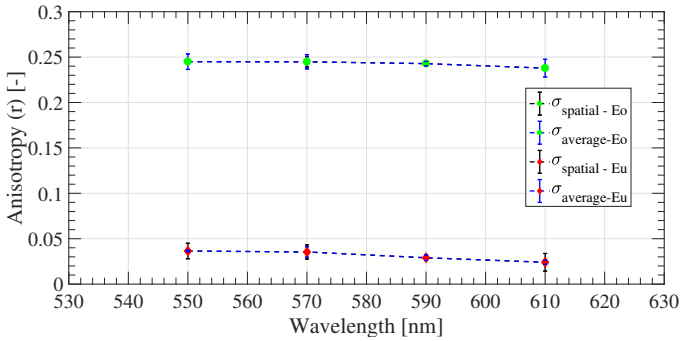

Fig. 5.8 Variation of anisotropy of eosin Y and europium in DI water using different long pass wavelength filters at the emission side in the experimental setups as described in section F.2 and section 4.1 respectively. In the legend, Eo represents eosin Y nanoparticles and Eu represents europium based nanoparticles.

scattering that is accumulated in the emission intensity. Four long-pass filters (550 nm, 570 nm, 590 nm, and 610 nm) were chosen as the emission side filters along with the short pass filter (643 nm) in the experimental setup (section 4.1). Respective anisotropy after 5 sets of experiments for both eosin Y (section F.2) and europium based particles (section 4.1) were plotted as shown in Figure 5.8. The emission anisotropy is nearly flat for eosin Y but drops slightly after 610 nm for europium based nano-particles. This is due to the removal of half of the quantum yield after 610 nm. To capture the remaining half spectra, the exposure time of the measurements was increased, which will show more depolarization effects. However, in chapter 6, the long-pass filter of wavelength 570 nm was used along with a short pass filter (643 nm) for europium based particles in the setup described in section 4.1.

Based on the above preliminary studies as a reference, experiments were conducted on the turbulent duct flows in chapter 6.

Chapter 6

Turbulent duct flows

In this chapter, the two approaches described in Figure 1.1 are elaborated. In section 6.1, approach 2 (indicated in green arrows) is described. Using the known DNS vorticity data [67] as input, the variation of the analytical correlations with different parameters shown in the Appendix D is studied. In section 6.2, the contours from the experiments are shown for Re = 4434 and Re = 0. They are compared only qualitatively due to high measurement error, showing the regions of interest which need to be further processed. The section 6.3 elaborates on the variation of intensity and anisotropy by plotting them as column averages for Re = 0, 2664, 4434 and 6208. From the methodology undertaken in this thesis (Figure 1.1), the final objective of approach 2 is discussed in section 6.4. The final objective of approach 1 is discussed in section 6.5 by employing the optimization algorithm. Finally section 6.6, describes the sensitivity of this technique by conducting the repeatability tests for Re = 4434.

6.1 Interpretation of synthetic signals using DNS data

The synthetic signals computed from analytical relations in Appendix D are dependent on the following parameters as shown below,

$$\{D_{zv}, D_{zh}, D_{yv}, D_{yh}\} = \text{function}(\omega_x, \omega_y, \omega_z, \varepsilon, \tau_c, \tau_f) \tag{6.1}$$

Here the vorticity components are from Rodrigues' rotation formula as shown in Equation 3.15 and Equation 3.16. Employing mean vorticity components from DNS data [67], the variation of analytical formulae as shown in Appendix D is analyzed. The parameters of the above function is shown in Table 6.1.

Table 6.1 List of all the mean input parameters of Equation 6.1 which were measured or computed in the previous chapters.

Quantity	Value
r_0	0.12
τ_f	240 μs subsection 5.1.1
τ_c	194 μs subsection 3.5.3
Vorticity DNS data	Pirozzoli et al. [67] (Re = 4400, 7000 and 17000)

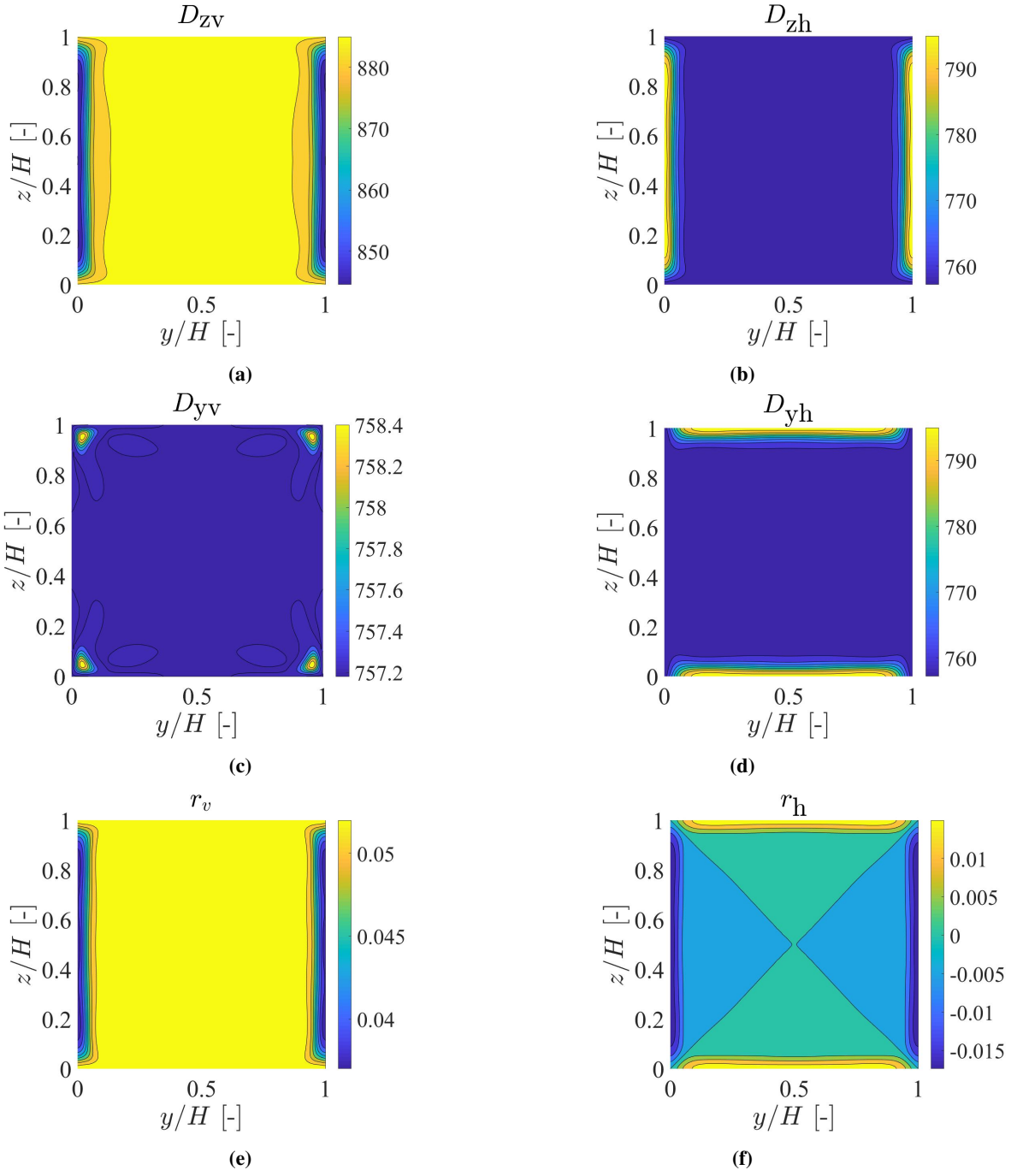

Fig. 6.1 The above images show the intensity images and variations of anisotropy at Re = 4400 for the cross section of the square duct 4×4 mm^2. These signals were computed using DNS vorticity data [67] as user input to compute the signals in the formulae in Appendix D. Fig (a) shows the time integrated signals for D_{zv}. Fig (b) shows the time integrated signals for D_{zh}. Fig (c) shows the time integrated signals for D_{yv}. Fig (d) shows the time integrated signals for D_{yh}. Fig (e) shows the anisotropy for vertically polarized laser r_v and Fig (f) shows the anisotropy for horizontally polarized laser r_h.

Before doing further analysis, it is important to check if the anisotropy of the nanoparticles in quiescent flow state is same for the glass square duct and the optical glass fluorescence cuvette. Because of the thicker glass substrate in the glass square duct, erroneous laser scattering might result in wrong emission anisotropy. However, the average anisotropy was found to be in the same order of 0.05 as shown in subsection 5.2.2. The average anisotropy can also reduce when the anisotropy experiments are conducted in moving fluids due to higher scattering from the shell of the nanoparticles, depending on their concentration. This will be elaborated in section 6.3.

Using Re = 4400 of DNS data in the correlations as given by Appendix D, Figure 6.1 was plotted. Figure 6.1a shows the contour of the signal D_{zv} which is increasing from the edges to the core of the duct. Figure 6.1b shows the contour of the signal D_{zh} which reduces from the edges to the core of the duct. Figure 6.1c shows a small variation near the corners in D_{yv}. Figure 6.1d shows the variation of D_{yh} along the top edges of the square duct. Another main observation is that, the average intensity of the contour D_{zv}, is higher than the rest of the intensity signals. Figure 6.1e shows a gradual increase in anisotropy from the edges to the centre in r_v. Figure 6.1f shows insignificant variation of anisotropy in the cross-section of duct as shown in r_h. The coordinate system which was used in the experiments and its relation with DNS data is shown in Figure 6.2. All the synthetic signals and the results from the experiments are shown in $z-y$ plane. For accurate estimation of vorticity, the results from the experiments should match the Figure 6.1 for each of the respective signals. Hence, these signals are compared with the experiments in section 6.2.

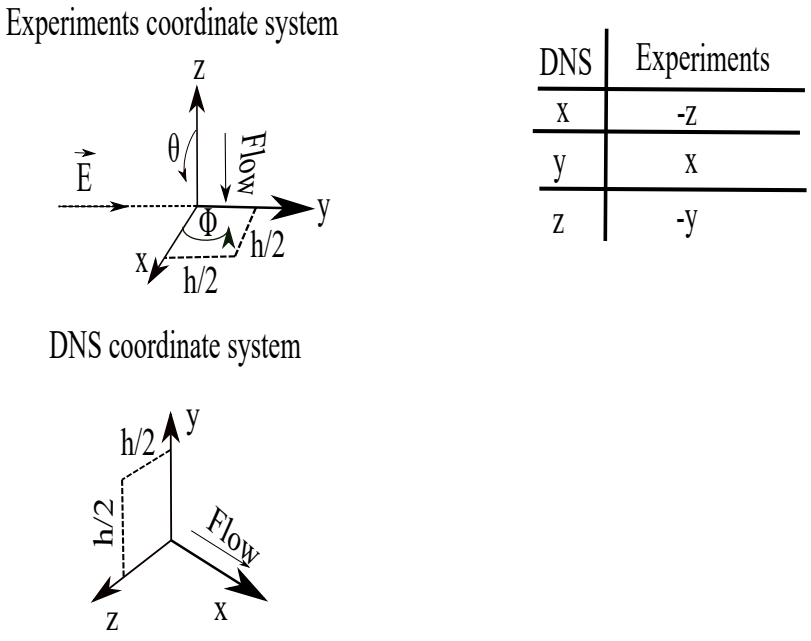

Fig. 6.2 The coordinate systems used in the experiment to derive the analytical correlations in section 3.3 and the coordinate system used in the DNS by Pirozzoli et al. [67] are shown above. The two coordinate systems have to be related to interpret the vorticity results. The relation between these two is with respect to flow directions are shown in the table above. $\vec{E}$ is the excitation source and h is the half channel width.

Before that, since the correlations in Appendix D depend on various parameters, it is important to understand the effect of each parameter individually on the anisotropy. The subsection 6.1.1 shows the variation of Re

on r_v and r_h. As Re increases, the non-dimensional number ND1 (Equation 3.26) increases in the boundary layer, due to the rise in vorticity. The subsection 6.1.2 shows the variation of r_v and r_h with the fundamental anisotropy. The subsection 6.1.3 shows the variation of r_v and r_h with the non-dimensional number ND2 as introduced in Equation 3.27. This is done to support the hypothesis proposed in subsection 3.5.3. The reference values for each comparison study is shown in Table 6.1.
To understand the time integrated intensity signals, anisotropy due to vertically polarized laser (r_v) and horizontally polarized laser (r_h) which were derived from Equation 1.2, was computed.

$$r_v = \frac{D_{zv} - D_{yv}}{D_{zv} + 2D_{yv}} \tag{6.2}$$

$$r_h = \frac{D_{yh} - D_{zh}}{D_{yh} + 2D_{zh}} \tag{6.3}$$

6.1.1 Effect of Re

The DNS of three different Re = 4400, 7000 and 17000 published by Pirozzoli et al. [67] was used as the input for the vorticity components. These vorticity components obtained from DNS are plotted for the half width of the square duct h. The variation of column-averaged r_v and r_h for different Re with Table 6.1, was shown in Figure 6.3. Figure 6.3a shows that the anisotropy is nearly constant in the core of the square duct and the percentage of depolarization has increased with the increase in Re. Figure 6.3b shows a similar trend with the decrease in anisotropy along the edges.
The trend of r_v is similar to the turbulent boundary layer of the flow. As Re increases, the boundary layer becomes thinner reducing the viscous sub-layer width. Further in addition to the rise in Re, the magnitude of vorticity increases implying a higher reduction in anisotropy compared to the quiescent flow anisotropy. As vorticity increases, the value of ND1 rises, which increases the resolution of accuracy of the vorticity measurements. The r_h also shows similar trend. However, for higher Re, the percentage of decrease in anisotropy for europium nanoparticles cannot be estimated since the anisotropy available for estimating vorticity is only 0.05 in the quiescent flow state. This can be fixed by choosing the particles with higher r_0 in the future.

6.1.2 Effect of fundamental anisotropy r_0

Fundamental anisotropy r_0 as measured in subsection 5.2.2 is a very important parameter which decides the sensitivity of the vorticity measurements. Figure 6.4 shows the column averaged variation of r_v and r_h for different r_0 at Re = 4400, keeping rest of the input parameters same as shown in Table 6.1. By varying the r_0, angle ε is computed using Equation 3.9. Figure 6.4a shows that, as r_0 increases the magnitude of depolarization rises along the edges due to vorticity. Figure 6.4b shows a similar trend. Table 6.2 shows the highest magnitude of depolarization for both r_v and r_h at different r_0.
This means that the sensitivity of the estimated vorticity due to r_0 is not affected significantly as long as r is higher than the noise levels from the measurements. However, the slight increase in depolarization for higher r_0 provides larger room for the estimation of vorticity at the same Re. From the Perrin equation (Equation 3.28), using r_0, the value of r is computed. From Equation 3.9, higher the value of r_0, higher is the value of anisotropy in the state of quiescent flow r. This increases the resolution of the estimation of vorticity by measuring depolarization, making the technique more employable at higher Re (more room for depolarization, For example: eosin Y).

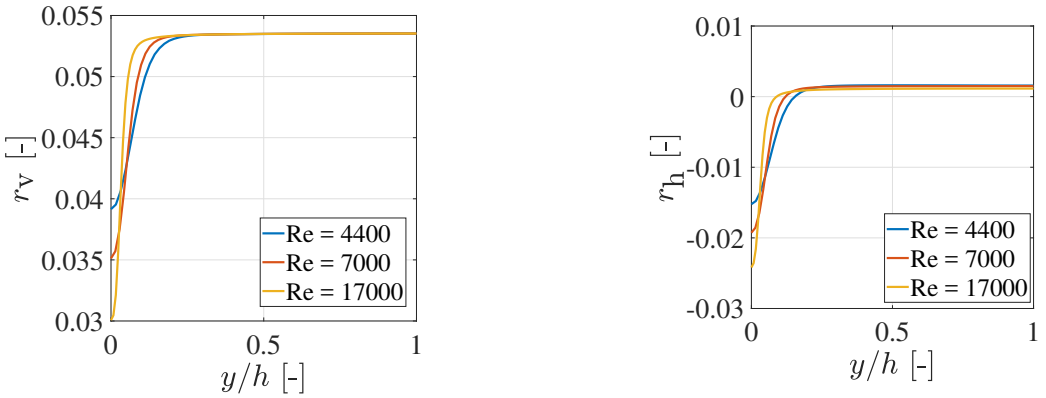

(a) **(b)**

Fig. 6.3 Variation of column averaged vertically polarized excitation anisotropy r_v and horizontally excited laser anisotropy r_h for different Re shown for half duct width. Fig (a) shows that as Re increases, r_v along the edges is further reduced. It can also be observed that as Re increases, the drop in anisotropy region reduces because of the reduction in the boundary layer width. Fig (b) also shows that as Re increases the r_h is increasing tending towards 0.

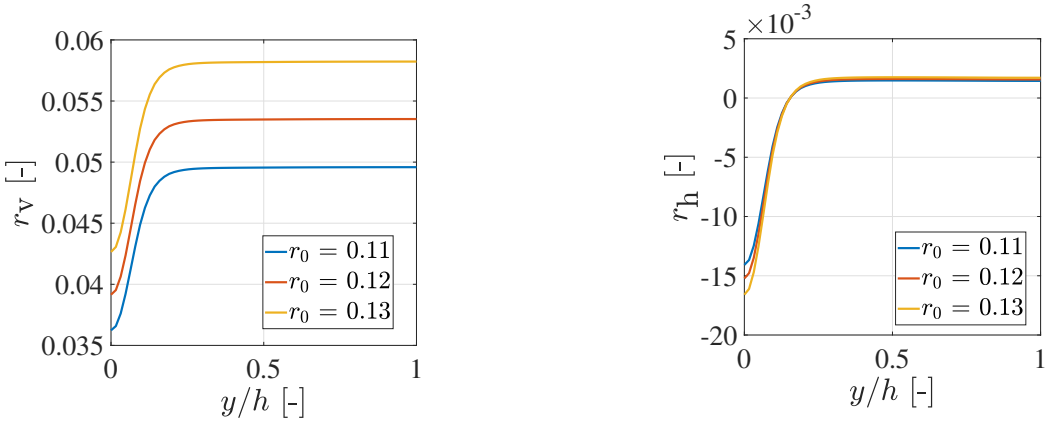

(a) **(b)**

Fig. 6.4 Variation of column averaged vertically polarized excitation anisotropy r_v and horizontally polarized excitation anisotropy r_h at Re = 4400, for different r_0 which is related to the the angle between the absorption and emission moments as shown in Equation 3.9. Fig (a) and Fig (b) shows that as the fundamental anisotropy increases, r_v and r_h will increase in magnitude at the core and the edges of the square duct.

Table 6.2 Variation of magnitude of depolarization for both r_v and r_h at different r_0 as shown in Figure 6.4. Higher the depolarization, higher is the sensitivity towards vorticity estimation.

Quantity	$r_{v,max}$ - $r_{v,min}$	$r_{h,max}$ - $r_{h,min}$
$r_0 = 0.11$	0.01331	0.015524
$r_0 = 0.12$	0.01436	0.016823
$r_0 = 0.13$	0.01556	0.017717

6.1.3 Effect of non-dimensional number ND2

In this subsection, ND2 is varied by changing the lifetime of the nanoparticles τ_f and keeping the correlation time τ_c constant.

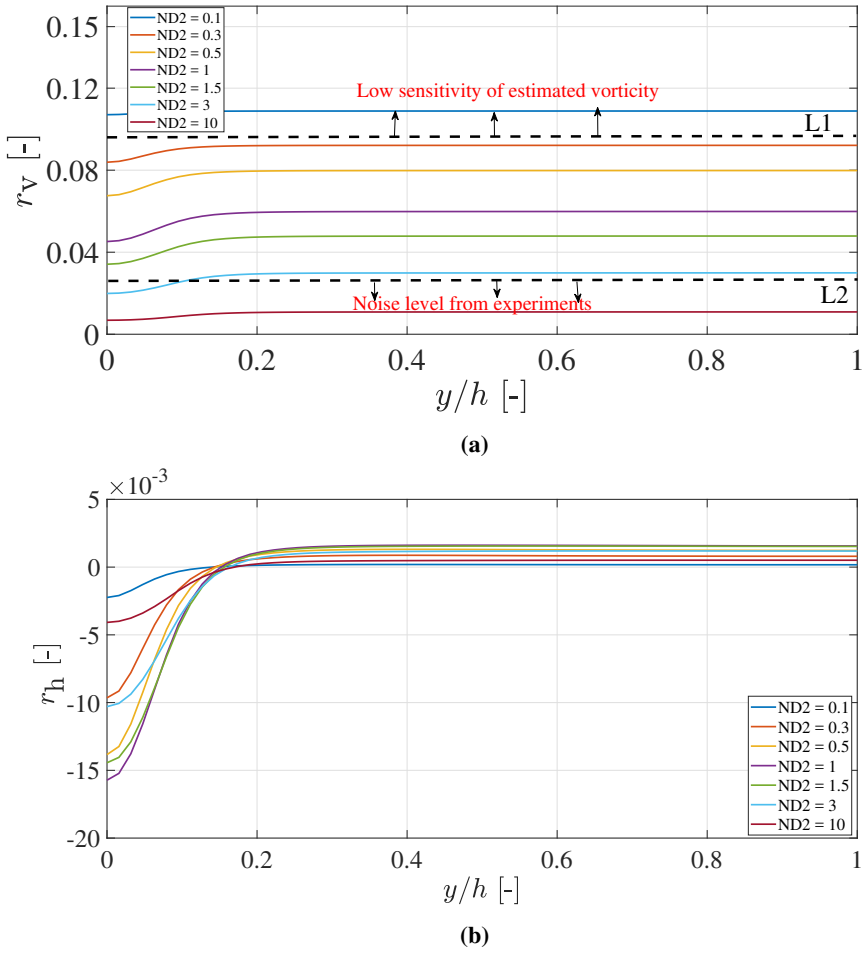

Fig. 6.5 Variation of column averaged vertically polarized excitation anisotropy r_v and horizontally polarized excitation anisotropy r_h for different non-dimensional numbers ND2 Equation 3.27. Fig (a) shows two lines L1 and L2. Lines L1 and L2 show the regions where it is not suitable for conducting measurements. Similar behavior is shown in the Fig (b). The experiments were conducted with ND2 in between the regions L1 and L2 as shown in the Table 3.1. The above graph shows the importance of ND2 when this experimental setup has to be designed.

The variation of non-dimensional number ND2 as introduced in Equation 3.27 is studied in this subsection by varying the τ_f and keeping rest of the parameters same as Table 6.1 at Re = 4400. Figure 6.5 shows the variation of r_v and r_h for different ND2 at Re = 4400. Figure 6.5a shows the two lines L1 and L2. As ND2 reduces, r_v increases. But above the line L1, the sensitivity of vorticity estimation reduces since the drop in r_v due to the vorticity along the edges is lower and the value of r_0 is fixed. This fixes the upper bound of the ND2 for a particular Re. For higher vorticity at higher Re in the boundary layer, the magnitude of depolarization increases pushing line L1 higher. This means that the bandwidth of ND2 depends on the Re.
Below the line L2, for a high ND2, the r_v drops entirely along the square duct. This is the threshold line

below which it is not possible to measure the anisotropy due to the noise level from the experimental setup (section 4.1). So, depending on the noise levels from the experiments, the position of the line L2 can be gauged. In this thesis, ND2 is between the two lines L1 and L2 making it suitable for this measurement technique as shown in Table 3.1.

Figure 6.5b shows the optimum range for ND2 since for ND2 = 0.1 and ND2 = 10, the variation of r_h shows a similar trend. For the rest of the ND2, depolarization near the edges is much higher, implying that the optimum range for ND2 is definitely between 0.05 and 30. For optimum sensitivity of vorticity estimation, the range of ND2 should be between 0.3 to 3 considering the noise levels (higher ND2) and the reduced sensitivity at lower ND2.

Ideally, for higher limits of ND2 which means higher lifetimes the technique should work based on ND1. However this is not reflected in Figure 6.5a because of the mathematical formulation used in Equation 3.20. Since the time integrated signals are integrated from t = 0 to ∞ (over complete lifetime), the correlations are not able to take into account the rotations occurring in intermediate timesteps. This is one of the limitation of the analytical correlations (Appendix D).

6.2 Comparison of contours from experimental results at Re = 0 and Re = 4434

In this section, the synthetic signals as shown in Figure 6.1 are compared with the results obtained from experimental setup (section 4.1). This shows the comparison of contours at Re = 0 and Re = 4434, for the signals I_{zv}, I_{zh}, I_{yv}, I_{yh}, r_v and r_h. These images are median filtered in 2D, by a 3×3 matrix.

Figure 6.6 shows the contour at Re = 4434 (first column) and Re = 0 (second column) for the signals I_{zv}, I_{zh}, I_{yv} which is non-dimensionalized for a quarter section of the square duct. Figure 6.7 shows contour at Re = 4434 (first column) and Re = 0 (second column) for the signals I_{yh}, r_v, r_h. The important regions which need to be analyzed depending on the type of signal is marked in red dotted rectangles, which can be inferred from Figure 6.1.

Ideally, the intensity images for Re = 0 should not show any variation in intensity. The contours in column two shows variation because of few reasons. Firstly, the major reason is the variation of intensity of the laser along the laser sheet because of the 3D Gaussian distribution of the laser sheet from the optics. Due to the varying intensity of the laser beam, the photo-bleaching effect at each particle as described in subsection 5.1.3 will vary depending on the intensity of the laser. However, for every experiment fresh set of particles was chosen to reduce the effect of photo-bleaching on the results. Shot to shot variation of the laser shot is not significant as described in the Figure 4.6b.

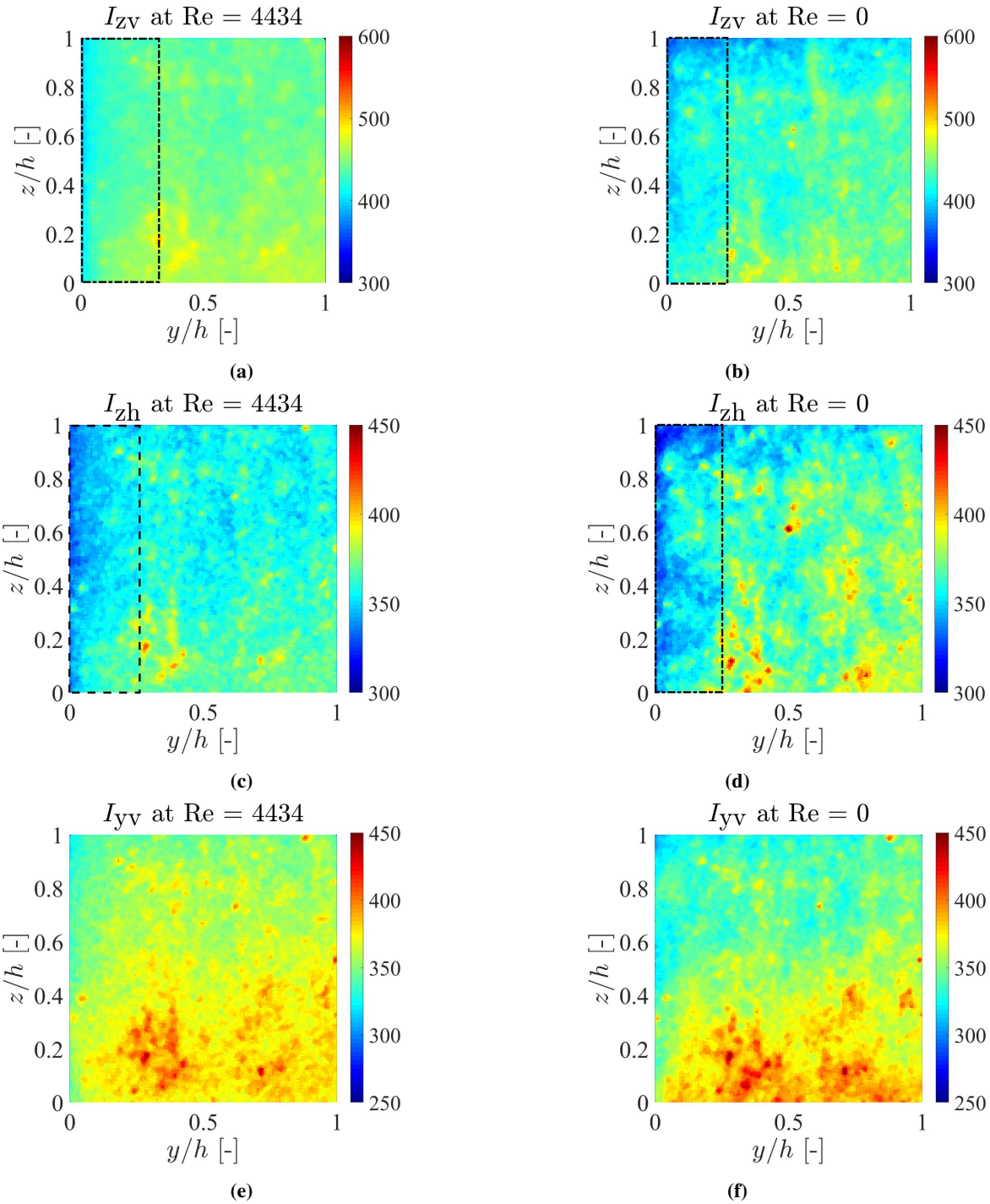

Fig. 6.6 The above images shows the intensity images at Re = 4434 for the cross section of the square duct 2×2 mm^2. These signals were obtained from the experimental setup section 4.1. Fig (a) shows the intensity signal I_{zv} at Re = 4434. Fig (b) shows the intensity signal I_{zv} at Re = 0. Fig (c) shows the intensity signal I_{zh} at Re = 4434. Fig (d) shows the intensity signal I_{zh} at Re = 0. Fig (e) shows the intensity signal I_{yv} at Re = 4434. Fig (f) shows the intensity signal I_{yv} at Re = 0. The important regions are marked in black rectangle with respect to Figure 6.1 which is further processed.

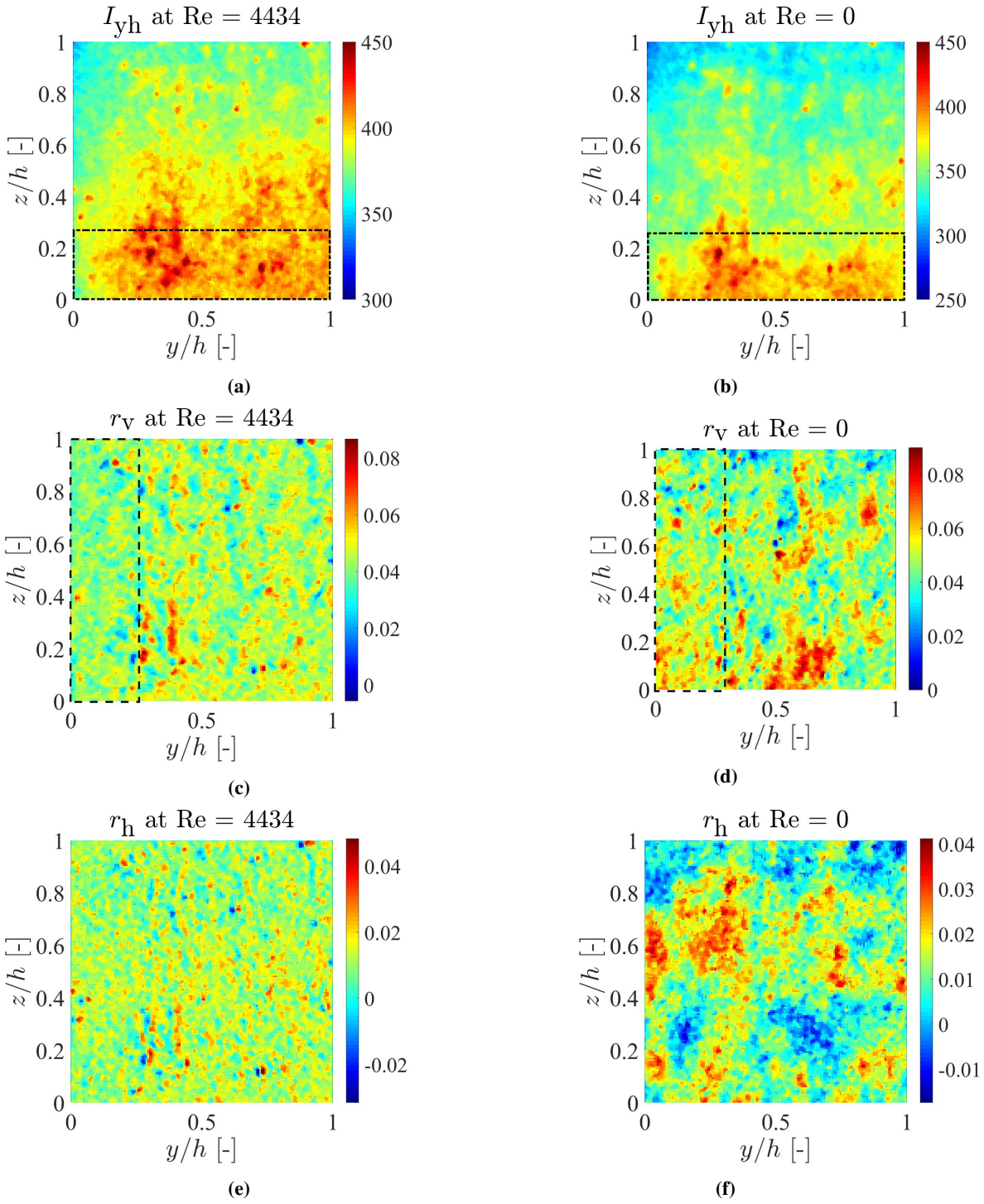

Fig. 6.7 The above images show the intensity images and variations of anisotropy at Re = 4434 for the cross section of the square duct 2×2 mm^2. These signals were obtained from the experimental setup section 4.1. Fig (a) shows the intensity signal I_{yh} at Re = 4434. Fig (b) shows the intensity signal I_{yh} at Re = 0. Fig (c) shows the anisotropy r_v at Re = 4434. Fig (d) shows the anisotropy r_v at Re = 0. Fig (e) shows the anisotropy r_h at Re = 4434. Fig (f) shows the anisotropy r_h at Re = 0. The important regions are marked in black rectangle with respect to Figure 6.1 which is further processed.

The noise from the camera is insignificant since the standard deviation in the background image with the laser off mode is less than 2%. The main reason is the variation of laser intensity, assuming uniform concentration of nanoparticles in the duct. To second this, consider Figure 6.6e and Figure 6.6f. From the synthetic signal D_{yv} Figure 6.1c, the intensity variation is less than 2 counts. This means that although they cannot be compared directly with the experimental results due to magnification factor I_0, the expected variation of I_{yv} in the experiments should be lower than the other signals. Hence, considering the noise level from the experiments, Re = 4434 and Re = 0 should show very similar contours as shown in Figure 6.6e and Figure 6.6f. Very few observations from the contours can be discussed, before tackling the issue of inhomogeneities in the intensity and pulse to pulse variations. Figure 6.6a and Figure 6.6b are compared with the region of interest marked in a dashed rectangle. From the Figure 6.1a, a rise in the intensity I_{zv} should be observed from the edges to the core of the duct. These trends are observed for both Re = 4434 and Re = 0, however the slope of their variations near the edges should be compared. The expected trend in Figure 6.6a as compared to Figure 6.1a cannot be explicitly observed in the black dotted rectangle. The average intensity of the signal D_{zv} is higher than D_{zh}, D_{yv} and D_{yh}. This is observed from the experiments as well for intensity I_{zv}. Similarly, the trend in Figure 6.6c and Figure 6.6d inside the rectangular block cannot be compared with Figure 6.6c because of the similar noise levels. However, Figure 6.7a show a rise in intensity variation in the black dashed rectangle compared to Figure 6.7b, but the trend cannot be observed clearly.

The variation in anisotropy can be explained here. In Figure 6.7c, r_v shows a lower anisotropy in the black dashed rectangle compared to the Figure 6.7d. This means that the anisotropy is increasing from the edges to the center of the square duct. A similar trend is observed in Figure 6.1e however, this quantification is difficult because of the noise levels. Similarly in Figure 6.7e, r_h shows the contour between 0.01-0.02. This includes the noise from the experimental setup and the actual variation of r_h due to vorticity. This is seconded by the synthetic signal as shown in Figure 6.1f. However, Figure 6.7f shows similar anisotropy values compared to Figure 6.7e. This implies that the anisotropy r_h cannot be distinctively separated from the noise, because of comparable noise levels.

To interpret these results and to reduce the ambiguity in the interpretation of results, column averages of the respective contours were taken and compared for four Re = 0, 2660, 4434 and 6208. They are discussed in section 6.3.

6.3 Variation of column-averaged experimental results for Re = 0, 2660, 4434 and 6208

In this section, column averages of the variation of intensity and anisotropy are studied to understand their variation along the y-axis. Figure 6.8 shows the variation of I_{zv}, I_{zh}, I_{yv}, I_{yh}, r_v and r_h at Re = 0, 2660, 4434 and 6208. They are column averaged over the contour and normalized by their respective minimum values to observe the trends and to ignore the effect of intensity variations at different Re. Figure 6.8a shows the variation of the intensity I_{zv}, Figure 6.8b shows the variation of the intensity I_{zh}, Figure 6.8c shows the variation of the intensity I_{yv}, Figure 6.8d shows the variation of the intensity I_{yh}, Figure 6.8e shows the variation of the intensity r_v and Figure 6.8f shows the variation of the intensity r_h. These are obtained by averaging the contours in Figure 6.6 and Figure 6.7 along the column (z/h) .

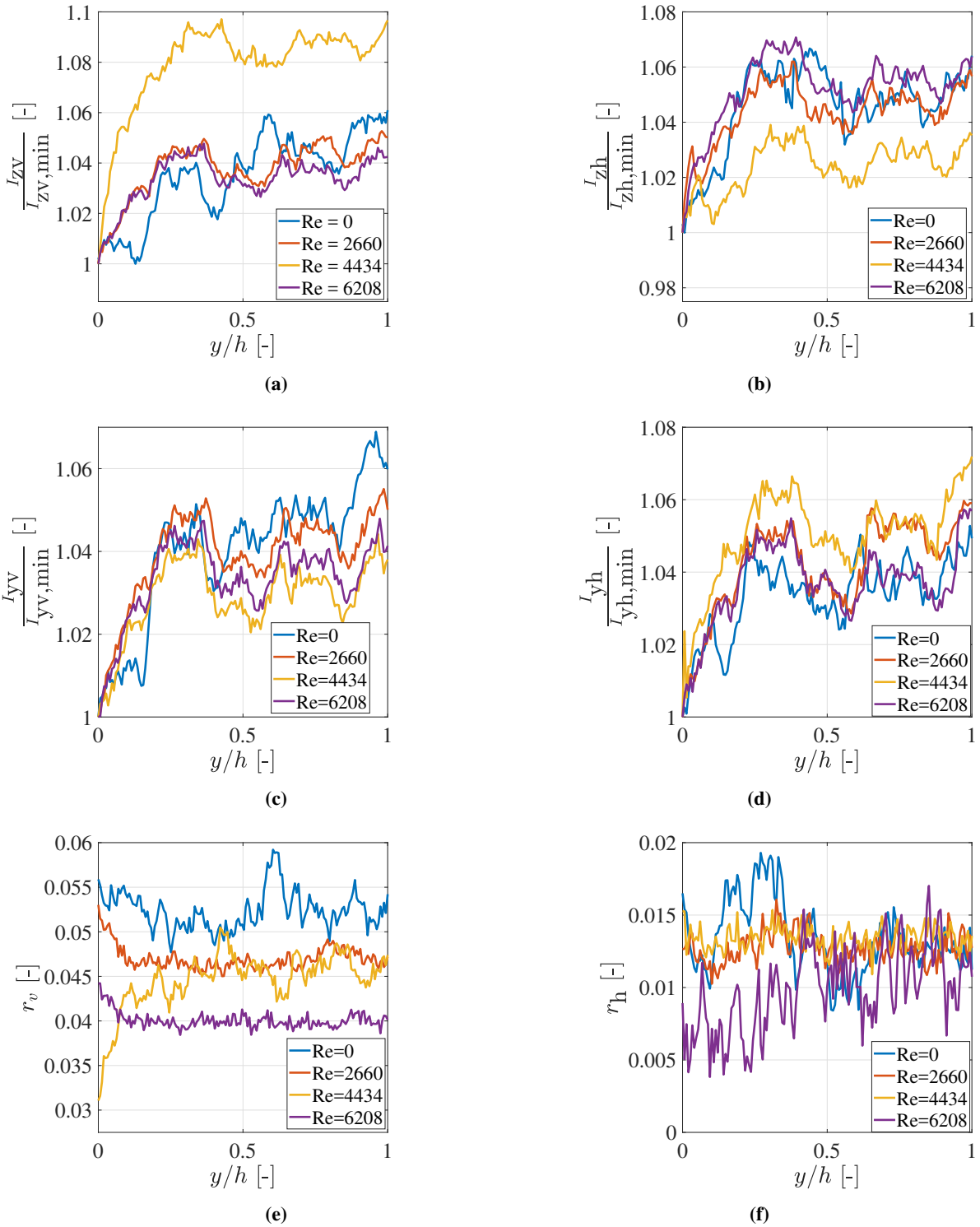

Fig. 6.8 The above plots show the variation of non-dimensional intensities over half width of square duct for Re = 0, 2660, 4434 and 6208. Fig (a) shows the variation of normalized intensity I_{zv}. Fig (b) shows the variation of normalized intensity I_{zh}. Fig (c) shows the variation of normalized intensity I_{yv}. Fig (d) shows the variation of normalized intensity I_{yh}. Fig (e) shows the variation of vertically polarized laser r_v. Fig (f) shows the variation of anisotropy of horizontally polarized laser r_h. The standard deviation plots are shown in Appendix I.

Figure 6.8a shows that for the Re = 4434 case, there is a difference in the slope of intensity variation, compared to the Re = 0 case. Ideally for Re = 0 case, the graphs should show a horizontal line which is equal to 1 for all the intensity orientations. However, because of the error in the measurement, the normalized intensity varies from 1 to 1.06. Similar trends are shown for Re = 2660 and 6208 cases. For Re = 2660 case, the non-dimensional number ND1 is close to zero because of the lower magnitude of the vorticity. For Re = 6208 case, the width of the boundary layer as shown by ω_y and ω_z might be less than 0.3 mm. However, the width of the laser sheet in this experiment is 0.5 mm. This means that the Re = 6208 case and above should behave similar to Re = 0. This is observed clearly in Figure 6.8a. Accordingly, the noise levels for intensity variation when they are column averaged can be gauged to around 6%.

Figure 6.8b shows that for Re = 4434 case, there is a difference of intensity I_{zh} variation compared to the Re = 0. The Re = 4434 case shows a small intensity drop compared to the rest of the Re. Although this is in the range of noise level, this difference in behavior of intensity for Re = 4434 and rest of the Re is considered due to the vorticity in the flow. However, it cannot be concluded that this drop is caused due to vorticity.

Similar trends are observed for Re = 0, 2660 and 6208. Figure 6.8c for I_{yv} shows similar trends for all the Re. This is because of the variation of small variation of intensity in Figure 6.1c (less than 2 counts) compared to the rest of the signals. From the experiments, this cannot be measured because of measurement error from the setup. Hence a similar trend is observed for all the Re. This also shows that the measurement error is approximately 6%.

Figure 6.8d shows the very similar variation of intensity I_{yh} for all the Re with a very small increase for Re = 4434 with respect to Re = 0. This is because these plots are column averaged by normalizing with their minimum values in their respective columns. From the synthetic signal Figure 6.1d, the expected variation of intensity is near the bottom edge of the cross-section. When this contour is column-averaged, only a small variation of intensity is observed since the variation of intensity along the column is lower. This change in intensity is very low to be captured by this experimental setup. Hence the variation of I_{yh} along y-axis is similar for all the Re.

The main idea behind this technique is depolarization due to vorticity. This is shown in Figure 6.8e for different Re. For Re = 4434 case, a drop in the anisotropy near the edges of the duct is observed. This drop might be because of the vorticity in the boundary layer. The standard deviation along the column of respective contours is shown in Appendix I. The standard deviation does not show any outliers at Re = 4434, in the intensities or anisotropy, implying that the drop in anisotropy is not caused due to any unexpected error but might have been caused because of vorticity in the flow. This is a promising evidence that vorticity might have been captured using depolarization for the first time. For other Re cases, the variation in anisotropy is nearly constant with the deviation of 0.04 - 0.05 in the core of the duct. This is because of the errors due to the experimental setup mainly from the variation of intensity along the laser sheet. From the experiments conducted in subsection 5.2.2, the anisotropy in optical glass cuvette is in the similar range as anisotropy in the core of the glass square duct being around 0.05 for Re = 0. However, for Re = 2660, 4434 and 6208 the anisotropy r_v has dropped slightly in the entire cross-section because of increased scattering among the nanoparticles or the scattering from the PMMA shell of the nanoparticles, leading to depolarization throughout the duct.

Figure 6.8f shows the variation of horizontally polarized laser anisotropy. This is below 0.02 and shows a similar variation for all the Re. This means that the experimental setup is not sensitive to capture the variation of r_h because of the vorticity. Due to this reason, the optimization model could not be based on the anisotropy r_v, r_h.

Since the experimental noise level from the setup should be the same irrespective of Re, the intensities for Re = 4434 and Re = 0 are subtracted to remove the systematic error. This is elaborated in section 6.4.

6.4 Comparison of column-averaged intensity graphs with synthetic signals obtained from DNS

Since this thesis is based on estimating vorticity from the optimization model as shown in Figure 3.4, it is important to show the differences between the synthetic signals obtained from DNS and the experimental results. This is the final objective of approach 2 (green arrows) as marked in the purple box in Figure 1.1. To compare this, filtering technique discussed in Figure 4.8 is used here.

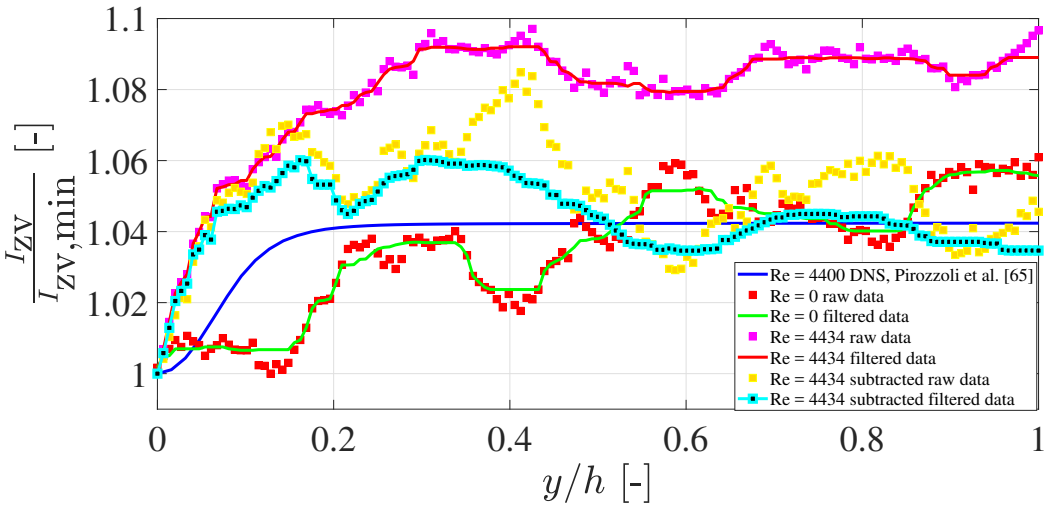

(a) Variation of column averaged normalized intensity I_{zv} at Re = 4434.

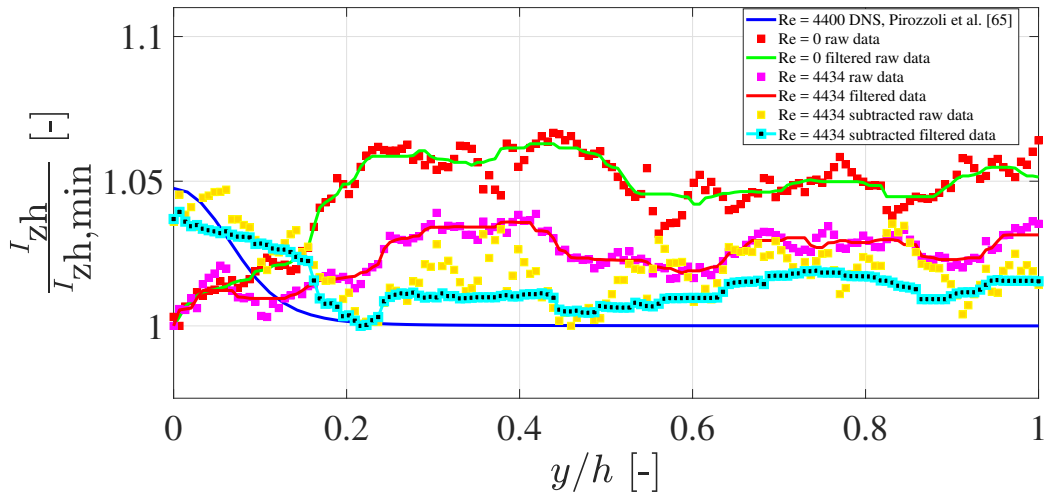

(b) Variation of column averaged normalized intensity I_{zh} at Re = 4434.

Fig. 6.9 Variation of normalized column averaged intensities I_{zv} and I_{zh} for Re = 0 and 4434 along the half width of the square duct. Both the plots show variation for different cases as shown in the legend. Starting with synthetic signal obtained from normalized Figure 6.1 from DNS [67]. "Raw data" for both the Re is shown. "Filtered data" using median filtering is shown for both the Re. "Re = 4434 subtracted" means, that normalized intensity at Re = 0 is subtracted from Re = 4434 to remove the common inaccuracies present in both Re = 0 and Re = 4434. Accordingly both the "subtracted raw and the filtered data" is shown.

Figure 6.9a shows the comparison plot of column averaged signal I_{zv}, Figure 6.9b shows the comparison plot of column averaged signal I_{zh}, Figure 6.10a shows the comparison plot of column averaged signal I_{yv} and Figure 6.10b shows the comparison plot of column averaged signal I_{yh}. Since the synthetic signals cannot be compared directly to the experimental results due to the magnification factor I_0, all of them are normalized with their respective minimum values. The respective signals are compared with the column averaged synthetic signals obtained from the DNS [67] as shown in Figure 6.1.

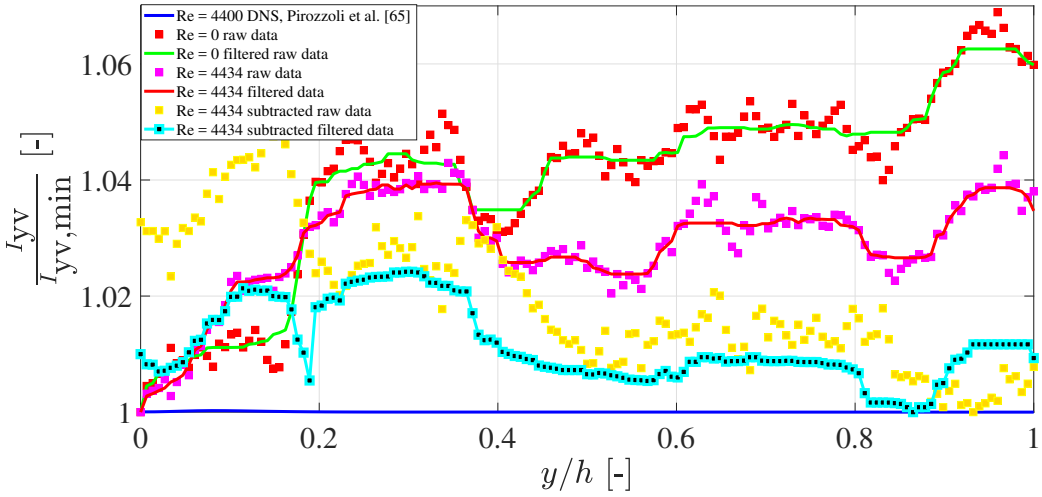

(a) Variation of column averaged normalized intensity I_{yv} at Re = 4434.

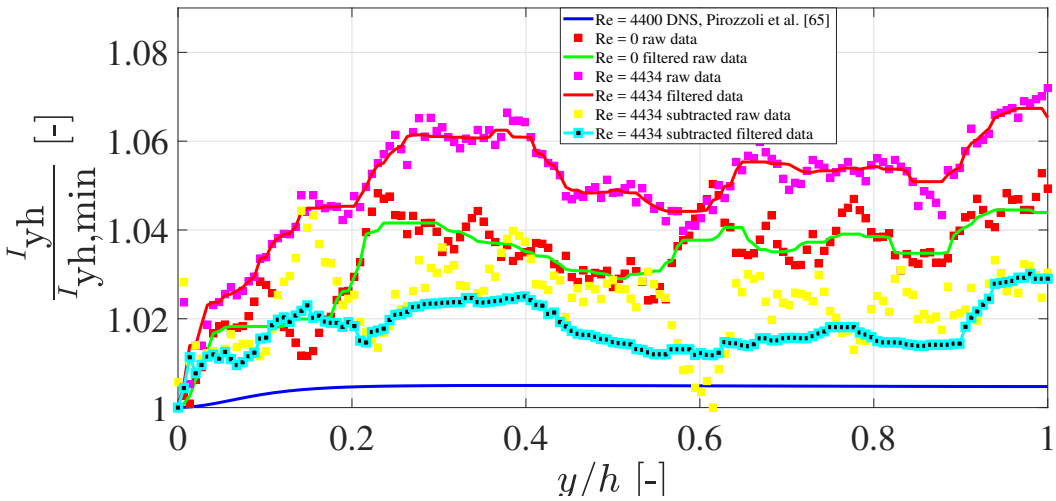

(b) Variation of column averaged normalized intensity I_{yh} at Re = 4434.

Fig. 6.10 Variation of normalized column-averaged intensities I_{yv} and I_{yh} for Re = 0 and 4434 along the half width of the square duct. Both the plots show variation for different cases as shown in the legend. Starting with synthetic signal obtained from normalized Figure 6.1 from DNS [67]. "Raw data" for both the Re is shown. "Filtered data" using median filtering is shown for both the Re. "Re = 4434 subtracted" means, that normalized intensity at Re = 0 is subtracted from Re = 4434 to remove the common inaccuracies present in both Re = 0 and Re = 4434. Accordingly both the "subtracted raw and the filtered data" is shown.

The legend in the figures Figure 6.9 and Figure 6.10 is explained here. "Re = 0 raw data" is the column averaged intensity signal of the image Figure 6.6b. "Re = 0 filtered data" is the median filtered column-averaged intensity signal of the image Figure 6.6b. "Re = 4434 raw data" is the column-averaged intensity signal of the image Figure 6.6a. "Re = 4434 filtered data" is the median filtered column-averaged intensity signal of the image Figure 6.6a. "Re = 4434 subtracted raw data" is obtained by following the algorithm as shown in Figure 4.8 and respectively its median filtered signal is Re = 4434 subtracted filtered data. The raw data for Re = 4434 and Re = 0 is also compared with other Re as shown in Figure 6.8a.
Figure 6.9a shows a similar trend for "Re = 4434 subtracted filtered data" and the "DNS synthetic signal". Roughly for y/h = 0-0.2, a rise in the normalized intensity is observed with an increasing deviation. From 0.2 - 1, its the noise level from the experimental setup. This means that the respective trend in the increase in intensity I_{zv} can be observed pixel by pixel if the noise level from the experimental setup is low. Figure 6.9b shows a similar decreasing trend for "Re = 4434 subtracted filtered data" as the "DNS synthetic signal" for y/h = 0-0.2. Figure 6.10a gives a rough idea about the noise levels in the experimental setup. The synthetic signals obtained from DNS is equal to 1 throughout the cross-section with a small change in intensity in the corners of the cross-section. However, the subtracted filtered data shows a clear deviation throughout the cross-section by a margin of 2%. This implies that because of the random error from the experimental setup, there is a deviation between experimental and DNS results. Although the contours are column averaged, the random error could not be removed. Lastly, Figure 6.10b shows an average deviation of 2% which is again because of the random error.
The normalized intensity is not following the trend of DNS in the boundary layer due to several reasons. The laser sheet thickness is around 0.5 mm. The results obtained from the experiments are spatially averaged over a width of 0.5 mm. Vortex stretching can also be the reason for the deviation concerning the DNS signal. The noise level from the experimental setup will have some share in the deviation of the DNS from experimental results, although the Re = 0 case is subtracted. Random error from the fluctuations of the laser intensity due to change in the laser frequency can also affect the deviation. Since two laser heads were used with a trigger box, this can also cause the deviation in the intensity. Although fresh nanoparticles were used, a small effect of photobleaching can also add to the error in the technique. Since the variation in intensity is primarily near the edges of the duct, laser attenuation and laser scattering can affect the respective polarized emissions. Systematic errors were removed by subtracting flow and no flow intensity signals. However, the random error from the setup was roughly quantified as around 2% in the column-averaged signals.
Based on this analysis, the filtered intensities were chosen as input parameters for the optimization algorithm as described in Equation 3.21. This is elaborated in section 6.5.

6.5 Estimation of vorticity using the optimization model

In this section, the filtered and subtracted intensities from the previous section is used as the input parameters of the optimization model shown in Equation 3.21. This is the final step of approach 1 discussed initially in Figure 1.1 marked in purple box. To estimate the vorticity, it is important to understand the variation of ratios of input parameters along the width of the square duct. Figure 6.11 shows the variation of column-averaged intensity ratios at Re = 4434 along the width of the square duct. This is compared with the ratio of synthetic signals computed from the DNS data at Re = 4400 [67]. Figure 6.11a shows the variation of the ratio $\frac{I_{zv}}{I_{zh}}$ along the width of the square duct. Figure 6.11b shows the variation of the ratio $\frac{I_{yh}}{I_{yv}}$ along the width of the square duct.

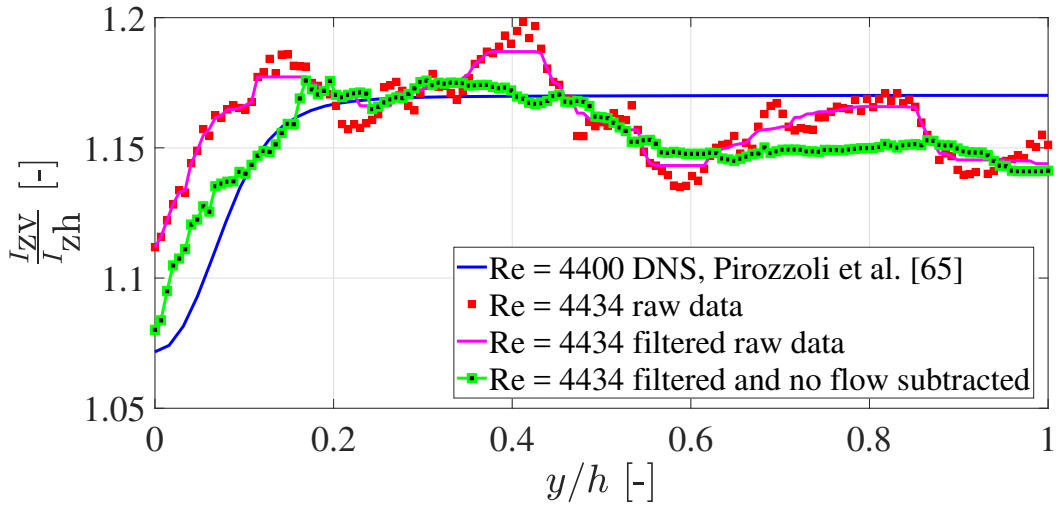

(a) Variation of the intensity ratio $\frac{I_{zv}}{I_{zh}}$ along the half width of the square duct.

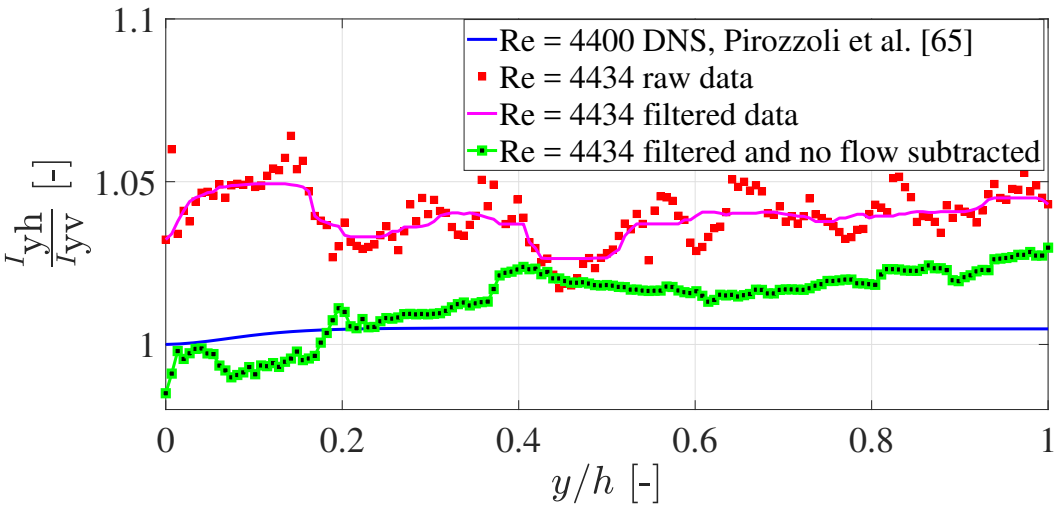

(b) Variation of the intensity ratio $\frac{I_{yh}}{I_{yv}}$ along the half width of the square duct.

Fig. 6.11 Variation of ratios of $\frac{I_{zv}}{I_{zh}}$ and $\frac{I_{yv}}{I_{yh}}$ at Re = 4434 along the half width of the square duct, which are the input parameters for the optimization model as shown in Figure 3.4. The legend shows the ratio of synthetic signals (Appendix D) computed from the DNS vorticity data [67]. "Raw data" and median "filtered data" is shown for Re = 4434. Finally, the "Re = 4434 filtered and no flow subtracted" means using the median filter and the intensity signals Re = 0 case (no flow condition) is subtracted to remove similar inaccuracies in both Re = 4434 and Re = 0 cases.

The legend shows the column-averaged ratio of synthetic signals as plotted in Figure 6.1. The ratio of respective intensities were computed to study their variation along the width of the square duct. Raw and median filtered data were also plotted. Finally, the filtered and no flow subtracted data removing the common inaccuracies from Re = 0 no flow condition is shown. Comparing the ratio of the synthetic signals, for the highest accuracy of vorticity results these two curves should overlap. A respective rise in the trends is observed from the edges but the slope of the curves is different.

The deviation between the synthetic signals and the experimental results is because of random error from the

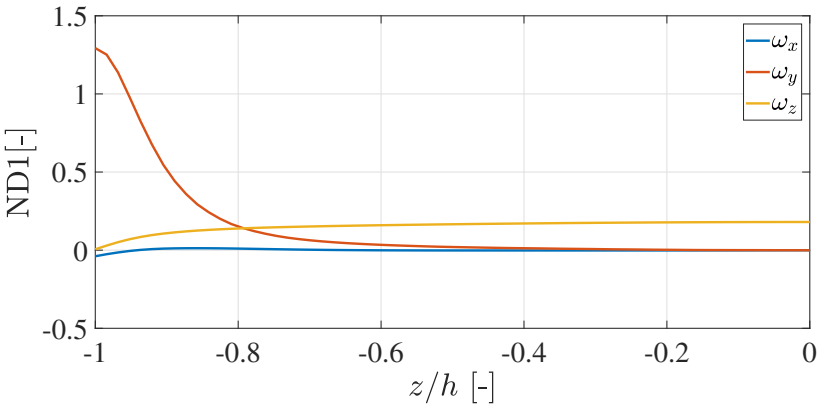

Fig. 6.12 This graph shows the variation of the introduced non-dimensional number ND1 (Equation 3.26) with the individual vorticity components ω_x, ω_y and ω_z. This plot shows that as z/h increases, the value of ND1 reduces which implies that the sensitivity of the measurement technique is reducing as described in section 3.5.

experiments. The deviation in the individual signals because of random error causes the deviation in the ratio of the signals. The difference between the maximum and minimum in the synthetic DNS signal in Figure 6.11a is around 0.07 but the difference between the maximum and minimum in Figure 6.11b is less than 0.02. So based on this, the ratio of I_{yh} and I_{yv} obtained from the experimental results cannot be trusted because of the magnitude of the random error is same as the magnitude of the expected ratio from the synthetic signals. Hence, this is a limitation that needs to be solved for the future. Using these ratios as the input parameters in the Equation 3.21, vorticity was estimated.

Before addressing that, since the coordinate system used to derive the correlations are in the spherical coordinate system, it is important to translate that coordinate system into the DNS coordinate system as shown earlier in Figure 6.2 for comparison. In subsection 3.5.3, the effect of ND1 on the sensitivity of the experiments was discussed. Figure 6.12 shows the variation of ND1 along the the half width of the square duct. The value of ND1 for ω_x and ω_z is less than 0.2. This means that with the sensitivity of the europium nanoparticles, column averaged ω_x and ω_z cannot be computed. ω_x cannot be computed with europium nanoparticles because the ND1 for maximum ω_x is less than 0.2 making it insensitive. Technically ω_z could be computed since it is of the same magnitude as ω_y but along a different plane. However, since the results discussed here are column averaged, the magnitude of ω_z reduces leading to lower ND1. If the noise level along the laser sheet would be lower, definitely ω_z could be computed with this technique. Currently, ω_z is not optimized from the optimization algorithm, hence ω_z comparison is not shown here.

For ω_y, the value of ND1 reduces from 1.3 to 0 as z/h increases from 0 to 1. This means that the sensitivity of the experiments reduces as z/h increases along the half width of the square duct. So, for z/h between 0 and 0.2, the vorticity ω_y could be computed by this technique. Figure 6.13 shows the comparison of column averaged vorticity ω_y for half width of the square duct. The plot shows "raw experimental data", "filtered subtracted experimental data", "DNS data [67]" and "synthetic signal output". "Filtered subtracted experimental data" means, the systematic error was removed from the Re = 4434 conditions, using no-flow conditions. "Synthetic signal output" means that when the derived synthetic signals (Figure 6.1) were used as user input in the optimization algorithm Equation 3.21, the obtained vorticity ω_y is plotted in purple line. The initial guess for vorticity is a zero vector (0,0,0) in the optimization algorithm.

Many observations can be made here. Firstly, the accuracy of the optimization algorithm can be observed here. The difference between the DNS vorticity and the vorticity from the synthetic signals shows the accuracy of the optimization algorithm. This shows that the optimization algorithm is not completely optimized which can be further improved. Since the optimization problem is not completely optimized, the deviation between the experimental and DNS results of ω_y cannot be attributed to have occurred solely due to the deviation of ratio of intensities Figure 6.11. Secondly, the unfiltered experimental data follows the trend near the edges though the vorticity for z/h = 0.2-1 shows the difference between experimental and the DNS results that are caused due to the random error from the measurements. The filtered experimental data shows the vorticity following a similar trend as the DNS data.

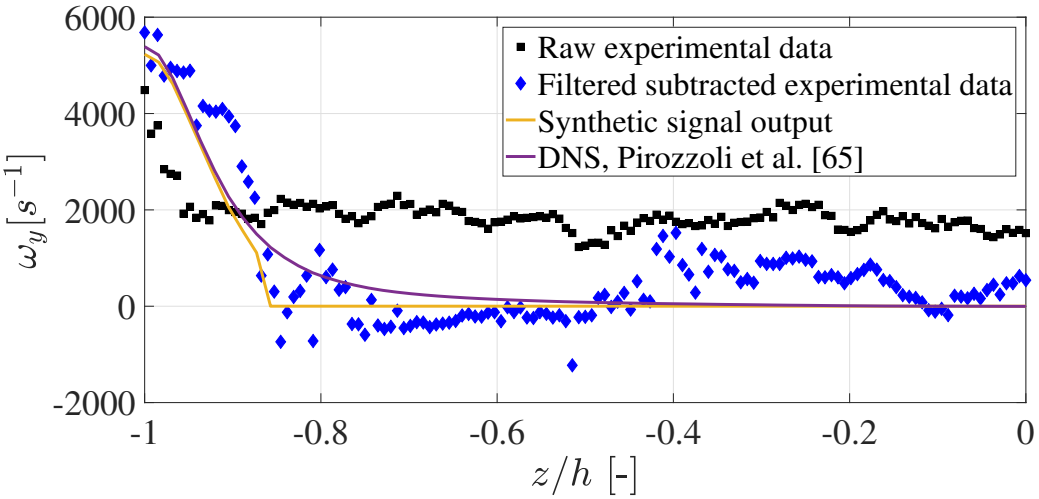

Fig. 6.13 The above plot shows the variation of column averaged vorticity ω_y along the half width of the square duct. It shows the comparison of DNS data [67] with both "filtered subtracted experimental data" and "raw experimental data". The legend "synthetic signal output" is the plot when the actual vorticity results from DNS is used in Appendix D and again these synthetic signals D_{zv}, D_{zh}, D_{yv} and D_{yh} are used as input parameters in the optimization model Equation 3.21. Ideally the DNS and the "synthetic signal output" should overlap when the optimization algorithm is completely optimized.

This trend in the vorticity drop is a promising evidence that, if the random noise from the measurement equipment can be reduced then the accuracy of the estimated vorticity can improve. The deviation in the ratios of intensities as plotted in Figure 6.11 cannot be assumed to be the only reason for the deviation in the estimated vorticity, because the algorithm should be further optimized. This can reduce or increase the difference between the estimated vorticity and the DNS data. However, the deviation between the raw and filtered data in Figure 6.11b after y/h = 0.2 to 1 is one of the main reasons for deviation between raw and filtered vorticity data after z/h = 0.2 to 1. So, a 1% increase in the ratio of intensity $\frac{I_{yh}}{I_{yv}}$ will cause a deviation of vorticity by approximately 1000 s^{-1}. This means that the optimization algorithm is highly sensitive to the input parameters especially in the regions where ND1 is close to zero.
Since the whole post-processing was performed with column averages, i.e, the intensity is averaged along the $z-$ axis in experimental coordinate system (Figure 6.2), pixel by pixel vorticity contour is beyond the scope of this thesis. For better understanding, Figure 6.14 shows the ω_y contour from both the DNS [67] at Re = 4400 and the experimental results at Re = 4434. Figure 6.14a shows the vorticity contour plotted from the results "Filtered experimental data" in Figure 6.13. Ideally, from the algorithm it should be possible to estimate all the

three vorticity components with a single field of view. However due to the random error and a low ND1, ω_z and ω_y cannot be computed using the setup section 4.1.
Since this is a first attempt to estimate vorticity like this, it is important to perform repeatability studies as described in section 6.6 for a better understanding.

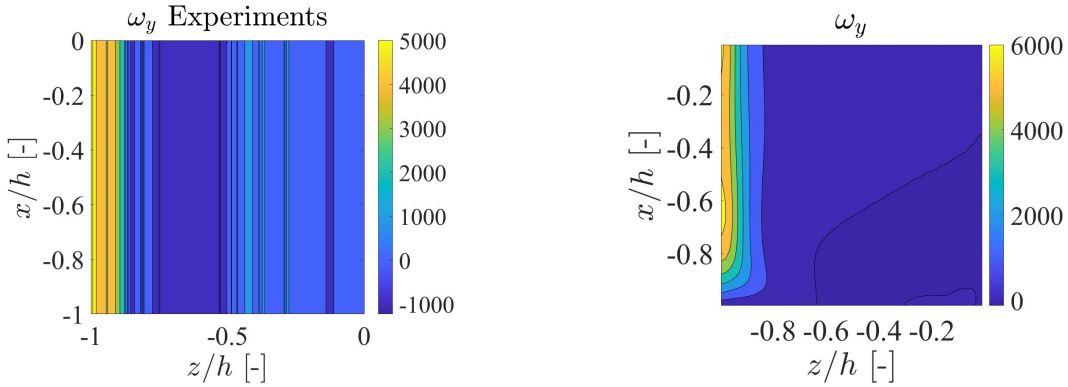

Fig. 6.14 The two contours show the mean vorticity ω_y for a single quadrant of the square duct. Fig (a) shows the averaged vorticity contour that was plotted in Figure 6.13 as "Filtered experimental data" at Re = 4434. Fig (b) shows the DNS data from Pirozzoli et al. [67] at Re = 4400.

6.6 Repeatability studies

In this section, repeatability studies were conducted for Re = 4434. Figure 6.15 shows the variation of column-averaged ω_y for three different trials along with the DNS data for the half-width of the square duct. Three observations can be made here. The estimated vorticity from the three trials do not overlap because of the random error. The trend in the vorticity can be observed which means that the vorticity can be estimated by this technique if the accuracy of the results is improved by reducing the random error. This is a promising factor for this measurement technique which shows the proof of concept of underlying physics. Secondly, the deviation between the DNS and the three trials is also because of the error from the optimization model. Thirdly, it should also be considered that for lower random error, the difference between the DNS and the experimental results can increase or reduce because its magnitude cannot be quantified. The anisotropy drop for the three trials is shown in Figure 6.15. Figure 6.15e shows the comparison of DNS vorticity and experimental results in terms of percentage. It can be observed that the relative error increases slowly from the edge and high values of relative error indicate that the sensitivity of the optimization algorithm is considerably high towards the random error in the experiments. For the regions of z/h between -1 to -0.8, where ND1 is close to 1 from Figure 3.6a, this methodology should work. However, due to random fluctuations, the error in the vorticity results is higher than 25%.
Further experiments were not conducted for Re between 2660 and 6208 because similar trends could be expected in the ω_y, however, nothing can be discussed regarding the accuracy of the vorticity results at this stage of the experimental technique, since the repeatability of vorticity is not accurate.

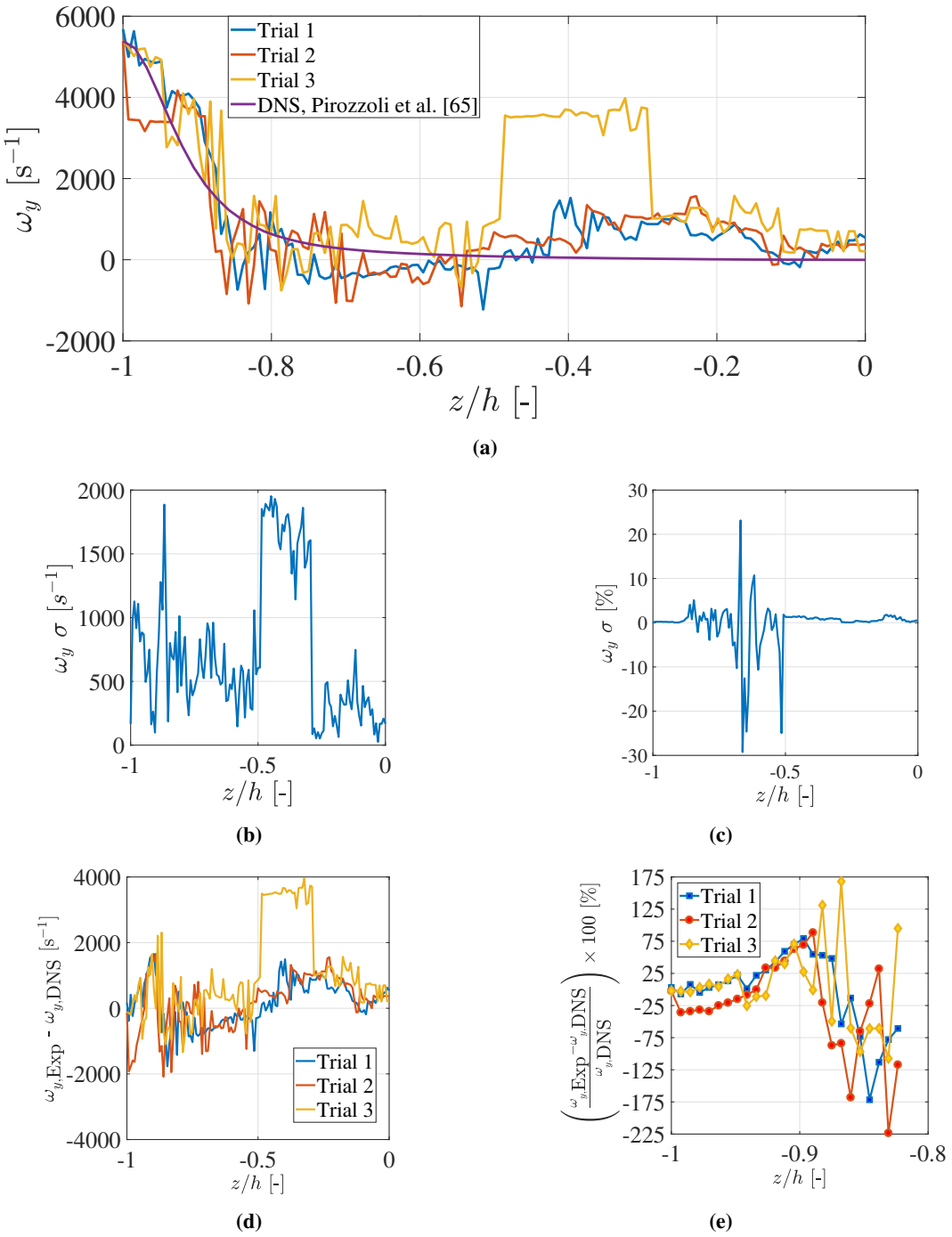

Fig. 6.15 The above figures shows the repeatability studies that were conducted to show the estimation of vorticity for three trial cases at Re = 4434 for half width of the square duct. Fig (a) shows the similar trend in vorticity as the DNS data near the edges of the duct in the range from z/h from -1 to -0.8, where ND1 is in the sensitivity range as shown in Figure 6.12. Fig (b) and Fig (c) shows the standard deviation among the three trials in [s^{-1}] and in [%] when they are normalized by mean of the three trials. Fig (d) and Fig (e) compares the experimental and DNS results for the three trials.

Chapter 7

Conclusion and Recommendations

"The beauty of research is that you never know where it's going to lead "

Richard Roberts

In this work, a completely different perspective to estimate vorticity using depolarization is presented. A proof of concept for the optical technique was developed to measure vorticity indirectly using phosphorescence depolarization of the nanoparticles and the results were further compared with DNS data. The current chapter will provide the main conclusions that were drawn from the results of this work and answer to the research questions raised in chapter 1. Further recommendations are also provided for improving this technique for the future.

7.1 Conclusion

In the guide to this thesis, many research questions were raised which directed the progress of this project. The following subsections will each repeat the raised sub-goals of this thesis and answer the particular research question. An additional comments sub-section is included which is very important for future researchers working on the development of this technique to follow.

7.1.1 Theory behind the technique

The theory behind this measurement technique that was developed inhouse, is not established or published previously, hence an elaborate description is provided in section 3.3. The optimization problem used to translate the intensities to the vorticity was presented in section 3.4. A detailed formulation of the problem was established using two additional nondimensional numbers ND1 and ND2 (subsection 3.5.3) to address the underlying physics and for future researchers to improve this technique. A list of assumptions was listed which helped in the simplification of the problem statement.

7.1.2 Preliminary experiments to understand the objectives

Since this is a completely new approach without any background literature on how to proceed, it was important to conduct the preliminary experiments to interpret the results in the turbulent duct flow. Lifetime measurements

and spectroscopic analysis of different nanoparticles were conducted to select the right nanoparticles with higher lifetimes and the experimental setup. Photobleaching studies were conducted to estimate its effect on the results of turbulent duct flow measurements.
For building or understanding an experimental setup based on a new concept without any rule book, it was important to follow the approach based on first principles. Initially, the excitation polarization and emission polarization was calibrated with laser power meters and colloidal silica respectively in subsection 5.2.1. The anisotropy of the nanoparticles was measured in fixed $r_0 = 0.12$ and quiescent state of flow $r = 0.05$ to estimate the drop in polarization due to rotational diffusion in subsection 5.2.2. Effect of viscosity on anisotropy was conducted to show the applicability of these nanoparticles as optical viscosity probes as shown in Figure 5.6. Effect of viscosity on the phosphorescence quantum yield was analyzed which gives a clear idea about using different fluid media to increase the phosphorescence quantum yield in vorticity estimation measurements Figure 5.7. The effect of filtering and concentration of the nanoparticles was studied which helped in reducing the scattering of light by choosing the optimum concentration of nanoparticles. These experiments laid out the guidelines for conducting this technique for future researchers.

7.1.3 Turbulent duct flow measurements

The results from chapter 6 show some of the promising evidenced that can be used in the future to improve accuracy. The section 6.1 shows the variation of the synthetic signals that were derived from the analytical formulae (Appendix D) with different input parameters. The threshold limits of non-dimensional number ND2 (Equation 3.27), depending on the Re were shown which decides the sensitivity of the experimental setup. The section 6.2 shows the contours of I_{zv}, I_{zh}, I_{yh} and I_{yv} from the experiments. A drop in the anisotropy was observed near the edges of the contour that may have been caused due to the vorticity. The average intensity of I_{zv} is higher than the other intensities which is similar to the synthetic signals.
Column-averaged signals were analyzed and the systematic noise was removed from the Re = 4434 condition. In Figure 6.8, the drop in anisotropy, a different trend for the intensities I_{zv} and I_{zh} were observed at Re = 4434 compared to Re = 0, 2660 and 6208. To show the proof of concept, the methodology shown in Figure 1.1 was followed. The end objective of approach 2 was shown in section 6.4. Figure 6.9 showed a similar trend of normalized synthetic signals with subtracted filtered experimental data for the intensities I_{zv} and I_{zh}. Figure 6.10 showed no similar trends for intensities I_{yv} and I_{yh} because of similar magnitudes of the random error and the expected intensity.
Finally, the objective of the approach 1 Figure 1.1 is presented in section 6.5. The input parameters in the optimization algorithm were compared with the ratio of the synthetic signals showing a very similar trend with a slight deviation in measurements because of the random error as shown in Figure 6.11. The variation of column averaged ND1 for different components of vorticity showed the trend in the sensitivity of this technique along the width of the square duct Figure 6.12. Lastly, the vorticity ω_y computed from the optimization algorithm showed a similar trend compared to the DNS data as shown in Figure 6.13. This is a promising evidence for further improvement of this technique by reducing the measurement error and improving the optimization algorithm. Repeatability studies were also conducted that showed very similar trends in the ω_y, as shown in Figure 6.15. The estimated vorticity for three trials did not overlap because of the measurement error from the measurement. However, the percentage in the error or the accuracy of the estimated vorticity from this technique cannot be discussed at this stage because of cumulative error from multiple sources of the experiment and the error present in the optimization of the optimization algorithm.

7.1.4 Additional comments

Very low fundamental anisotropy r_0 from the europium nanoparticles was unexpected in this thesis due to a lack of previous literature. These particles had to show higher sensitivity to the polar excitation and longer lifetimes which made the particles per se unique for this problem statement. However, the rest of the thesis was progressed considering this limitation on the table.
The ratio of the width of the turbulent duct thickness to the laser sheet thickness is around 8 which makes it very difficult to estimate the vorticity accurately. This also limits the highest Re for which measurements can be conducted due to the smaller width of the boundary layer. Since the problem statement required a canonical flow with considerable previous research and to avoid any depolarization of the excitation source, flow in a flat surface glass square duct was chosen.

7.1.5 Main conclusion

All the sub-goals which were undertaken during the initial phase of the project was completed and described in the earlier chapters. From the conclusions of the previous chapter, the author feels that the experiment can be improved in the coming future with equipment to estimate vorticity as a contour. The trend in the estimated vorticity ω_y, the repeatability studies, the drop in the anisotropy near the edges of the square duct, similarity of experimental and synthetic signals and the expected sensitivity of ND1 all these indicate as the promising evidence of the proposed hypothesis of the underlying physics. If the accuracy is improved, this technique has the potential to estimate all the three components of vorticity with a single field of view. Since this is the first attempt that involves the formulation of this problem statement and attempting to explore this uncharted physics, there is a lot of room for improvement which is described in section 7.2.

7.2 Future Recommendations

The main idea of developing this measurement technique is to compute the vorticity efficiently by observing the depolarization. Since this is the first-ever attempt in measuring vorticity using depolarization, there can be several improvements and recommendations which can be adhered to, for understanding the underlying physics.

- Steady-state measurements were conducted in this technique. However, for more accurate results, a single-shot transient imaging technique can improve the accuracy of the depolarization caused due to the vorticity.
- This measurement technique employed a UV laser to excite lanthanide-based europium particles. To scale this technique, it is useful to find particles that have phosphorescence spectra in visible wavelength range that also shows sensitivity towards polarized excitation.
- The europium or terbium based particles that have a lifetime of the order of milliseconds show limited sensitivity towards polarized excitation. If the particles can be synthesized using chemical techniques that show higher sensitivity towards polarized excitation and have lifetimes of the order similar to lowest vorticity time-scales, this technique can be improved successfully.
- To improve this technique, the experimental equipment should be tailored to the laser wavelength and the square duct dimensions. The laser sheet optics used in this thesis show attenuation of the UV laser beam

with 0.5 mm laser sheet thickness. It should be replaced with UV laser sheet optics. Smaller laser sheet thickness should be used to improve the resolution of this method.

- All the measurements conducted here were using the laser sheet along the duct flow, which is oriented in the vertical direction. In this thesis, the author has not conducted experiments on the horizontal flow. This technique should be applied to the horizontal duct flow with the laser sheet perpendicular to the flow for further validation of the results.
- The optimization model which is being developed inhouse at ETH, is still under development. This should become generic and applicable to all the fluid flow problems. In this thesis, due to time constraints, only duct flow is studied. However, to improve the algorithm and verify this optical technique, other fluid flow problems must be studied using this technique to check its versatility.
- This technique can be further combined with LIF using the same particles to measure temperature fields and the vorticity simultaneously.
- The emission from the europium particles comes in contact with 3 filters and a polarizer. These four components will affect the emission side quantum yield and reduce the quantum yield detected by the camera. To improve this, polarizer band-pass filters can be used in the future to reduce unwanted attenuation due to experimental equipment.
- The laser beam shows fluctuation which affects the accuracy of the results from this technique. However, a UV laser power meter can be used to further optimize the laser output or perform experiments with continuous constant power output laser beam to improve this technique.
- The shape of the nanoparticles have to be verified using a Scanning Electron Microscope (SEM).
- The objective of this thesis was to use inexpensive equipment to measure vorticity directly. However, after using 4 types of luminescent particles, 3 types of laser and 2 cameras, this combination has worked due to low phosphorescence quantum yield. If phosphorescent particles with higher lifetimes and higher quantum yield which are sensitive to polarized excitation are synthesized then cheaper experimental equipment using laser in the visible radiation and the setup in section F.2 could be used.
- To calibrate polarization measurements, colloidal silica is used which shows 100% scattering and anisotropy of the sample (ideally, $r = 1$). Colloidal silica also shows fluorescence in the UV excitation which is a disadvantage ($r = 0.2$) during calibration of this setup. The author has successfully calibrated to his knowledge by considering the laser as 100 % vertically polarized. This can be improved if a 100% scattering sample in UV radiation is employed to fix the calibration angles of the emission side.
- No particular image processing algorithm was used in this thesis to improve the resolution of the results since the focus was to compare the accuracy of the raw data. To further improve this technique, possibly advanced image processing algorithms can be combined with deep learning techniques in the future.
- A rectangular square duct was used since spherical surfaces depolarizes the laser beam before exciting the particles. To overcome this, the pipe can be designed using a rectangular outer surface which reduces the depolarization and by experimentation, the depolarization factor can be computed which could be used as a correction factor in the optimization vorticity algorithm.

- Particle plastic interaction is not taken into account in the micro-scale. When the particles emit light, it can get scattered due to the plastic surface from the other particles. This is not taken into account in this thesis, however, it was minimized by ensuring the minimum concentration of the sample.
- Different types of flow have to be studied to strongly conclude the hypothesis. Wake of a cylinder or a sphere can be a good starting point. However, it is recommended that once the measurement error is fixed and the optimization algorithm is completely optimized then other flows should be studied.
- Since these measurements were conducted with long exposure at the cost of accuracy, if the equipment cost is further reduced then it is possible to develop a device like a thermal camera which can estimate vorticity.

References

[1] Adrian, R. and Westerweel, J. (2010). *Particle Image Velocimetry*. Cambridge University Press.

[2] Adrian, R. J. (1986). Image shifting technique to resolve directional ambiguity in double-pulsed velocimetry. *Appl. Opt.*, 25(21):3855–3858.

[3] Adrian, R. J. (1991). Particle-imaging techniques for experimental fluid mechanics. *Annual Review of Fluid Mechanics*, 23(1):261–304.

[4] Agui, J. H. and Andreopoulos, Y. (2003). A new laser vorticity probe — lavor: Its development and validation in a turbulent boundary layer. *Experiments in Fluids*, 34(2):192–205.

[5] Allen, J., Shockling, M., and Smits, A. (2004). Effects of surface roughness on high reynolds number turbulent pipe flow.

[6] Ameloot, M., vandeVen, M., Ulises Acuña, A., and Valeur, B. (2013). Fluorescence anisotropy measurements in solution: Methods and reference materials (iupac technical report). *Pure and Applied Chemistry*, 85.

[7] Barnhart, D. H., Adrian, R. J., and Papen, G. C. (1994). Phase-conjugate holographic system for high-resolution particle-image velocimetry. *Appl. Opt.*, 33(30):7159–7170.

[8] Bassani, F. (1989). Luminescence: General concepts and applications to the study of solids. In Jameson, D. M. and Reinhart, G. D., editors, *Fluorescent Biomolecules*, pages 1–16, Boston, MA. Springer US.

[9] Bertoluzza, A., Fagnano, C., Morelli, M. A., Guglielmi, M., Scarinci, G., and Maliavski, N. (1988). Raman spectra of SiO 2 gel glasses prepared from alkoxide, colloidal and amine silicate solutions. *Journal of Raman Spectroscopy*, 19(4):297–300.

[10] Bertz, A., Ehlers, J.-E., Wöhl-Bruhn, S., Bunjes, H., Gericke, K.-H., and Menzel, H. (2013). Mobility of Green Fluorescent Protein in Hydrogel-Based Drug-Delivery Systems Studied by Anisotropy and Fluorescence Recovery After Photobleaching. *Macromolecular Bioscience*, 13(2):215–226.

[11] Bian, X., Kim, C., and Karniadakis, G. E. (2016). 111 years of brownian motion. *Soft Matter*, 12:6331–6346.

[12] Biotechnology, S. (2019). Pt(ii) meso-tetra(pentafluorophenyl)porphine (cas 109781-47-7).

[13] Brundrett, E. and Baines, W. D. (1964). The production and diffusion of vorticity in duct flow. *Journal of Fluid Mechanics*, 19(03):375–394.

[14] Bui, A. T., Grichine, A., Duperray, A., Lidon, P., Ois, F., Riobe, R., Andraud, C., and Maury, O. (2017). Correction to "Terbium(iii) Luminescent Complexes as Millisecond-Scale Viscosity Probes for Lifetime Imaging". *J. Am. Chem. Soc*, 139:7693–7696.

[15] Crimaldi, J. P. (2008). Planar laser induced fluorescence in aqueous flows. *Experiments in Fluids*, 44(6):851–863.

[16] Davis, R. V., Govoni, D. E., and Fehr, M. J. (2010). Room temperature phosphorescence apparatus and methods, us7772009b2.

[17] Deželić, G. and Kratohvil, J. P. (1960). Determination of size of small particles by light scattering. experiments on ludox colloidal silica. *Kolloid-Zeitschrift*, 173(1):38–48.

[18] Dolatabadi, N., Rahmani, R., Rahnejat, H., and Garner, C. (2019). Thermal conductivity and molecular heat transport of nanofluids. *RSC Advances*, 9:2516.

[19] Elsinga, G. E. (2008). *Tomographic Particle Image Velocimetry and its application to turbulent boundary layers*. PhD thesis.

[20] Faucon, J. and Lakowicz, J. (1987). Anisotropy decay of diphenylhexatriene in melittin-phospholipid complexes by multifrequency phase-modulation fluorometry. *Archives of Biochemistry and Biophysics*, 252(1):245 – 258.

[21] Frish, M. B. and Webb, W. W. (1981). Direct measurement of vorticity by optical probe. *Journal of Fluid Mechanics*, 107:173–200.

[22] G. Zhegalova, N., Aydt, A., T. Wang, S., and Berezin, M. (2013). Molecular thermometers for potential applications in thermal ablation procedures. *Proc. SPIE*, 8596.

[23] Gabor, D. (1948). A New Microscopic Principle. *Nature*, 161:777–778.

[24] Griffiths, D. J. and Schroeter, D. F. (2018). *Introduction to Quantum Mechanics*. Cambridge University Press, 3 edition.

[25] Hori, T. and Sakakibara, J. (2004). High-speed scanning stereoscopic PIV for 3D vorticity measurement in liquids. *Measurement Science and Technology*, 15:1067–1078.

[26] Kastrinakis, E. G. (1976). *An experimental investigation of the fluctuations of the streamwise components of the velocity and vorticity vectors in a fully developed turbulent channel flow*. PhD thesis.

[27] Kenkre, V. M., Tokmakoff, A., and Fayer, M. D. (1994). Theory of vibrational relaxation of polyatomic molecules in liquids. *The Journal of Chemical Physics*, 101(12):10618–10629.

[28] Kenyon, A. J., Mccaffery, A. J., and Quintella, C. M. (1991a). Fluorescence depolarization as a probe of molecular dynamics within liquid jets. *Molecular Physics*, 72(4):965–970.

[29] Kenyon, A. J., Mccaffery, A. J., Quintella, C. M., and Winkel, J. F. (1991b). A study of molecular dynamics within liquid flows using fluorescence depolarization. *Molecular Physics*, 74(4):871–884.

[30] Kim, J., Moin, P., and Moser, R. (1987). Turbulence statistics in fully developed channel flow at low Reynolds number. *Journal of Fluid Mechanics*, 177:133–166.

[31] Kim, J. H. and Fiedler, H. E. (1989). Vorticity measurements in a turbulent mixing layer. In Fernholz, H.-H. and Fiedler, H. E., editors, *Advances in Turbulence 2*, pages 267–271, Berlin, Heidelberg. Springer Berlin Heidelberg.

[32] Kock am Brink, B. and Foss, J. (1993). chapter Enhanced mixing via geometric manipulation of a splitter plate. Shear Flow Conference. American Institute of Aeronautics and Astronautics.

[33] Kovasznay, G. S. L. (1954). High speed aerodynamics and jet propulsion. *Princeton University press*, 9:213–285.

[34] Kuijt, J., Ariese, F., Brinkman, U., and Gooijer, C. (2003). Room temperature phosphorescence in the liquid state as a tool in analytical chemistry. *Analytica Chimica Acta*, 488(2):135–171.

[35] Kundu, P. K., Cohen, I. M., and Dowling, D. R., editors (2012). *Vorticity Dynamics, Chapter 5*. Academic Press, Boston, fifth edition.

[36] Kuznetsov, V. A., Kunavin, N. I., and Shamraev, V. N. (1974). Spectra and quantum yield of phosphorescence of rhodamine 6g solutions at 77^0 k. *Journal of Applied Spectroscopy*, 20:604–607.

[37] Lab261 (2019). Nanospheres,luminescent.

[38] Lakowicz, J. R., editor (2006a). *Fluorescence Anisotropy*, pages 353–382. Springer US, Boston, MA.

[39] Lakowicz, J. R., editor (2006b). *Instrumentation for Fluorescence Spectroscopy*, pages 27–61. Springer US, Boston, MA.

[40] Lakowicz, J. R., editor (2006c). *Introduction to Fluorescence*, pages 1–26. Springer US, Boston, MA.

[41] Lang, D. B. and Dimotakis, P. E. (1982). Measuring vorticity using the laser doppler velocimetry. *American Physical Society Bulletin*, 27.

[42] Lee, S.-C., Heo, J., Woo, H. C., Lee, J.-A., Seo, Y. H., Lee, C.-L., Kim, S., and Kwon, O.-P. (2018). Fluorescent Molecular Rotors for Viscosity Sensors. *Chemistry - A European Journal*, 24(52):13706–13718.

[43] Levitt, J. A., Chung, P.-H., Kuimova, M. K., Yahioglu, G., Wang, Y., Qu, J., and Suhling, K. (2011). Fluorescence Anisotropy of Molecular Rotors. *ChemPhysChem*, 12(3):662–672.

[44] Lindon, J. C., Tranter, G. E., and Koppenaal, D. W. (2016). *Encyclopedia of spectroscopy and spectrometry*.

[45] Luyet, B. and Gehenio, M. (1940). Life and death at low temperatures.

[46] Maeda, N., Hirota, M., and Fujita, H. (2005). Turbulent flow in a rectangular duct with a smooth-to-rough step change in surface roughness. *Energy*, 30(2):129 – 148. 3rd International Symposium on Advanced Energy Conversion Systems and Related Technologies.

[47] Maxey, M. R. and Riley, J. J. (1983). Equation of motion for a small rigid sphere in a nonuniform flow. *The Physics of Fluids*, 26(4):883–889.

[48] Meng, H., Pan, G., Pu, Y., and Woodward, S. H. (2004). Holographic particle image velocimetry: from film to digital recording. *Measurement Science and Technology*, 15(4):673–685.

[49] Miyazaki, Kagesawa, and Ikeuchi (2003). Polarization-based transparent surface modeling from two views. In *Proceedings Ninth IEEE International Conference on Computer Vision*, pages 1381–1386 vol.2. IEEE.

[50] Mo, J. (2015). *Short timescale Brownian motion and applications*. PhD thesis.

[51] Modesti, D. and Pirozzoli, S. (2016). Reynolds and Mach number effects in compressible turbulent channel flow. *International Journal of Heat and Fluid Flow*, 59:33–49.

[52] Monty, J. (2019). Developments in smooth wall turbulent duct flows.

[53] Mu, T., Chen, S., Zhang, Y., Guo, P., and Chen, H. (2015). Determining the orientation of transition moments and depolarization by fluorescence polarizing angle spectrum. *Optics Express*, 23.

[54] Natrajan, V. K. and Christensen, K. T. (2009). Structural characteristics of transition to turbulence in microscale capillaries. *Physics of Fluids*, 21(3):034104.

[55] Natrajan, V. K. and Christensen, K. T. (2010). The impact of surface roughness on flow through a rectangular microchannel from the laminar to turbulent regimes. *Microfluidics and Nanofluidics*, 9(1):95–121.

[56] Natrajan, V. K., Yamaguchi, E., and Christensen, K. T. (2007). Statistical and structural similarities between micro- and macroscale wall turbulence. *Microfluidics and Nanofluidics*, 3(1):89–100.

[57] Nieminen, T. A., Rubinsztein-Dunlop, H., Heckenberg, N., and Bishop, A. (2001). Numerical modelling of optical trapping. *Computer Physics Communications*, 142(1):468 – 471.

[58] Nieuwstadt, F. T. M., Boersma, B. J., and Westerweel, J. (2016a). *Turbulent Flows*, pages 1–7. Springer International Publishing, Cham.

[59] Nieuwstadt, F. T. M., Boersma, B. J., and Westerweel, J. (2016b). *Turbulent Flows*, pages 151–181. Springer International Publishing, Cham.

[60] Nieuwstadt, F. T. M., Boersma, B. J., and Westerweel, J. (2016c). *Turbulent Flows*, pages 87–123. Springer International Publishing, Cham.

[61] Nikuradse, J. (1930). Untersuchungen über turbulente strömungen in nicht kreisförmigen rohren. *Ingenieur-Archiv*, 1(3):306–332.

[62] Ong, L. and Wallace, J. (1995). Local isotropy of the vorticity field in a boundary layer at high reynolds number. In Benzi, R., editor, *Advances in Turbulence V*, pages 392–397, Dordrecht. Springer Netherlands.

[63] Ötügen, M. V., Su, W.-J. J., and Papadopoulos, G. (1998). A new laser-based method for strain rate and vorticity measurements. *Measurement Science and Technology*, 9(2):267–274.

[64] Park, S.-R. and Wallace, J. M. (1993). The influence of instantaneous velocity gradients on turbulence properties measured with multi-sensor hot-wire probes. *Experiments in Fluids*, 16(1):17–26.

[65] Perrin, F. (1934). Mouvement brownien d'un ellipsoide - I. Dispersion diélectrique pour des molécules ellipsoidales. *Journal de Physique et le Radium*, 5(10):497–511.

[66] Pinelli, A., Uhlmann, M., Sekimoto, A., and Kawahara, G. (2018). Reynolds number dependence of mean flow structure in square duct turbulence. *J. Fluid Mech*, 644:107–122.

[67] Pirozzoli, S., Modesti, D., Orlandi, P., and Grasso, F. (2018). Turbulence and secondary motions in square duct flow. *Journal of Fluid Mechanics*, 840:631–655.

[68] Quintella, C. M., Gonçalves, C. C., Pepe, I., Lima, A. M. V., and Musse, A. P. S. (2002). Automated system to acquire fluorescence, polarization and anisotropy maps within liquid flows. *Journal of Automated Methods and Management in Chemistry*, 24(2):31–39.

[69] Quintella, C. M., Musse, A. P. S., Gonçalves, C. C., and Mccaffery, A. J. (2003). Fluorescence depolarisation monitoring of liquid flow before and after exiting a slit nozzle. *Experiments in Fluids*, 35:41–48.

[70] Raffel, M., Willert, C. E., and Kompenhans, J. (1998). *Mathematical background of statistical PIV evaluation*, pages 61–78. Springer Berlin Heidelberg, Berlin, Heidelberg.

[71] Rahmann, S. and Canterakis, N. (2001). Reconstruction of specular surfaces using polarization imaging. In *Proceedings of the 2001 IEEE Computer Society Conference on Computer Vision and Pattern Recognition. CVPR 2001*, volume 1, pages I–I.

[72] Reichardt, H. (1938). Messungen turbulenter schwankungen. *Naturwissenschaften*, 26(24):404–408.

[73] Reifenberger, J. G., Snyder, G. E., Baym, G., and Selvin, P. R. (2003). Emission polarization of europium and terbium chelates. *The Journal of Physical Chemistry B*, 107(46):12862–12873.

[74] Roland L. Panton (2013). *Incompressibles flow*. John Wiley & Sons, Inc, fourth edi edition.

[75] Ryabtsev, A., Pouya, S., Safaripour, A., Koochesfahani, M., and Dantus, M. (2016). Fluid flow vorticity measurement using laser beams with orbital angular momentum. *Optics express*, 24(11).

[76] Santos, B. and Valeur, B., editors (2012). *Fluorescence Polarization: Emission Anisotropy*, pages 181–212. Wiley, VCH Verlag GmbH.

[77] Sato, T., Hamada, Y., Sumikawa, M., Araki, S., and Yamamoto, H. (2014). Solubility of oxygen in organic solvents and calculation of the hansen solubility parameters of oxygen. *Industrial & Engineering Chemistry Research*, 53(49):19331–19337.

[78] Scarano, F., Wieneke, B., and Van Oudheusden, B. W. (2006). Tomographic Particle Image Velocimetry. *Experiments in Fluids*, 41:933–947.

[79] Schafer, L., Dierksheide, U., Klaas, M., Schäfer, L., Dierksheide, U., Klaas, M., and Schröder, W. (2011). Investigation of dissipation elements in a fully developed turbulent channel flow by tomographic particle-image velocimetry. *Physics of Fluids*, 23(035106):1–11.

[80] Schwarz, J. (2018). Characterization of xanthenic - stained nanoparticles, institute of fluid dynamics, eth zurich.

[81] Shane, J., Mazilu, M., Lee, W. M., and Dholakia, K. (2010). Effect of pulse temporal shape on optical trapping and impulse transfer using ultrashort pulsed lasers. *Optics express*, 18:7554–68.

[82] Singh, R. (2002). C. v. raman and the discovery of the raman effect. *Physics in Perspective*, 4(4):399–420.

[83] Skoog, D. A. and Leary, J. J. (1992). *Principles of instrumental analysis*. Fort Worth : Saunders College Pub, 4th ed. / douglas a. skoog, james j. leary edition. Includes bibliographical references and index.

[84] Sommer, M. E., Elgeti, M., Hildebrand, P. W., Szczepek, M., Hofmann, K. P., and Scheerer, P. (2015). Chapter twenty-six - structure-based biophysical analysis of the interaction of rhodopsin with g protein and arrestin. In Shukla, A. K., editor, *Membrane Proteins—Production and Functional Characterization*, volume 556 of *Methods in Enzymology*, pages 563 – 608. Academic Press.

[85] Tagawa, M., Tsuji, T., and Nagano, Y. (1992). Evaluation of X-probe response to wire separation for wall turbulence measurements. *Experiments in Fluids*, 12:413–421.

[86] Tao, B., Katz, J., and Meneveau, C. (2000). Geometry and scale relationships in high Reynolds number turbulence determined from three-dimensional holographic velocimetry. *Physics of Fluids*, 12(5):941–944.

[87] Thompson, R. B., Gryczynski, I., and Malicka, J. (2002). Fluorescence polarization standards for high-throughput screening and imaging. *BioTechniques*, 32(1):34–42. PMID: 11808695.

[88] Tokumaru, P. T. and Dimotakis, P. E. (1995). Image correlation velocimetry. *Experiments in Fluids*, 19(1):1–15.

[89] Tsinober, A., Kit, E., and Taitel, M. (1982). Induction Velometry: Some Precise Relations Between Turbulent Velocity and Electrical Fields. *Metallurgical Applications of Magnetohydrodynamics (eds. Moffat, H. K.; Proctor, M. R. E.), Cambridge*, pages 129–135.

[90] Vinuesa, R., Prus, C., Schlatter, P., and Nagib, H. M. (2016). Convergence of numerical simulations of turbulent wall-bounded flows and mean cross-flow structure of rectangular ducts. *Meccanica*, 51(12):3025–3042.

[91] Virant, M. and Dracos, T. (1997). 3d PTV and its application on lagrangian motion. *Measurement Science and Technology*, 8(12):1539–1552.

[92] Vukoslavčević, P. and Wallace, J. (1991). A 12-sensor hot-wire probe to measure the velocity and vorticity vectors in turbulent flow. *Measurement Science and Technology*, 7:1451.

[93] Wallace, J. M. (1986). Methods of measuring vorticity in turbulent flows. *Experiments in Fluids*, 4(2):61–71.

[94] Wallace, J. M. and Foss, J. F. (1995). The measurement of vorticity in turbulent flows. *Annu. Rev. Fluid Mech*, 27:469–514.

[95] Walter, E. R. H., Williams, J. A. G., and Parker, D. (2017). Solvent polarity and oxygen sensitivity, rather than viscosity, determine lifetimes of biaryl-sensitised terbium luminescence. *Chemical Communications*, 53(100):13344–13347.

[96] Ware, W. R. (1962). Oxygen quenching of fluorescence in solution: An experimental study of the diffusion process. *The Journal of Physical Chemistry*, 66(3):455–458.

[97] Wassman, W. W. and Wallace, J. M. (1979). Measurement of vorticity in turbulent shear flow. *American physical Society*, 24.

[98] Westerweel, J., Elsinga, G. E., and Adrian, R. J. (2013). Particle image velocimetry for complex and turbulent flows. *Annual Review of Fluid Mechanics*, 45(1):409–436.

[99] Wigeland, R. A., Ahmed, M., and Nagib, H. M. (1978). Vorticity measurements using calibrated vane-vorticity indicators and cross-wires. *AIAA Journal*, 16(12):1229–1234.

[100] Willert, C. (1997). Stereoscopic digital particle image velocimetry for application in wind tunnel flows. *Measurement Science and Technology*, 8(12):1465–1479.

[101] Wüstner, D., Solanko, L. M., Lund, F. W., Sage, D., Schroll, H. J., and Lomholt, M. A. (2012). Quantitative fluorescence loss in photobleaching for analysis of protein transport and aggregation. *BMC Bioinformatics*, 13(1):296.

[102] Wyngaard, J. C. (1969). Spatial resolution of the vorticity meter and other hot-wire arrays. *Journal of Physics E: Scientific Instruments*, 2(11):983–987.

[103] Yao, J., Zhao, Y., and Fairweather, M. (2015). Numerical simulation of turbulent flow through a straight square duct. *Applied Thermal Engineering*, 91:800–811.

[104] Yoon, Y. and Lueptow, R. M. (2006). Concentration of colloidal silica suspensions using fluorescence spectroscopy. *Colloids and Surfaces A: Physicochemical and Engineering Aspects*, 277(1):107 – 110.

[105] Young, A. T. (1981). Rayleigh scattering. *Appl. Opt.*, 20(4):533–535.

[106] Zhang, H., Wu, Q., and Berezin, M. Y. (2015). Fluorescence anisotropy (polarization): From drug screening to precision medicine.

[107] Zhegalova, N. G., Dergunov, S. A., Wang, S. T., Pinkhassik, E., and Berezin, M. Y. (2014). Design of fluorescent nanocapsules as ratiometric nanothermometers TOC image HHS Public Access. *Chemistry*, 20(33):10292–10297.

[108] Zhu, Z., Yang, H., and Chen, T. (2009). Direct Numerical Simulation of Turbulent Flow in A Straight Square Duct at Reynolds Number 600. *Journal of Hydrodynamics, Ser. B*, 21(5):600–607.

Appendix A

Part drawings of the experimental setup

Below are the part drawings shown for designing the experimental setup.

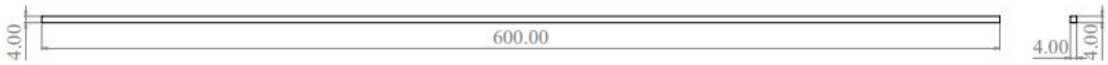

(a)

Fig. A.1 The dimensions of the glass channel with its dimensions in millimeter. The side view shows the cross-section of the channel. The channel has a rectangle to circular reducer at the inlet and the outlet which is used to connect the hoses

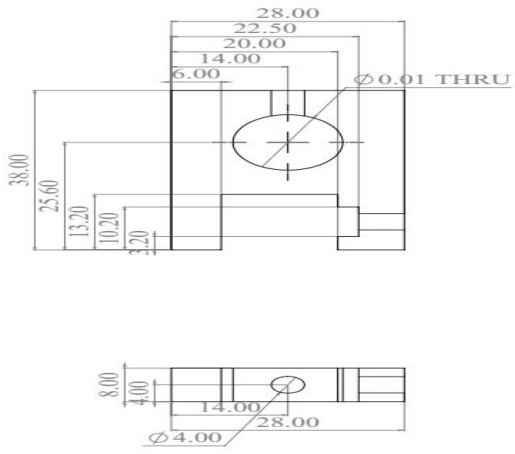

(a)

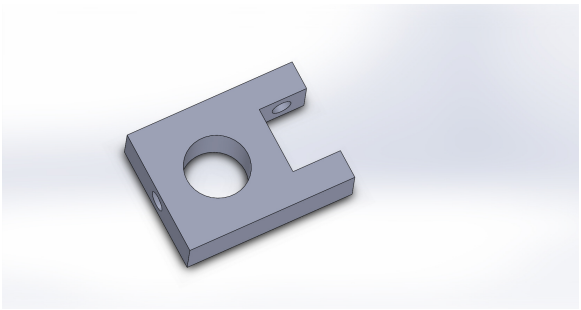

(b)

Fig. A.2 The glass channel was mounted using a 3D printed part as shown in the figure. Fig. (a) shows the front and top views with its dimensions in millimeter and the Fig. (b) shows the respective CAD part

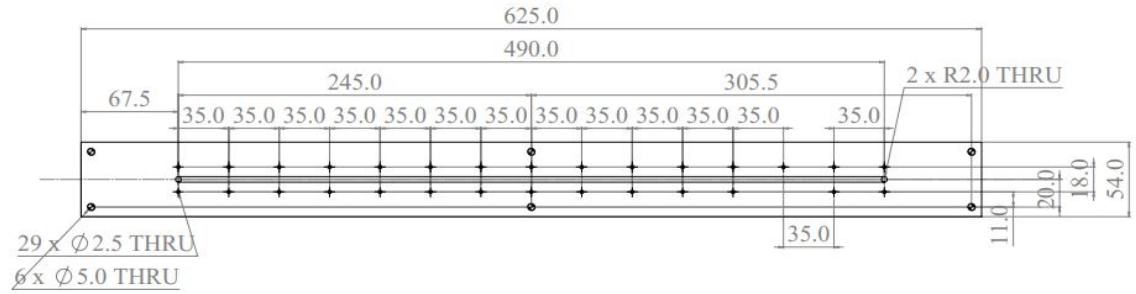

(a)

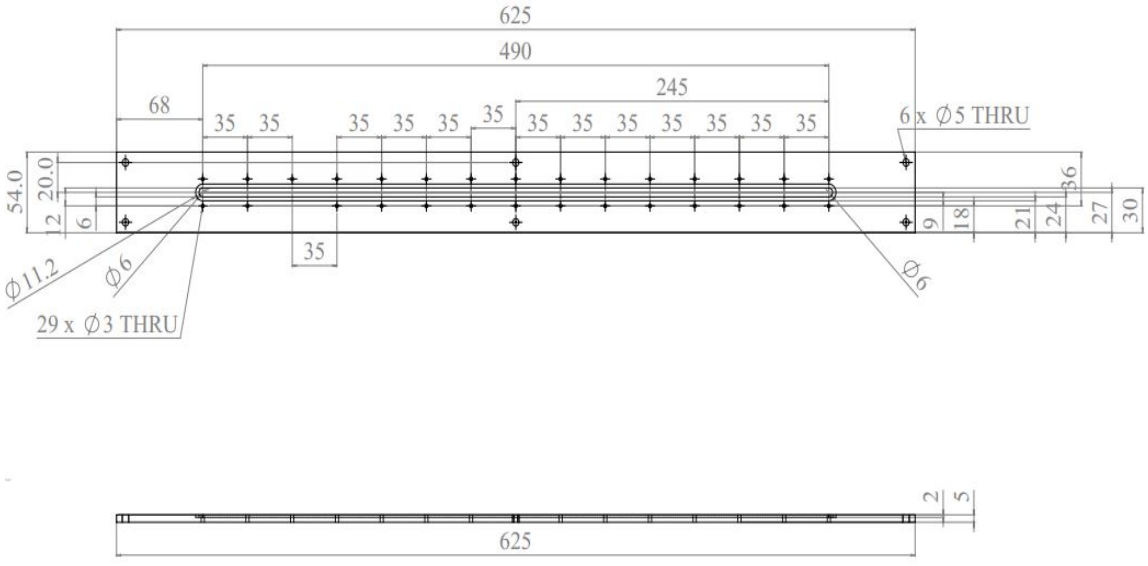

(b)

Fig. A.3 The plastic channel was built using two caskets with an O ring to prevent it from any leaks. The dimensions are in millimeter. Fig (a) shows the channel which has a cross-section of 4×4 mm^2 dimension. Fig (b) is used to mount on Fig (a) to obstruct the flow using an ellipsoidal O ring

Appendix B

Practical aspects of performing polarization based measurements to estimate vorticity

B.1 Starting the laser heads

In this project the most important part about the laser for this project is using a third harmonic crystal which emits the laser at 355nm. Dichroic optics accordingly should be suitable for 355 nm allowing it to transmit and negate the rest of the wavelengths. Most important part of this laser is the dielectric polarizer which is used to polarize the laser in a particular direction and rest of the components remain the same as PIV mode lasers. The following steps are followed for successful startup.

1. The DI water reservoir level should be sufficient before the startup of the system is very important
2. Turn on the toggle key on each laser head and wait for 6 seconds for a quick diagnostic check. Later, turn the key in counter-clockwise direction for turning on the flash-lamp and the readout display.
3. Wait for 20 minutes for complete warm-up of the laser heads
4. Cover the lab space from others for their safety and wear the goggles for protection from laser.
5. Check if the laser can be switched on by checking the Start button and the shutter button with goggles on.
6. On the laser bench slide the exit port button to Open position to allow the laser
7. Run the laser for at least 5 minutes for the harmonic crystals to get optimized with the lab temperature.

B.2 Aligning the laser sheet

The most important part about conducting the planar based measurements is aligning the laser sheet along the channel. In this project the ratio between channel width cross-section and the laser sheet is around 7 times. This ratio makes it very important for aligning the laser sheet along the glass channel.

1. Turn on the laser in low power mode with Q switch delay 300 μ s
2. Use a calibration target for the laser spot to align precisely
3. Vary the tightness of the beam splitter screws so that the laser spot is aligned precisely to the calibration target.
4. The polarizer, wave plate and the light sheet optics should be aligned such that the laser spot hits the centres of the optical parts to reduce the scattering to the fullest.
5. The iris opening should be handled to control the height of the laser sheet.

B.3 Field of view of the camera

The channel width itself can be used as the calibration target for translating the physical dimensions to the distances of the image.

1. Set the zoom of the camera macro objective, such that the channel is in focus.
2. Use the width of the channel as the calibration target
3. The camera was fixed rigidly using Thor lab mounts to Newport boards. With the desired field of view, the camera could be moved near or away from the channel.
4. Distance rings were added or removed to find the desired focus from the camera.

B.4 Part descriptions

The part descriptions are shown in the Table B.1 and Table B.2

Table B.1 Part numbers with the manufacturer as shown in the Figure F.1. This setup was built to capture phosphorescence from rhodamine and eosin Y based components.

Part numbers (Fig. F.1)	Description of the part
Roithner (30 mW, 3V DC and CW 532-30)	1
Dantec dynamics	2
Thor Labs	3
LPVISE2X from ThorLabs	4
5	Test sample (Cuvette or Channel)
OG550 Schott Glass	6
OG570 Schott Glass	7
Phoenix 5.0 MP Polarization Model with Sony IMX250MZR CMOS (Mono)	8
9	Computer system

Table B.2 Part numbers with the manufacturer as shown in the Figure 4.1. This setup was built to capture phosphorescence from europium based components.

Experimental equipment number (Fig. 4.1)	Description of the part
1	4.5 W Continuum Surelite UV pulsed laser of 355 nm with two laser heads
2	ThorLabs (HBSY13)
3	Beam Dump
4	Thorlabs (BSF10-UV)
5	ThorLabs (GLB-10)
6	Thorlabs (WPH05M-355)
7	Light sheet optics
8	Iris diaphragm
9	Test sample (Cuvette or Channel)
10	Thorlabs(LPVISE200-A)
11	Long pass filer 570 nm (OG570)
12	(Edge Filter – 643nm SWP)
13	Camera - Sensicam QE 12 bit and the objective of the camera is AF MICRO NIKKON 105 mm 1:2.8 D
14	Computer system

B.5 Procedure to conduct the experiments in the duct flow

Since this technique is in the development stage, it is important to follow a certain procedure to conduct the experiments to minimize human error. Based on the theory described in chapter 3, the following procedure is followed to study the channel flow.

1. All the experiments are conducted in the darkroom with minimum light.
2. Turn on the laser and wait for it to optimize itself to the room temperature for 30 minutes.
3. Turn on the camera and wait for it to cool down to -12 °C
4. Set the polarization of the laser to 0° using an alpha BBO Glan laser polarizer
5. Calibrate the polarization in the emission side by ensuring the anisotropy for horizontally polarized laser as 0 by using a wave-plate after the Glan laser polarizer.
6. Remove the wave-plate in the excitation side and set the filters in the emission side along with emission side polarizer (0°).
7. Keeping the laser off, take the background image to gauge the background noise levels.
8. Using the trigger box set the timing delays between the two laser heads. The Q-switch delay for each laser head is 187 μs. The delay between the two laser heads is 2 ms.
9. Turn on the pump for the channel flow and run it for 2 minutes and simultaneously turn on the laser using the trigger box and run it for two minutes before starting the experiments.
10. Run the code with sufficient exposure time to obtain the 'N' number of images. These images will be for vertically polarized excitation and vertically polarized emission.

11. Keeping the laser on, simultaneously conduct the other three orientation experiments by changing the polarizer angle at the excitation and emission side.

The other orientations are vertically polarized excitation and horizontally polarized emission, horizontally polarized excitation and horizontally polarized emission and horizontally polarized excitation and vertically polarized emission. They are measured using a wave-plate coupled with an alpha BBO Glan laser polarizer in the excitation side.

Appendix C

Synthetic signals for Re = 7000, 17000

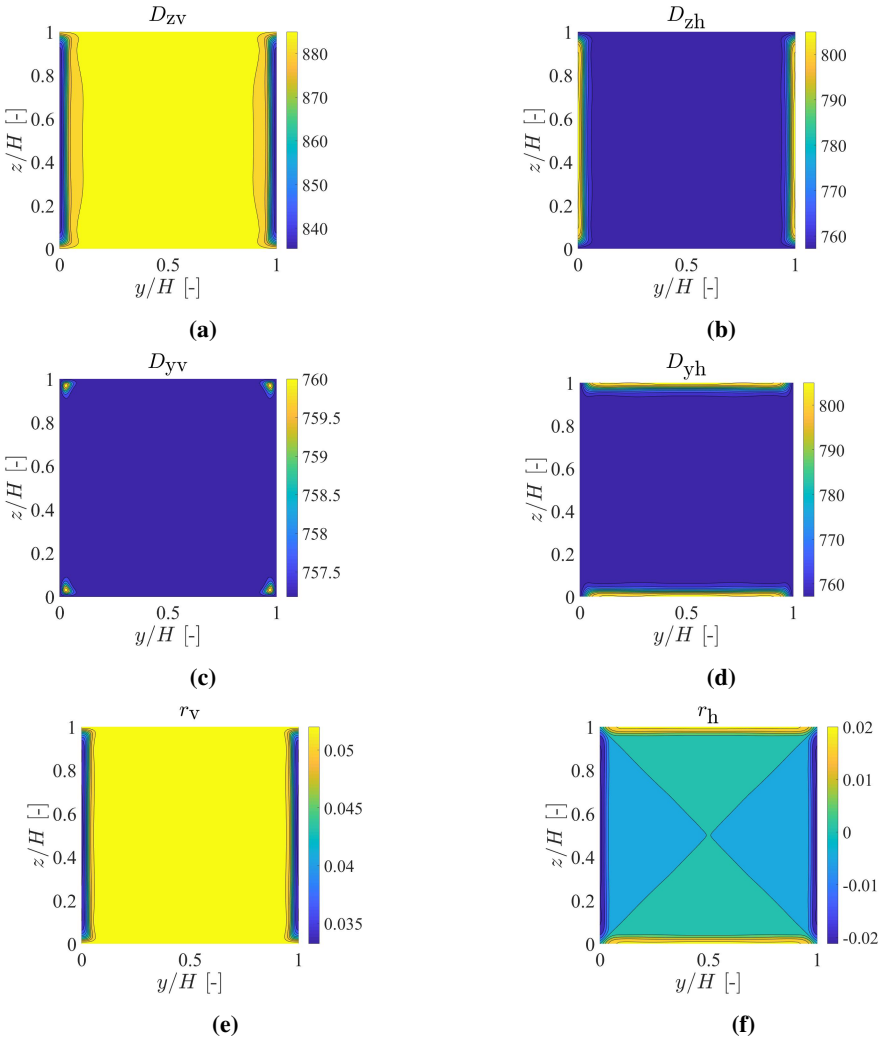

Fig. C.1 The synthetic signals computed using the DNS data [67] for Re = 7000 are shown as the contours of the channel with a cross-section of 4×4 mm^2. Using Appendix D the above signals were computed.

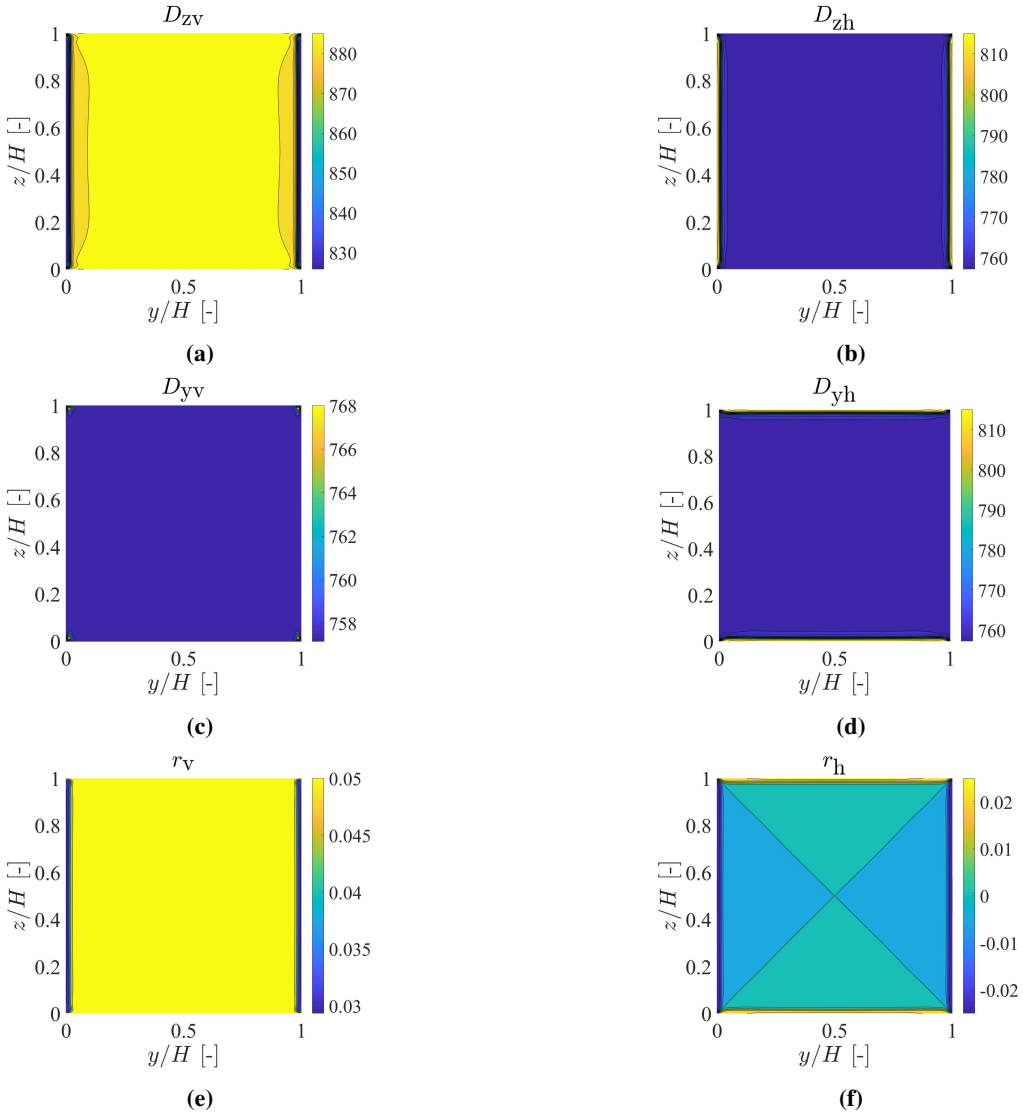

Fig. C.2 The synthetic signals computed using the DNS data [67] for Re = 17000 are shown as the contours of the channel with a cross-section of 4×4 mm^2. Using Appendix D the above signals were computed.

Appendix D

Synthetic signals correlations

The signals D_{zv}, D_{zh}, D_{yv} and D_{yh} are the time integrated solutions used to create the optimization problem for measuring the vorticity as elaborated in section 3.3. Please note that here, $\tau_{\mathrm{br}} = \tau_c$ and $\tau_{\mathrm{l}} = \tau_f$.

$$
\begin{aligned}
D_{\mathrm{zv}} = & \left[\frac{I_0\,\tau_l}{(3\,\tau_l+3\,\tau_{br})\,(\Omega^2\tau_l{}^2\tau_{br}{}^2+\tau_{br}{}^2+2\,\tau_{br}\,\tau_l+\tau_l{}^2)\,(4\,\Omega^2\tau_l{}^2\tau_{br}{}^2+\tau_{br}{}^2+2\,\tau_{br}\,\tau_l+\tau_l{}^2)}\right]\times \\
& \Bigg[2/5\left(3\left(1+\left(\Omega^2-3\,\omega_z{}^2\right)^2\tau_l{}^4+\left(2\,\Omega^2+3\,\omega_z{}^2\right)\tau_l{}^2\right)\tau_{br}{}^4+3\left(\left(4\,\Omega^2+6\,\omega_z{}^2\right)\tau_l{}^3+4\,\tau_l\right)\tau_{br}{}^3+\right. \\
& 3\left(\left(2\,\Omega^2+3\,\omega_z{}^2\right)\tau_l{}^4+6\,\tau_l{}^2\right)\tau_{br}{}^2+12\,\tau_l{}^3\tau_{br}+3\,\tau_l{}^4\tau_{br}\,(\cos(\varepsilon))^2+4\left(\frac{3}{20}+\left(3/5\,\Omega^2\omega_z{}^2+\frac{9\,\Omega^4}{10}-\right.\right. \\
& \left.\frac{9\,\omega_z{}^4}{10}\times\tau_l{}^4+\left(\frac{21\,\Omega^2}{20}-3/10\,\omega_z{}^2\right)\tau_l{}^2\tau_{br}{}^5+4\left(\Omega^4\tau_l{}^5+\left(\frac{67\,\Omega^2}{20}-3/5\,\omega_z{}^2\right)\tau_l{}^3+\frac{17\,\tau_l}{20}\right)\tau_{br}{}^4+ \\
& \left.\left.4\left(\left(\frac{71\,\Omega^2}{20}-3/10\,\omega_z{}^2\right)\tau_l{}^4+\frac{19\,\tau_l{}^2}{10}\right)\tau_{br}{}^3+4\left(5/4\,\Omega^2\tau_l{}^5+\frac{21\,\tau_l{}^3}{10}\right)\tau_{br}{}^2+\frac{23\,\tau_l{}^4\tau_{br}}{5}+\tau_l{}^5\right]\right. \qquad \text{(D.1)}
\end{aligned}
$$

$$
\begin{aligned}
D_{\mathrm{zh}} = & \left[4\,\frac{I_0\,\tau_l}{(3\,\tau_l+3\,\tau_{br})\,(\Omega^2\tau_{br}{}^2\tau_l{}^2+\tau_{br}{}^2+2\,\tau_{br}\,\tau_l+\tau_l{}^2)\,(4\,\Omega^2\tau_{br}{}^2\tau_l{}^2+\tau_{br}{}^2+2\,\tau_{br}\,\tau_l+\tau_l{}^2)}\right]\times \\
& \Bigg[\left(1/10\left(3\left(-1/2+\left(\Omega^2-3\,\omega_z{}^2\right)\left(\Omega^2-3\,\omega_y{}^2\right)\tau_l{}^4+9\,\tau_l{}^3\omega_x\,\omega_y\,\omega_z+\left(1/2\,\Omega^2-3\,\omega_y{}^2-3\,\omega_z{}^2\right)\tau_l{}^2\right)\tau_{br}{}^4+\right.\right. \\
& 3\left(9\,\tau_l{}^3\omega_x\,\omega_y\,\omega_z-2+\left(\Omega^2-6\,\omega_y{}^2-6\,\omega_z{}^2\right)\tau_l{}^2\right)\tau_l\,\tau_{br}{}^3+3/2\left(-6+\left(\Omega^2-6\,\omega_y{}^2-6\,\omega_z{}^2\right)\tau_l{}^2\right)\tau_l{}^2\tau_{br}{}^2 \\
& -6\,\tau_l{}^3\tau_{br}-3/2\,\tau_l{}^4\tau_{br}\,(\cos(\varepsilon))^2+\left(3/10+\left(\frac{9\,\Omega^4}{10}+\left(3/10\,\omega_y{}^2+3/10\,\omega_z{}^2\right)\Omega^2-\frac{9\,\omega_y{}^2\omega_z{}^2}{10}\right)\tau_l{}^4\right. \\
& -\frac{9\,\tau_l{}^3\omega_x\,\omega_y\,\omega_z}{10}+\left(6/5\,\Omega^2+3/10\,\omega_z{}^2+3/10\,\omega_y{}^2\right)\tau_l{}^2\tau_{br}{}^5+\tau_l\left(\frac{29}{20}+\Omega^4\tau_l{}^4-\frac{9\,\tau_l{}^3\omega_x\,\omega_y\,\omega_z}{10}+\right. \\
& \left.\left(\frac{73\,\Omega^2}{20}+3/5\,\omega_z{}^2+3/5\,\omega_y{}^2\right)\tau_l{}^2\tau_{br}{}^4+1/10\left(28+37\left(\Omega^2+\frac{3\,\omega_y{}^2}{37}+\frac{3\,\omega_z{}^2}{37}\right)\tau_l{}^2\right)\tau_l{}^2\tau_{br}{}^3\right. \\
& \left.\left.\left.+\left(5/4\,\Omega^2\tau_l{}^5+\frac{27\,\tau_l{}^3}{10}\right)\tau_{br}{}^2+\frac{13\,\tau_l{}^4\tau_{br}}{10}+1/4\,\tau_l{}^5\right]\right. \qquad \text{(D.2)}
\end{aligned}
$$

$$D_{\mathrm{yv}} = \left[\frac{I_0\,\tau_l}{(3\,\tau_l+3\,\tau_{br})\,(\Omega^2\,{\tau_{br}}^2\,{\tau_l}^2+{\tau_{br}}^2+2\,\tau_{br}\,\tau_l+{\tau_l}^2)\,(4\,\Omega^2\,{\tau_{br}}^2\,{\tau_l}^2+{\tau_{br}}^2+2\,\tau_{br}\,\tau_l+{\tau_l}^2)}\right]\times$$
$$\left[\left(-4/5\,\left(3\,\left(1/4+\left(\Omega^2-3\,{\omega_z}^2\right)\,\left(\Omega^2-3/2\,{\omega_y}^2-3/2\,{\omega_z}^2\right)\,{\tau_l}^4+9/2\,{\tau_l}^3\,\omega_x\,\omega_y\,\omega_z+\right.\right.\right.\right.$$
$$\left(5/4\,\Omega^2-3/2\,{\omega_y}^2\right)\,{\tau_l}^2\,{\tau_{br}}^4+3\,\left(9/2\,{\tau_l}^4\,\omega_x\,\omega_y\,\omega_z+\left(5/2\,\Omega^2-3\,{\omega_y}^2\right)\,{\tau_l}^3+\tau_l\right)\,{\tau_{br}}^3$$
$$+3\,\left(\left(5/4\,\Omega^2-3/2\,{\omega_y}^2\right)\,{\tau_l}^4+3/2\,{\tau_l}^2\right)\,{\tau_{br}}^2+3\,{\tau_l}^3\,\tau_{br}+3/4\,{\tau_l}^4\,\tau_{br}\,(\cos(\varepsilon))^2+$$
$$4\,\left(3/10+\left(6/5\,\Omega^4+\left(-\frac{9\,{\omega_z}^2}{10}-3/10\,{\omega_y}^2\right)\,\Omega^2+\frac{9\,{\omega_z}^2\,\left({\omega_y}^2+{\omega_z}^2\right)}{10}\right)\,{\tau_l}^4+\frac{9\,{\tau_l}^3\,\omega_x\,\omega_y\,\omega_z}{10}+\right.$$
$$\left(3/2\,\Omega^2-3/10\,{\omega_y}^2\right)\,{\tau_l}^2\,{\tau_{br}}^5+4\,\left(\frac{29}{20}+\Omega^4\,{\tau_l}^4+\frac{9\,{\tau_l}^3\,\omega_x\,\omega_y\,\omega_z}{10}+\left(\frac{17\,\Omega^2}{4}-3/5\,{\omega_y}^2\right)\,{\tau_l}^2\right)\,\tau_l\,{\tau_{br}}^4$$
$$\left.+4\,\left(\left(4\,\Omega^2-3/10\,{\omega_y}^2\right)\,{\tau_l}^4+\frac{14\,{\tau_l}^2}{5}\right)\,{\tau_{br}}^3+4\,\left(5/4\,\Omega^2\,{\tau_l}^5+\frac{27\,{\tau_l}^3}{10}\right)\,{\tau_{br}}^2+\frac{26\,{\tau_l}^4\,\tau_{br}}{5}+{\tau_l}^5\right] \quad \text{(D.3)}$$

$$D_{\mathrm{yh}} = \left[\frac{I_0\,\tau_l}{(3\,\tau_l+3\,\tau_{br})\,(\Omega^2\,{\tau_l}^2\,{\tau_{br}}^2+{\tau_{br}}^2+2\,\tau_l\,\tau_{br}+{\tau_l}^2)\,(4\,\Omega^2\,{\tau_l}^2\,{\tau_{br}}^2+{\tau_{br}}^2+2\,\tau_l\,\tau_{br}+{\tau_l}^2)}\right]\times$$
$$\left[\left(-4/5\,\left(3\,\left(1/4+\left(\Omega^2-3/2\,{\omega_y}^2-3/2\,{\omega_z}^2\right)\,\left(\Omega^2-3\,{\omega_y}^2\right)\,{\tau_l}^4-9/2\,{\tau_l}^3\,\omega_x\,\omega_y\,\omega_z+\right.\right.\right.\right.$$
$$\left(5/4\,\Omega^2-3/2\,{\omega_z}^2\right)\,{\tau_l}^2\,{\tau_{br}}^4+3\,\left(-9/2\,{\tau_l}^4\,\omega_x\,\omega_y\,\omega_z+\left(5/2\,\Omega^2-3\,{\omega_z}^2\right)\,{\tau_l}^3+\tau_l\right)\,{\tau_{br}}^3$$
$$+3\,\left(\left(5/4\,\Omega^2-3/2\,{\omega_z}^2\right)\,{\tau_l}^4+3/2\,{\tau_l}^2\right)\,{\tau_{br}}^2+3\,{\tau_l}^3\,\tau_{br}+3/4\,{\tau_l}^4\,\tau_{br}\,(\cos(\varepsilon))^2$$
$$+4\,\left(3/10+\left(6/5\,\Omega^4+\left(-3/10\,{\omega_z}^2-\frac{9\,{\omega_y}^2}{10}\right)\,\Omega^2+\frac{9\,{\omega_y}^2\,\left({\omega_y}^2+{\omega_z}^2\right)}{10}\right)\,{\tau_l}^4-\frac{9\,{\tau_l}^3\,\omega_x\,\omega_y\,\omega_z}{10}\right.$$
$$+\left(3/2\,\Omega^2-3/10\,{\omega_z}^2\right)\,{\tau_l}^2\,{\tau_{br}}^5+4\,\tau_l\,\left(\frac{29}{20}+\Omega^4\,{\tau_l}^4-\frac{9\,{\tau_l}^3\,\omega_x\,\omega_y\,\omega_z}{10}+\left(\frac{17\,\Omega^2}{4}-3/5\,{\omega_z}^2\right)\,{\tau_l}^2\right)\,{\tau_{br}}^4$$
$$\left.+4\,\left(\left(4\,\Omega^2-3/10\,{\omega_z}^2\right)\,{\tau_l}^4+\frac{14\,{\tau_l}^2}{5}\right)\,{\tau_{br}}^3+4\,\left(5/4\,\Omega^2\,{\tau_l}^5+\frac{27\,{\tau_l}^3}{10}\right)\,{\tau_{br}}^2+\frac{26\,{\tau_l}^4\,\tau_{br}}{5}+{\tau_l}^5\right] \quad \text{(D.4)}$$

Appendix E

Comparison of fresh and used sample

When the stream of particles is run down the gear pump, it was important to check if the particles are harmed or any coagulation is observed. To check this, the anisotropy of the fresh sample and old used sample from the reservoir is experimented. Fig. E.1 shows the comparison between old and fresh sample of the particles. Fig. E.1a shows the variation of column averaged mean anisotropy of 5 images across the cuvette in quiescent state. Fig. E.1b shows the variation of standard deviation in anisotropy along the column averaged images. This variation shows that they approximately show same variation which means no coagulation is observed.
However from this experiment whether the particles are ground to a much finer diameter cannot be verified. Additional SEM analysis must be performed to verify the shape of the particles before and after the experiments were conducted.

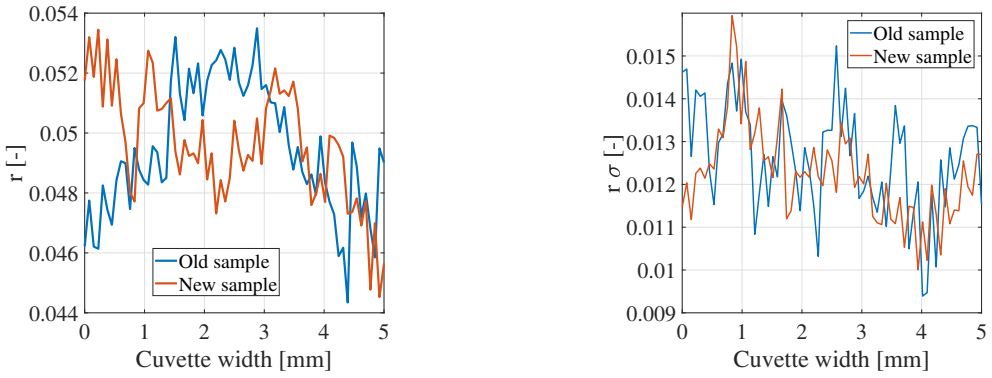

Fig. E.1 Fig (a) shows variation of mean anisotropy with cuvette width for vertically polarized laser. Fig(b) shows the variation of standard deviation of anisotropy along the column of the region of interest. Old sample means the used europium particles from the reservoir and new sample is the fresh unused europium particles from the company.

Appendix F

Variation of anisotropy in the channel for scattering and fluorescent particles

F.1 Phosphorescence anisotropy setup using rhodamine and eosin Y

Two setups were built during this thesis to capture the phosphorescence quantum yield. The experimental setup described in this section was built to capture the phosphorescence from rhodamine and eosin Y based compounds. These compounds have their excitation and emission spectrum in the visible range wavelength which makes it easier to conduct experiments using cheaper equipment. It also ensures higher levels of safety during the experiments.
The experimental setup is shown in Figure F.1. Figure F.1a shows the schematic diagram of the experimental setup. Figure F.1b shows the actual simplified experimental setup. The numbers in the figures indicate the part numbers which are listed in Table F.1. All the part descriptions are provided in the Appendix B, Table B.1.
This experimental setup was not successful to capture the phosphorescence quantum yield of rhodamine and eosin Y compounds, however, it was suitable to capture fluorescence quantum yield with ease. Since this did not work, a new experimental setup was developed as described in section 4.1. Experiments conducted using this setup for eosin Y is shown in the Figure F.4.

In this thesis, europium particles were chosen because they showed high lifetimes compared to scattering and fluorescence solutions. However, several experiments were conducted with scattering and fluorescence solutions to verify if any depolarization is observed along the edges. Fig. F.4a shows the variation of anisotropy of colloidal silica along channel width for different Re when excited using 355 nm laser. Fig. F.4b shows the variation of anisotropy of eosin Y along channel width for different Re when excited using 532 nm laser.
Methods from the [34] was also tried to remove dissolved oxygen using sodium sulfite. However a continuous supply of sodium sulfite and an air tight cuvettes had to be ensured for a steady high quantum yield and a consistent anisotropy. Due to these reasons, the above could not be incorporated in this thesis.

Yoon and Lueptow [104] and Bertoluzza et al. [9] have conducted experiments previously using colloidal silica in the UV range. They observe colloidal silica showing fluorescence and scattering due to the chemical nature of the silica when excited in the UV range. Eosin Y shows fluorescence when excited by 532 nm laser indicating the lifetimes in order of nanoseconds as shown earlier. However, scattering and fluorescence do not show any depolarization along the edges which indicates that they are not sensitive to the vorticity along the edges of the duct flow. Schwarz [80] conducted intensity decay experiments with eosin Y at various

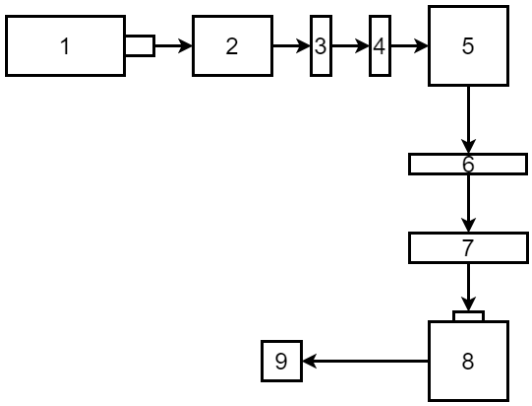

(a) The schematic diagram of the experimental setup.

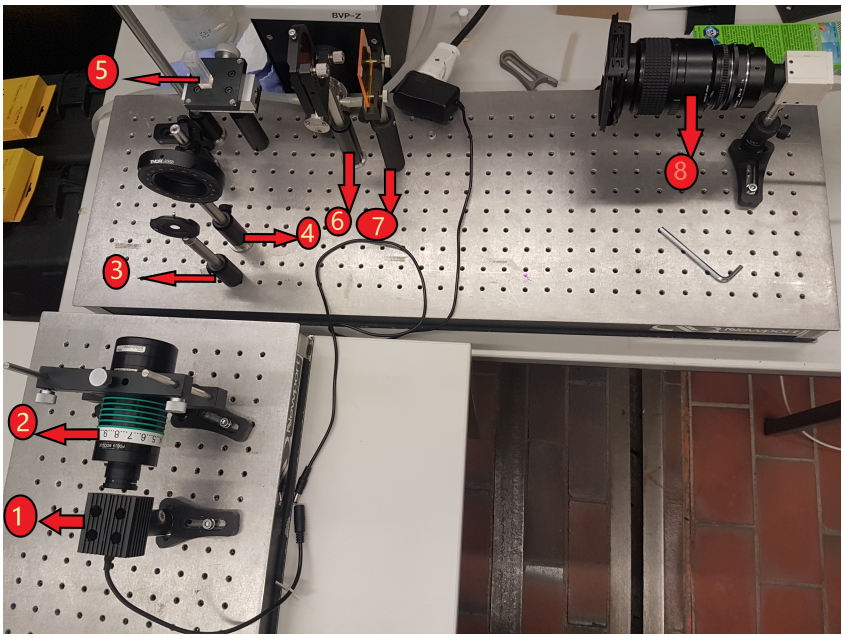

(b) Actual experimental setup.

Fig. F.1 Schematic diagram of the experimental setup is shown in Fig. (a) and the actual experimental setup is shown in Fig. (b). The numbering in the schematic diagram and the experimental setup image denotes the parts as described in the Table F.1.

concentrations. Figure F.3a shows the intensity decay curve with respect to the timescale. The two lifetimes for Eosin Y is shown as 134 ns and 553 ns. The respective two processes are delayed fluorescence and phosphorescence since the timescale of fluorescence is generally under 10 ns [83].

Phosphorescence quantum yield of rhodamine and eosin Y particles is very low at room temperature. To increase the phosphorescence quantum yield in the room temperature, Kuijt et al. [34] and Davis et al.[16] listed several techniques depending on the type of fluorescent molecule. One of the techniques used in this thesis involved the usage of sodium sulfite (350 ppm) as an oxygen scavenger, sodium iodide (50mM) as HAP and eosin Y based PMMA particles were mixed to enhance phosphorescence yield. Heavy Atom Perturber (HAP) was used to reduce the non-radioactive decay and increase the phosphorescence efficiency. A surge in phosphorescence yield was observed after 650 nm. However, this technique was not suitable for this thesis,

Table F.1 List of components as shown in the Figure F.1. This setup was built to capture phosphorescence from rhodamine and eosin Y compounds

Experimental equipment number (Figure F.1)	Description of the part
1	Laser 532 nm Nd:YAG (30 mW, CW)
2	Light sheet optics
3	Iris diaphragm
4	Linear film polarizer
5	Test sample (optical glass fluorescence cuvette or square duct)
6	Long pass filter - 1
7	Long pass filter - 2
8	Phoenix 5.0 MP polarization camera and objective of the camera is AF MICRO NIKKON 105 mm 1:2.8 D
9	Computer system
Seeding particles	Rhodamine (diameter = 250 nm) and eosin Y (diameter = 100 nm)
Observation distance	10 cm
Exposure	2 s

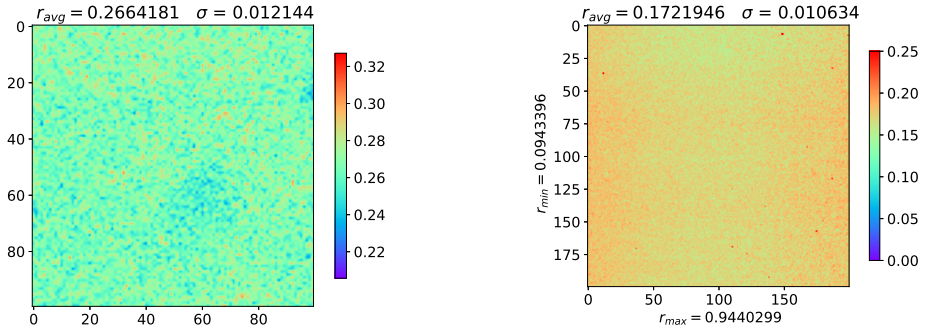

(a) **(b)**

Fig. F.2 Anisotropy measurements of fixed eosin Y nanoparticles is shown in Fig (a). Anisotropy measurements of eosin Y nanoparticles in quiescent flow state is shown in Fig (b).

since the mixed state of rhodamine, sodium sulfite and sodium iodide was not stable. The phosphorescence yield from the above sample was not reproducible after many experiments. Rhodamine based PMMA particles did not show uniform reactivity with sodium iodide and oxygen scavenger resulting in erroneous results. Spectroscopy analysis of eosin Y particles was necessary since the project aimed at capturing their respective phosphorescence quantum yield. Figure F.3b shows two points on the graph (1 and 2 marked in red). Point 1 is the peak near 532 nm because of the laser. It shows a smaller peak because it was filtered using 550 nm long-pass filter. Point 2 near 610 nm shows a slight increase in the intensity. This might be due to the overlap of delayed fluorescence or phosphorescence to the fluorescence spectra. However, using the experimental setup as described in section F.2, the fluorescence and phosphorescence yield could not be differentiated.

F.2 Variation of anisotropy in the channel

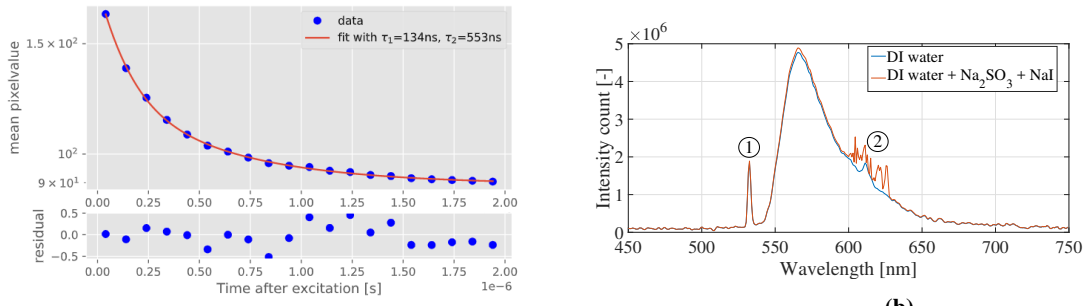

Fig. F.3 The intensity decay with a two exponential fit for Eosin Y 85% as shown in Fig(a) [80]. Fig(b) shows the variation of phosphorescence quantum yield spectra of eosin Y in DI water and by adding heavy atom perturber (NaI) and the oxygen scavenger (Na_2SO_3) by following the procedure [16]. The integration time was 0.5 seconds.

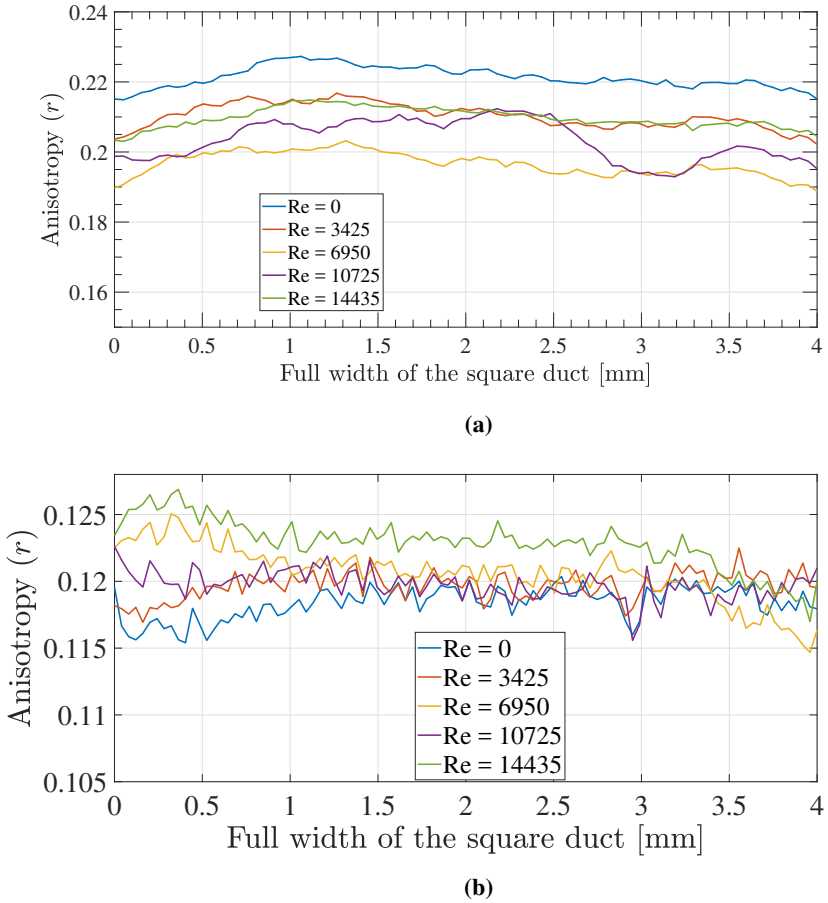

Fig. F.4 Variation of mean anisotropy for different Re across the full channel. Fig (a) shows the variation of anisotropy for colloidal silica which shows fluorescence and scattering when excited by 355 nm laser Fig. (b) shows the variation of anisotropy for eosin Y which shows fluorescence when excited by 532 nm laser.

Appendix G

Optical forces on the nanoparticles

Based on the problem formulation as described in section 3.5, the effect of the optical forces on the nanoparticles was estimated using the computational toolbox in MATLAB developed by Nieminen et al. [57]. Nieminen et al. developed a computational toolbox which calculates the forces on the spherical particles due to the electromagnetic fields exerted by the laser. They use spherical partial wave expansion to express scattering fields in electromagnetic theory. Fig. G.1 shows the variation of the non-dimensional axial (Q_z) and radial

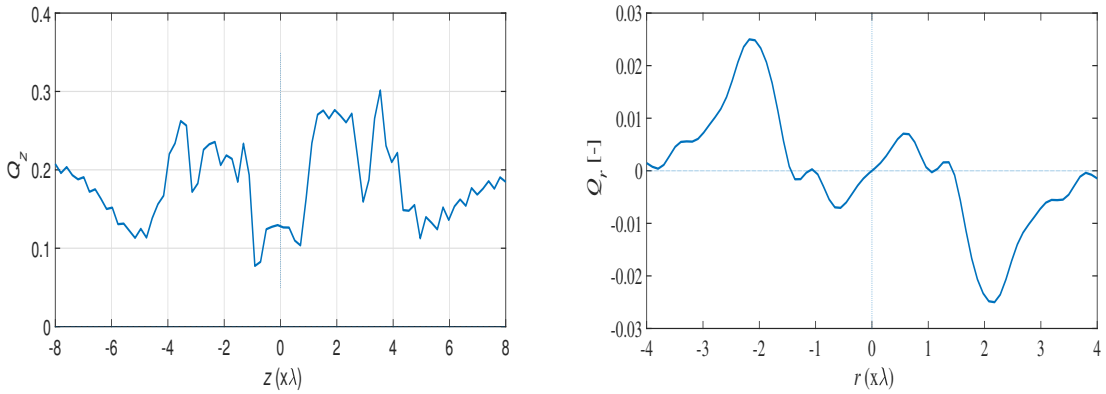

(a) **(b)**

Fig. G.1 The optical forces on the nanoparticle by a high powered laser in the z direction (a) and in the radial direction (b).

forces (Q_r) by the laser on the europium nanoparticles . This analysis was conducted assuming that the laser is fully focused on the gelatin fixed particles and a very low numerical aperture in the order of 10^{-5}.
The input parameters in the toolbox is The numerical aperture (NA) of a Gaussian laser beam is defined as,

$$\mathrm{NA} \approx \frac{\lambda_0}{\pi w_0} \tag{G.1}$$

Here, $2w_0$ is the diameter of the beam at its narrowest spot and λ_0 is the wavelength of the laser. The laser used in this project was a Gaussian beam laser, but the diameter of the beam at the narrowest spot is in the millimeter range. λ_0 is 355 nm laser and of 4.5 W power pulsed laser. Shane et al. [81] shows that the optical forces on the nanoparticles is independent of the pulse duration as long as the total force is computed on the nanoparticles.

By substituting NA and the wavelength of the laser in the computational toolbox, Fig. G.1 is plotted. Fig. G.1b is the radial force that is very symmetric and is 0 at r(xz)=0 which laser-focused center of the particle. However Fig. G.1a is the axial force that happens to experience a positive (0.125) force. This means the laser tries to push the particle in the direction of the propagation of the beam away from the focused center. This might cause the particle to translate and rotate. The forces responsible for this is Q_z and Q_r. They are multiplied by $\frac{nP}{c} \approx 10^{-8}$ to represent the forces in Newton. The magnitude of these forces are insignificant compared to shear forces in the boundary layer. Hence, the scattering force in the z-direction on the nanoparticles due to the laser can be neglected. Here P is the laser power, c is the speed of light and n is the refractive index of the particle.

Appendix H

Different approaches undertaken to build the optimization problem

1. The optimization function was built using 4 angles of the emissions (0, 90, 45 and 135) for vertically polarized laser. However, the anisotropy of europium particles is too low in the quiescent state to show clear distinction in the above components, which leads to erroneous results.
2. The optimization problem was built as a function of ratios of no-flow condition. However this did not work, because of the in-homogeneity of the no-flow condition making it an additional degree of freedom in the sources of error. Hence quiescent flow anisotropy was not considered. Photo-bleaching was one more factor which could be negated if no-flow condition anisotropy was not considered.
3. The author tried simplifying the analytical correlations by reducing it into two equation or one equation methods and trying to solve using ICCG algorithm with deflation vectors as POD system obtained from assuming individual vorticity values as zero. However, this system did not give the right answer with respect to the DNS due to over simplification.

Appendix I

Standard deviation intensity graphs for different Re and column averaged standard deviation plots

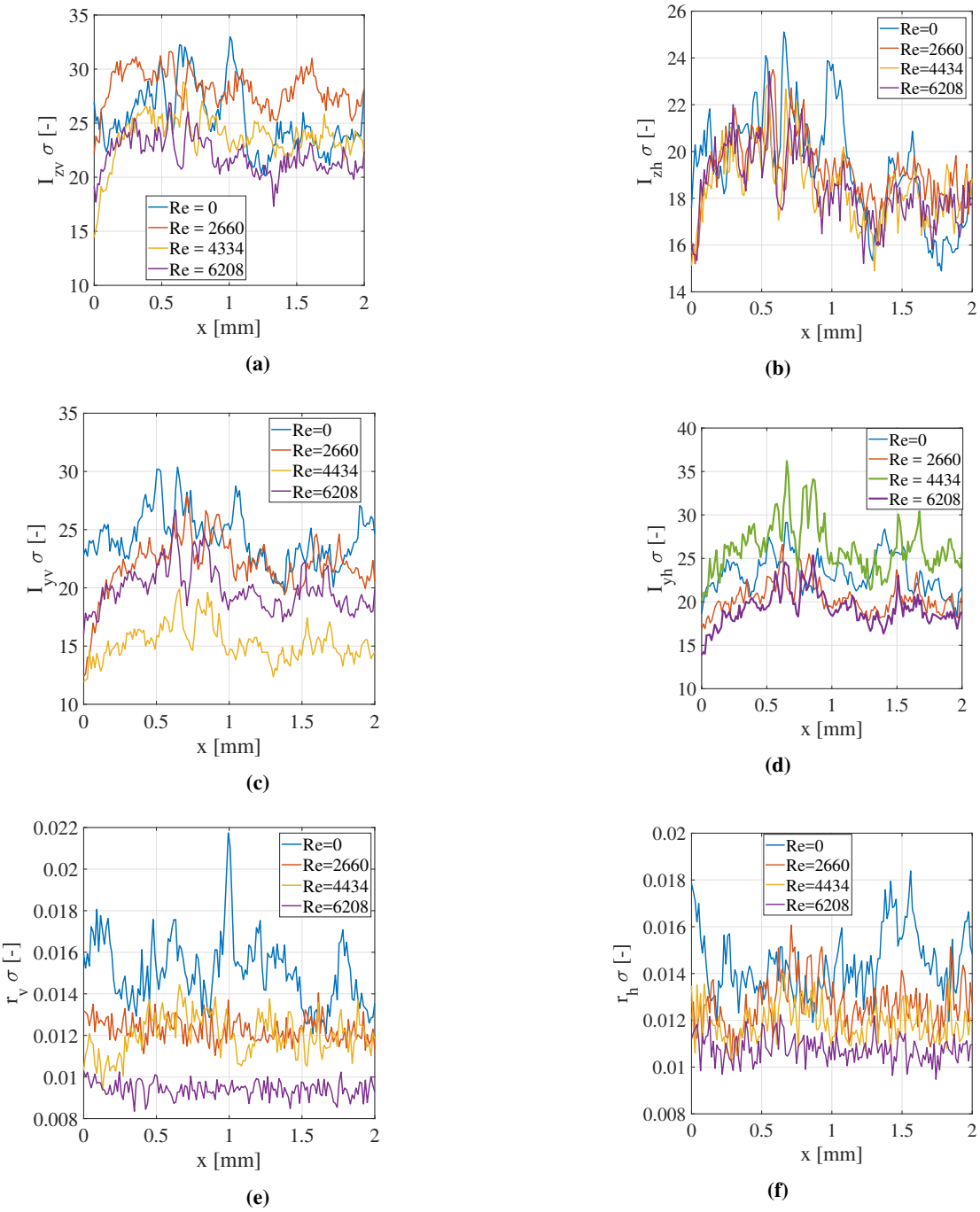

Fig. I.1 This shows the variation of standard deviation along the column for different Re. Figure I.1a shows the standard deviation plots for vertically polarized laser and vertically polarized emission. Figure I.1b shows the contour for vertically polarized laser and horizontally polarized emission. Figure I.1c shows the contour for horizontally polarized laser and vertically polarized emission. Figure I.1d shows the contour for horizontally polarized laser and horizontally polarized emission. Figure I.1e show the anisotropy computed for vertically polarized laser orientation using Figure I.1a and Figure I.1c. Figure I.1f show the anisotropy computed for horizontally polarized laser orientation using Figure I.1d and Figure I.1b.

Appendix J

Reproducibility studies

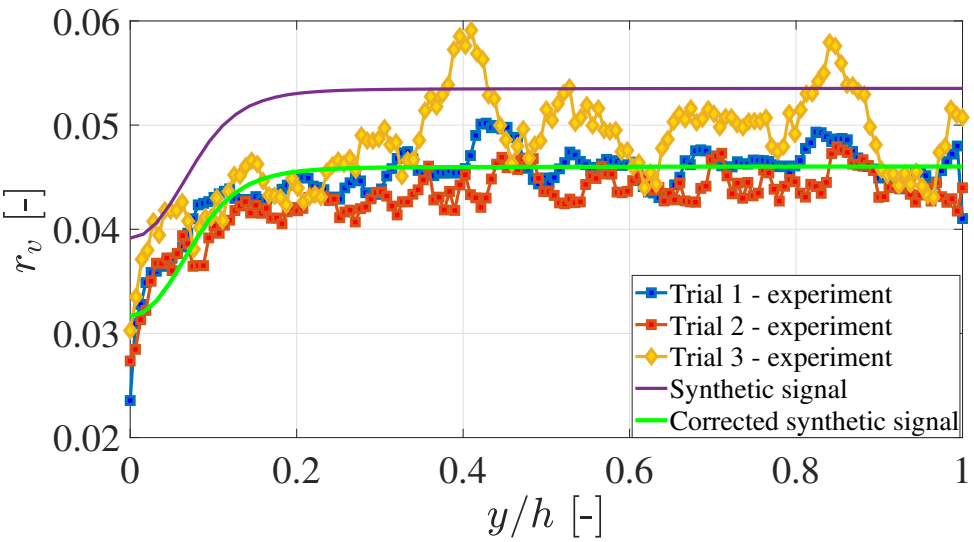

Fig. J.1 This figure shows the variation of r_v for three experimental trials at Re = 4434 and the synthetic signal computed as shown in Figure 6.1 along the half width of the square duct. The main observation in anisotropy is the drop in the anisotropy near the edges of the duct caused due to vorticity. The synthetic signal is expected anisotropy drop without any scattering from the setup. However the corrected synthetic signal when the scattering is accounted is shown in the figure. This correction factor depends on the experimental setup and the nanoparticles.

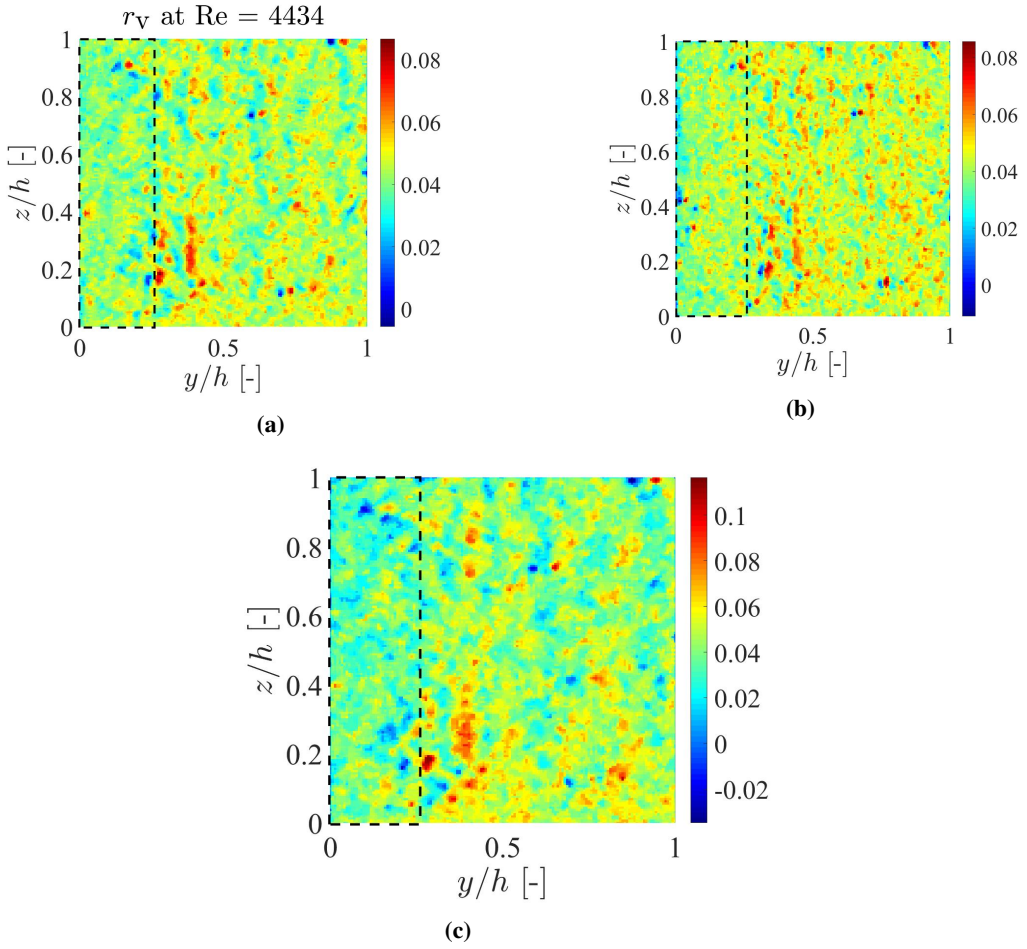

Fig. J.2 The above figures shows the respective contours of r_v for three trials at Re = 4434. It can be observed that the contours are considerably noisy because of the error in the respective intensity signals. The main observation that can be made is the slight increase in average r_v from the $y/h = 0$ to 1. These are plotted as column averages in Figure J.1.

J.1 Anisotropy images for Re = 2660, 6208

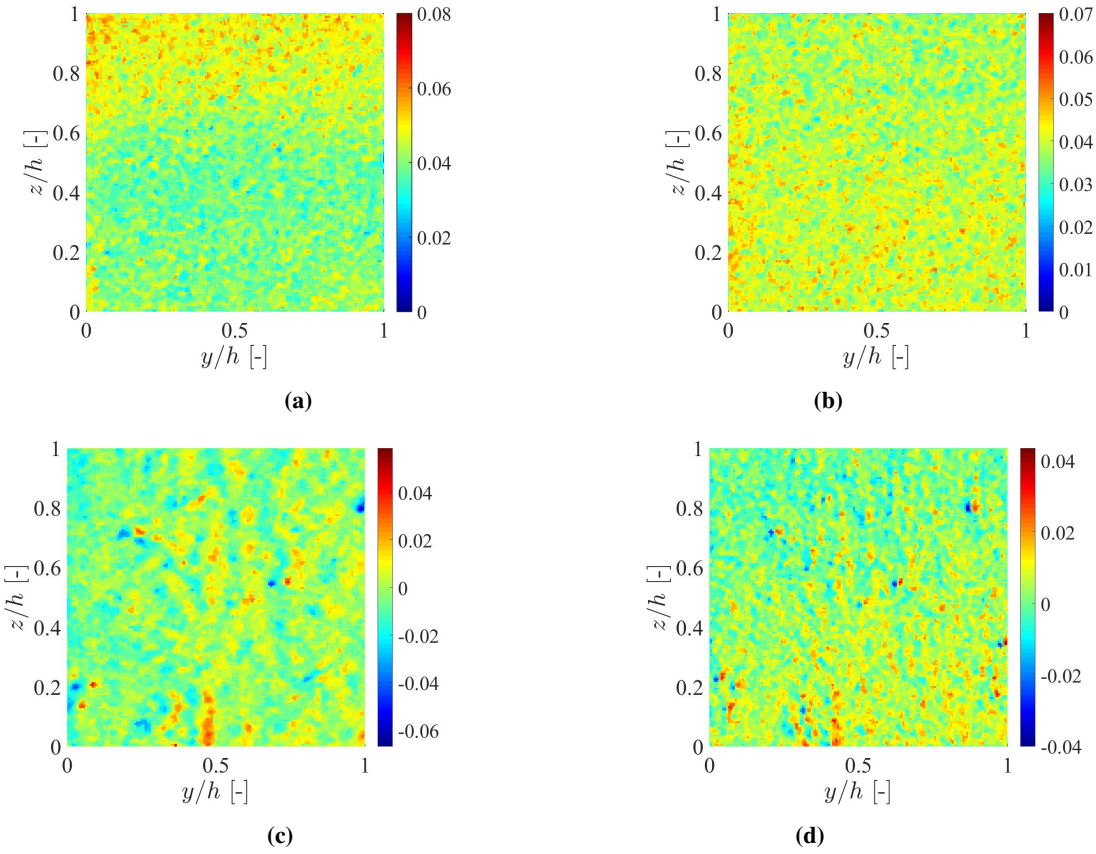

Fig. J.3 The above contours are the anisotropy contours at Re = 2660 and 6208 for a quarter cross-section of the square duct. Fig. (a) shows r_v at Re = 2660. Fig. (b) shows r_v at Re = 6208. Fig. (c) shows r_h at Re = 2660. Fig. (d) shows r_h at Re = 6208.

J.2 Variation of sensitivity of the optimization algorithm for different Re

The optimization algorithm does not function for column or row averaged ω_x due to very low value. After Re = 20000, the optimization algorithm would work pixel by pixel near the edges since ND1 would be close to 1. "Output from optimization algorithm" means synthetic signals obtained from formulae in Appendix D at a particular Re, is used as input again in the optimization algorithm to check its sensitivity.

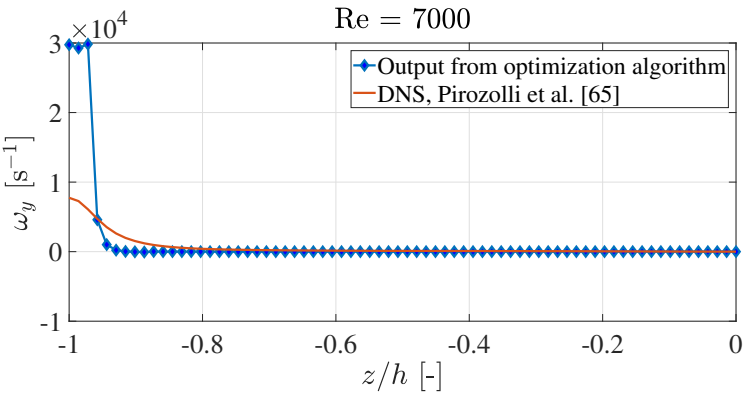

(a)

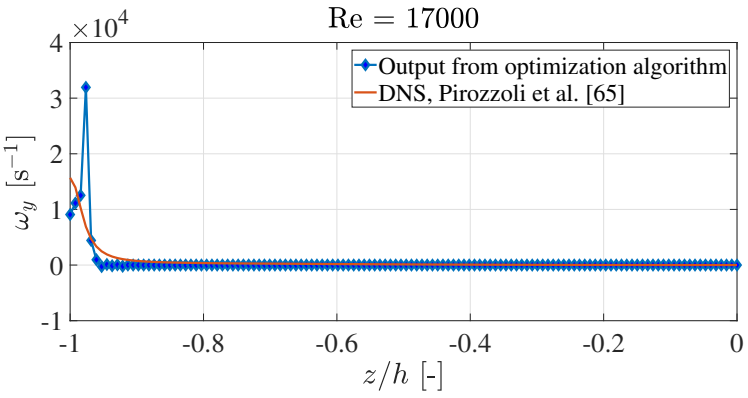

(b)

Fig. J.4 Variation of sensitivity of the optimization algorithm of ω_y using the algorithm in section 3.4.

Appendix K

Sources of error - future scope for improvement

K.1 Experimental errors

There are various sources of error which the author has identified. If these errors are fixed then the accuracy of the results could be improved. The main possible sources of LIF error can be extrapolated here which are chemical compound, laser, CCD and Optics [15]. The reason for inaccuracies,

- Laser fluctuations shot to shot variation .
- Dirt or bubbles in the fluid medium.
- Synthesizing alternative nanoparticles with higher lifetimes and sensitive to polarized excitation.
- Employing the most suitable equipment with regards to excitation and emission spectra for minimum signal attenuation with thinner laser sheet thickness.
- Channel inhomogenieties.
- Verifying the shape of the spherical particles after it is used in the pump by conducting SEM.
- Rise in std by 3% when no flow and flow conditions are compared.
- Imperfect calibration of the emission polarization.
- Error in r_0 is 0.01.
- Error in lifetime is τ_l is 40 μs.
- Pump inaccuracies.
- The background signal may be polarized if due to scattered light, or unpolarized if due to low-molecular weight impurities.

K.2 Analytical model errors

- Rounding off errors in MATLAB due to complex equations.
- Opting the right algorithm to solve for optimization. Many researchers in the past in the field of robotics have shown that different algorithms to solve for nonlinear optimization functions show different results. It also depends on the initial value.

K.3 List of deactivation processes of phosphorescence

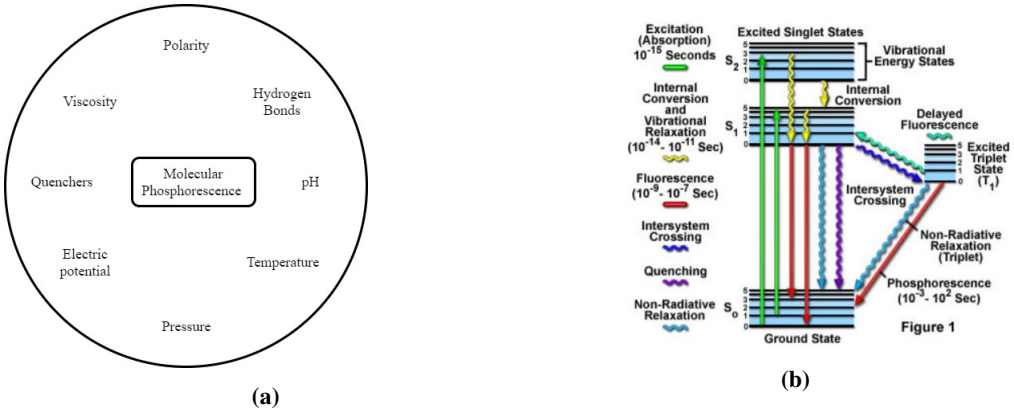

Fig. K.1 Different deactivation processes which will reduce the quantum yield of the processes. This shows the difficulty to capture phosphorescence at room temperature [40].